Broadly tuneable VECSEL-pumped crystalline Raman laser

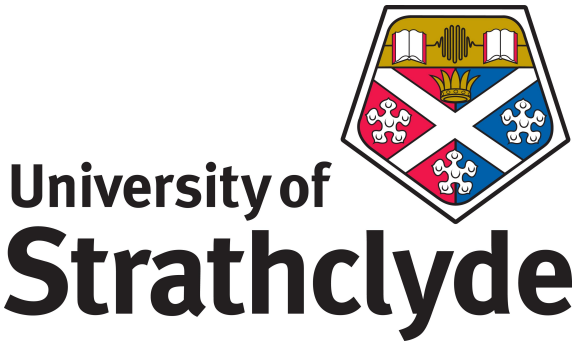

A thesis presented in fulfilment of the
requirements for the degree of

Doctor of Philosophy

by

Riccardo Casula

Institute of Photonics, Department of Physics
University of Strathclyde

2019

This thesis is the result of the author's original research. It has been composed by the author and has not been previously submitted for examination which has led to the award of a degree.

Signed:

Date: 31st October 2019

A mamma

Acknowledgements

I would like to express my infinite gratitude to the following people and institutions:

First and foremost, my supervisor, Dr. Jennifer Hastie, for giving me the opportunity to join her warm and friendly team, for her guidance throughout my PhD, and for her support to continue for the academic pathway with post-doc application. She also provided advice on the editing the thesis, reminding me that simplicity is the soul of wit.

To Prof. Alan Kemp, my second supervisor, who assisted me and contributed with his precious inputs and valuable advices.

To Drs. John-Mark Hopkins and Gerald Bonner of Fraunhofer Centre of Applied Photonics, for their suggestions in the work here presented.

To the post-doctoral researchers of the Advanced Lasers team. To Dr. Daniele Parrotta, who devoutly helped me in the lab with inexhaustible patience every time I needed it and showed me how to build a laser. To my teammate Dr. Julio Rodriguez, for the long chats, be they about lasers, politics, chess, or gaming. I also thank him for helping me design the cavity with his laser cavity design software, SimCav. To Dr. David Pabœuf, for his feedbacks and lab recommendations.

To Sharon Kelly and Lorraine Annand for their assistance in administration tasks.

To the rest of my colleagues and members of staff of the Institute of Photonics for making it a friendly place.

To Profs Pier Carlo Ricci, Michele Saba and Francesco Quochi of the Department of Physics at the University of Cagliari (Italy) for their support to continue my research abroad.

To my dearest friends, Tiziana Zedda and Claudia Zucca, for their unfailing encouragement to apply abroad, for having listened to all my preoccupations before moving out of Italy and supporting me to complete this work. To my dad and my brother, for their love and encouragement to do the best I can *–vi voglio bene*!

Finally, to the UK EPSRC Challenging Engineering Award (EP/I022791/1), ERC DiaL Grant (278389), the Fraunhofer UK Ltd and the Royal Academy of Engineering, that all financed this research.

Abstract

Here is presented the first demonstration of a continuous-wave third-Stokes crystalline Raman laser. This was achieved via intracavity Raman conversion of a vertical external cavity surface emitting laser (VECSEL), also known as a semiconductor disk laser (SDL). The VECSEL-pumped Raman laser achieved Watt-level output and broad tuneability within the water transmission window at 1.7 μm, offering potential applications in remote sensing and medical imaging. In this thesis the design and characterization of such a cascaded Raman laser are described.

The attractive performance of VECSELs based on InGaAs for emission around 1 μm, now being implemented in commercial cw laser systems, has spurred the VECSEL research community to widen the fundamental spectral coverage beyond 1.2 μm via more sophisticated and at the same time more complex growth and fabrication processes. These devices nonetheless lend themselves very well to nonlinear frequency conversion, primarily owing to the high-intensity fields generated intracavity, thus bypassing difficult epitaxy and processing to access long wavelengths with high power and low output coupling. Raman media, as $\chi^{(3)}$-type materials, are powerful tools as wavelength converters thanks to the simplified optics required to achieve stimulated Raman scattering -which is the basis of the Raman laser- when compared to most common $\chi^{(2)}$-based systems.

This thesis reports 1.1 W continuous-wave Raman laser emission centred at 1.73 μm from third-Stokes generation in a KGW crystal within an InGaAs-based VECSEL designed for fundamental emission at 1.18 μm. This system also demonstrated broad tuneability from 1696-1761 nm when the VECSEL was tuned from 1163-1193.2 nm,

exceptional beam quality ($M^2 \sim 1$) and instrument-limited narrow linewidth of 48 pm FWHM. In addition, simultaneous output coupling at the first and second Stokes was also attained, with maximum output power of 1.1 and 0.8 W at 1.5 μm and 1.32 μm, respectively tuneable from 1473-1522 nm and 1300-1338 nm. Having originally intended to reach 1.7 μm with a synthetic crystal of diamond and two Stokes shifts (the Raman shift is larger than in KGW), in this work three Stokes shifts in KGW were utilized since the deposition of robust anti-reflection coatings was more feasible on this crystal for such a broad wavelength range (1.1-1.7 μm). Nevertheless, the first Stokes shift in diamond, being AR-coated for 1.1-1.4 μm operation and pumped by the same VECSEL structure, resulted in Raman laser emission at an important water absorption region around 1.4 μm, with maximum 2.3 W output power and tuneable over a range of 42 nm.

Contents

List of Figures

List of Tables

Chapter 1

Introduction

The very first concept of stimulated emission of electromagnetic radiation was theoretically established in 1917 by Albert Einstein with the well-known Einstein coefficients [1]. The realization of the first functioning laser came more than forty years later, in 1960 [2]. Since then, laser engineering has been a very intense field of research, expanding in various technology areas, including diverse fields such as spectroscopy, telecommunication, computing, medicine, gas sensing, LIDAR, and many others. Each of these applications depends on a particular combination of different laser properties, among which emission wavelength, output power, output beam quality, but also compactness and efficiency. For example, molecular spectroscopy is an important research area as it requires high-power, single-frequency lasers with an emission wavelength that can be tuned over the spectral region in which some molecules exhibit absorption lines, typically in the near-infrared and beyond. Also, medical imaging, in particular optical coherence tomography [3], can benefit from broadly tuneable lasers near 1.5 μm and 1.7 μm thanks to the low scatter and water absorption in this region. Depending on the laser type, however, some lasers exhibit excellent properties while showing other undesired low-quality characteristics. For example, most employed sources are semiconductor diode lasers as they cover a wide range of wavelengths from the visible to the mid-infrared owing to the combination of different materials and structures in very compact devices. Due to their compact size and geometry, however, a single semiconductor diode laser can not operate with multi-Watt output power and exhibiting simultane-

ously a high-quality beam. This is typical amongst edge-emitting (high power, low beam quality) and surface-emitting diode lasers (low power, high beam quality). In contrast to semiconductors, doped solid-state and fibre lasers can emit several Watts with excellent beam quality but the emission wavelengths are limited to the electronic transitions of the guest ions.

The recent success of vertical-external-cavity surface-emitting lasers (VECSELs) [4,5], also called optically-pumped semiconductor disk lasers (OPSDLs, or SDLs), stems from their particular combination of multiple properties, such as multi-Watt output power with excellent beam quality and great wavelength flexibility, enabling laser operation from the red to the mid-infrared [6, 7]. SDLs are recently replacing most classic commercial laser sources owing to the relatively low-cost epitaxial growth process of InGaAs-based quantum well materials that make SDLs easily implemented in a range of commercial systems, such as those produced by Coherent Inc. [8]. Although SDLs can operate very efficiently with emission wavelength around 1 μm, they require different materials and growth techniques to target spectral regions beyond this region, among which more complex SDL structures based on InAs quantum dots and dilute nitride InGaAs quantum wells [9–11]. When the monolithic growth is not possible, the fabrication process based on wafer fusion, already utilized for telecom VCSELs [12], can produces SDLs to cover that part of the spectral region near 1.5 μm with great efficiency [13]. Alternatively to direct emission, the macro-cavity geometry of SDLs can be exploited to implement nonlinear materials to generate laser emission wavelengths that are hard to reach directly from semiconductor diodes. Second harmonic generation and Raman conversion are two well-known standard techniques that have been extensively employed in SDLs for bridging several gaps in the visible and the infrared region respectively [6, 7]. Commercial lasers that make the use of SDLs are based on monolithic InGaAs, adding more wavelengths in the visible via intracavity frequency doubling [8]. A recent study of SDLs showed that emission at 1.2 μm can be still fabricated with high quality, monolithically grown InGaAs quantum wells, with record of output power above 20 W [14], making them promising candidates for extending the wavelength coverage in the water transmission window up to 1.7 μm by means of

intracavity Raman conversion. This thesis will present the use of Raman crystals to shift the wavelength of SDLs based on this material towards the novel 1.7 μm region. In this chapter an overview of semiconductor and Raman lasers will be given in a bit more details.

1.1 Semiconductor laser evolution to the thin disk technology

The first working semiconductor device showing laser emission in continuous-wave was a diode based on a GaAs p-n homo-junction, demonstrating operability in the infrared at 850 nm [15]. Nowadays, the double hetero-structure is implemented in the fabrication of modern laser diodes, allowing them to be operative at standard temperature and low current density threshold. In these architectures, the active layer is between two cladding layers with higher bandgap and smaller refractive index, that confine more electrons and holes together within the small bandgap, allowing them to emit photons with greater efficiency. Since the advent of sophisticated growth processes, such as metal-organic chemical vapour deposition and molecular beam epitaxy, further improvements have been also demonstrated by reducing the middle active layer thickness to the nanometre scale and hence taking shape of quantum wells. Here the carriers are confined in one dimension with thickness on the order of the de Broglie wavelength and are allocated onto defined energy states, thereby reducing the threshold. Controlling with great precision the width and the height of the quantum well by changing the alloy fraction in ternary or quaternary compositions, determines in turn the emission wavelength.

Depending on the propagation direction of the laser emission relative to the plane of the gain region, semiconductor lasers are classified as edge-emitting or surface-emitting lasers, as represented in Fig. 1.1. In edge emitters, the laser emits from the cleaved edge as the in-plane waveguide guides the radiation, as shown in Fig, 1.1. Propagation along the longer axis ($\sim$ 100-1000 μm long) and Fresnel reflection at the semiconductor/air interface, provide sufficient feedback to make up for the losses thanks to which the laser

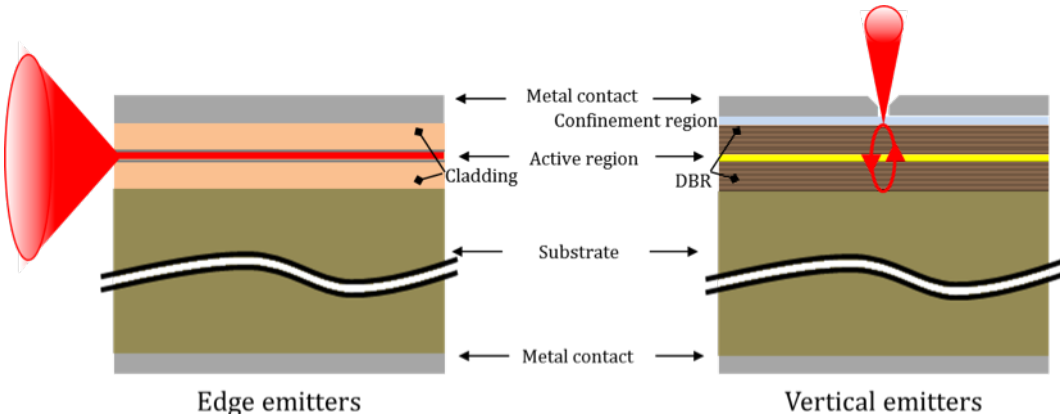

Figure 1.1: Diagram of conventional edge- and surface-emitting lasers. DBR: distributed Bragg reflector.

can achieve up to some Watts of output power. At the same time, however, the output beam becomes asymmetric and highly divergent, which would require, for instance, a correcting lens if coupled into an optical fibre.

In contrast, in vertical-cavity surface-emitting lasers (VCSELs), demonstrated for the first time in continuous wave in 1989 [16], the emission is normal to the substrate of the chip. The gain region is composed of several quantum wells with high material gain, but limited to a few percent modal gain per pass owing to their very narrow thickness, which is around 10 nm. Given the very short gain region, highly reflective distributed Bragg reflectors (DBRs) are grown monolithically on the substrate and on top of the active region to satisfy the laser threshold condition. VCSELs are pumped electrically, with an aperture in the top current injection contact of a few μm radius, limiting the output power to $\sim$10-100 mW [17], taking also advantage of fundamental transverse mode operation. The current injection aperture can be increased for a higher output power, at disadvantage of a poorer beam. Since they emit vertically, VCSELs can be also integrated in a two dimensional array with millions of components per centimetre squared, scaling the total output power up to a hundred Watts [18, 19]. VCSELs are still being developed for high density data interconnects in computer chips and other applications that require electronics miniaturization.

1.2 Introduction to semiconductor disk lasers

The surface-emitting technology later evolved to address one of the major challenges for semiconductor lasers: how to deliver a laser output that combines high power and low divergence, resulting in the development of vertical-external-cavity surface-emitting lasers (VECSELs) [5] . Unlike VCSELs, the laser standing wave is allowed to resonate in a free-space region as one gain mirror is external to the active layers [5, 20, 21]. VECSELs benefit from the macro-cavity design of solid-state lasers, and combine them with the gain properties of semiconductors.

The thin-disk architecture of solid-state lasers was introduced in 1993 [22, 23], conceived to manage the heat deposited in a high-power, thin-disk solid-state gain medium. Thanks to this analogy, semiconductor disk lasers (SDLs) terminology has therefore been adopted as an alternative to VECSELs and will be hereafter used in this manuscript. Also, being a semiconductor, the gain region material absorbs the pump intensity within a few micrometers, simplifying the focusing optics geometry for an efficient single-pass pump absorption. The unique combination of properties such as high output power, good beam quality, broad tuneability, narrow-linewidth emission, allow SDLs to be applied in many other technology fields, improving the quality and compactness of the design. In contrast to VCSELs and with the exception of a few demonstrations of electrically-pumped SDLs [24], SDLs do not include electrical contacts for pumping as they can be optically-pumped by an external source. By optical pumping, the distribution of the excited carriers can be uniform over the active area. Also, scaling the pumping area for higher output power requires matching the cavity mode inside the resonator for fundamental spatial mode operation. This can only be accomplished by adjusting the cavity length; hence an external cavity needs to be set up. SDLs are very versatile in this sense; the gain region, composed of several quantum wells, is monolithically grown on top of a single DBR and the extended cavity, from a few centimetres to a meter long, allows the inclusion of multiple elements for wavelength tuning, single-frequency operation, and pulsed operation with saturable absorbers.

Unlike VCSELs, SDLs have one DBR omitted and replaced by an high-reflective

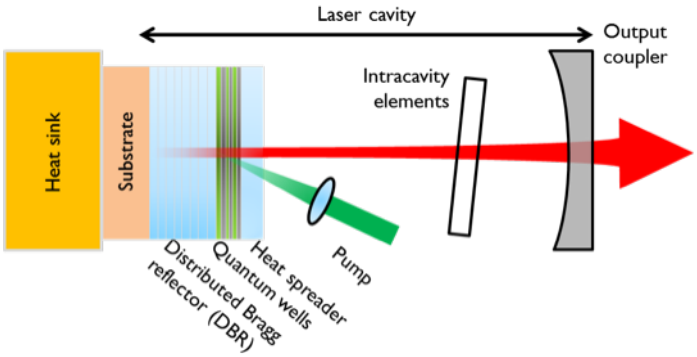

Figure 1.2: Schematic representation of an SDL gain mirror incorporated as an optically-pumped end-mirror within a standing-wave laser cavity,

mirror in the free space as schematized in Fig.1.2. On one hand, as the low gain limits the total loss to a few percent, the reflection and optical absorption loss must be maintained as low as possible for output coupling of few percent. On the other hand, as result of low output coupling, the higher intracavity power enables highly efficient frequency conversion with the insertion of nonlinear material, shifting the emission spectrum towards difficult wavelengths.

The first SDL was demonstrated in 1997, with gain structure based on quantum wells of InGaAs emitting in the spectral region around 1 μm with output power of 500 mW [4, 5]. Since then, the SDLs development have accelerated and growth techniques improved that nowadays InGaAs SDLs became the most established materials, making them capable of emitting directly several tens of output power [25–27] and thus suitable for highly efficient frequency doubling in the visible in commercial laser systems available at Coherent Inc. [8, 28].

Quantum wells can now be engineered for direct emission from the red to the infrared using different materials -with the most recent review in Guina et al. of Ref. [7]- as shown in Fig. 1.3, but the rest of the SDL structure (substrate, DBR) has to be designed accordingly in order to allow efficient stimulated emission at the desired wavelength, but impeding SDLs from operating efficiently at some other spectral regions. For example, the fundamental wavelength operation of InGaAs-based SDLs can be changed from 920 to 1180 nm by increasing the indium content at the advantage of higher strain for

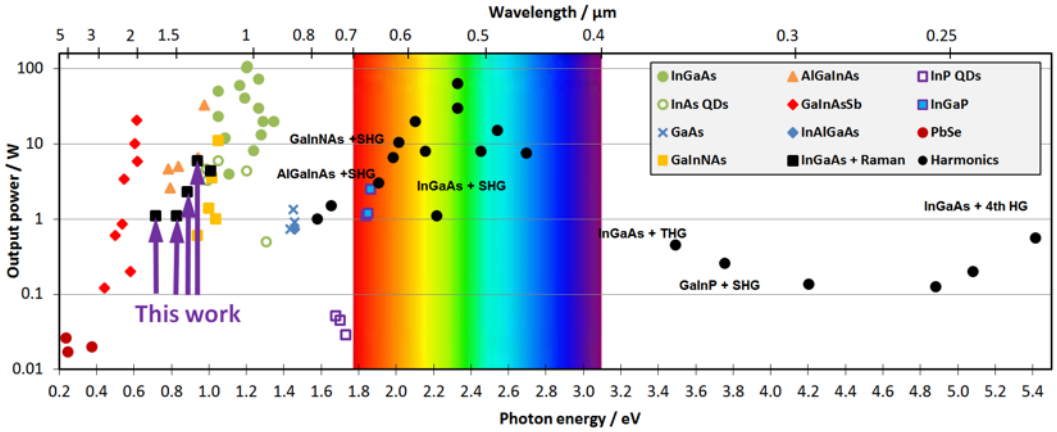

Figure 1.3: Maximum output power versus wavelength emission covered by CW SDLs via direct emission and frequency conversion. Figure of courtesy of Jennifer Hastie.

higher gain, but at the greater expenses of the growth quality due to the longer lattice constant, making it difficult a low-defect monolithical growth over the GaAs substrate. Reaching the near-infrared region between 1.2-1.55 μm has been accomplished with more complex epitaxy techniques by inserting layers of InAs quantum dots [29] or very low concentration of nitrogen in the well [10, 11].

Alternatively, the quantum well design of GaInAsP active layer for emission around 1.55 μm can be either implemented on InP substrates, and this was demonstrated first in VCSELs [12] via different bonding technique with AlAs/GaAs DBR mirrors, such as wafer fusion process [30–32]. Wafer fusion is a relatively complex fabrication technique that bonds two materials otherwise very difficult to grow monolithically due to the great difference between the substrate and the QW lattice constant, this will be reviewed in more details in Chapter 2.

Whereas wafer-fused SDLs have demonstrated to operate efficiently in the eye-safe wavelength region, in particular 1.3 μm, 1.48 μm and 1.58 μm [13, 33], SDLs are also so versatile that same wavelengths target can be addressed by using more simple laser-active structures and converting the wavelength within an external nonlinear material, such as a Raman crystal.

1.3 Introduction to Raman lasers

Stimulated Raman scattering, which is the base of Raman lasers, is a practical approach with which the pump laser is converted towards longer wavelength with a fixed Stokes shift [34], and this can be repeated in cascade for even longer wavelengths as long as the intensity of the intracavity fields is high enough to reach the threshold at each Stokes order wavelength [34]. The infrared region is achieved by more traditional optical parametric oscillators (OPOs), but these require birefringent or quasi-phase matching techniques due to the $\chi^{(2)}$ nonlinear characteristic of such devices. On the other hand, Raman crystals, based on $\chi^{(3)}$ nonlinearity, have always a phonon mode oscillating at the Stokes wavelength that conserves the momentum independently of temperature, which offers a key advantage to obtain a diffraction limited output from an aberrated pump beam, and allows automatic broad tuning of Raman laser wavelength as long as the pump is tuneable. Further details of the Raman laser physics will be given in Chapter 3.

First demonstration of a SDL-pumped Raman laser was reported at the Institute of Photonics by Parrotta et al. using a commercial InGaAs SDL and a KGW crystal for Raman laser emission near 1180 nm [35], which also reported the first continuous-wave cascaded Raman laser made possible by the broadband coatings.

Raman lasers have been a very intense field of research at Macquarie University in Australia, with several new results published every year, pioneering demonstrations of cw Raman laser using diamond up to the second-Stokes order (see for example Refs. [36, 37]). However, wavelength operation towards higher Stokes orders has been the domain of high-energy pulsed lasers. SDLs, on the other hand, have a high-finesse resonator, making them highly suitable for efficient cascaded Raman conversion even in cw operation.

The rapid development over the last decade of their properties, SDLs have become very attractive for a range of laser applications that require single-frequency and tuneable operation in the near infrared, such as molecular spectroscopy and gas sensing. Indeed, the low-noise and narrow-linewidth feature of SDLs have attracted commercial

interest (e.g. Innoptics [38]) to replace standard Ti:Sapphire laser source for such applications at 1 μm and 2.3 μm. Laser operation in the in the local minimum of water absorption spectral region (1.7 μm) from compact, highly coherent SDLs would benefit new medical imaging applications (e.g. optical coherence tomography [39]), as well as remote gas sensing and LIDAR.

1.4 Thesis outline

Here we propose to utilize an SDL with a Raman material to reach tuneable wavelength operation around 1.4 and 1.7 μm with narrow emission. The following chapters will review the relevant technical background required for this work.

Chapter 2 will focus on SDLs, describing the design and thermal management required for high-power operation. A review of the SDLs spectral coverage and potential applications will be also given in more details.

Chapter 3 will give an overview of the most important Raman laser principles and how to implement Raman crystals into the SDL cavity for wavelength conversion. This chapter also introduces in more details two materials used for this work: a synthetic diamond for its unrivalled thermal properties and largest Raman shift, important to reach first Stokes wavelength operation at 1.4 μm, but limited to reach the second Stokes wavelength (1.7 μm) due to the difficulty of depositing, at the time of the experiment, broadband anti-reflection coatings on diamond; and $KGd(WO_4)_2$ (or KGW), with shorter Raman shift but capable of accessing the 1.7 μm region via cascaded Raman conversion thanks to the availability of broadband coatings.

In Chapter 4, access to the 1.4 μm wavelength region will be demonstrated via a tuneable SDL-pumped diamond Raman laser as alternative to the wafer-fused counterparts. The emission at 1.4 μm will be accessed by a single Stokes shift of a 1.18-μm InGaAs-based SDL.

In Chapter 5, the work will extend the SDL wavelength accessibility to the 1.7 μm region for the first time, using cascaded Raman conversion in KGW. Despite a shorter Raman shift than diamond, the quality of broad-band anti-reflection coatings

on this crystal will enable extendibility to the long-wavelength region via the first demonstration of three Stokes shifts in a CW crystalline Raman laser.

Finally, in Chapter 6 a summary of results and comparison between the two Raman crystals will be given, describing possible application and future work.

Chapter 2

Semiconductor disk laser

2.1 Design and principles of operation

The SDL structure is composed of two main parts: the active region and the distributed Bragg reflector (DBR). A scheme of the design and the principle of operation are illustrated in Fig. 2.1.

The active region is made by a set of several quantum wells grown monolithically on top of the distributed Bragg reflector (DBR). The laser photon energy is chosen by appropriate selection of the quantum well composition that gives similar bandgap energy. With a total thickness of few microns, the whole active region can absorb most of the pump power [4, 40]. In the case when the barriers are pumped, the energy difference between the pump and the emitted photons determines the amount of energy that is converted into heat. The increased temperature affects the emission wavelength, and thus design criteria must consider the temperature change. The laser emission is almost totally reflected by the DBR ($R > 99.99\%$). Also, the quantum wells are arranged at the antinodes of the laser standing wave to maximize the gain. This configuration is called resonant period gain and also helps to avoid spatial hole burning [41]. The external mirrors are aligned to match the resonating cavity mode with the pump focus size and hence optimize the laser efficiency. To impede the carriers from flowing to the surface of the structure and to limit non-radiative recombination, a confinement window layer with high bandgap is grown on the top of the device. Furthermore, to

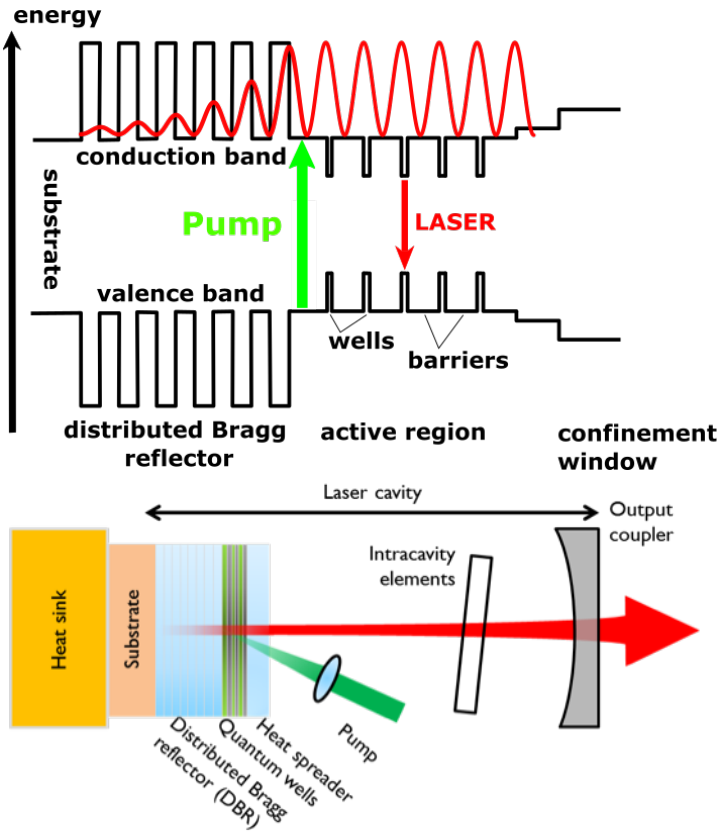

Figure 2.1: Schematic representation of an SDL. *Top*: semiconductor bandgap structure in the active region. *Bottom*: the SDL gain mirror incorporated as an optically-pumped end-mirror within a standing-wave laser cavity, cooled via a transparent crystalline heatspreader and heatsink.

avoid oxidation from the external environment, a final aluminium-free window layer caps the whole structure.

SDLs are grown epitaxially on a semiconductor substrate via metallic organic chemical vapour deposition (MOCVD) or molecular beam epitaxy (MBE). Depending on the target emission wavelength, most mature SDLs are grown monolithically. When this is not possible (see Section 1.2.4) some alternatives, other than nonlinear frequency conversion, include wafer fusion bonding of the DBR to the gain region, adding more complexity and costs to the fabrication process.

2.1.1 Active region

The active gain section of a SDL contains multiple quantum wells, positioned exactly at the antinodes of the operating laser wavelength for maximum gain extraction and minimum spatial hole burning. This geometry is called resonant periodic gain (RPG) [41, 42]. Each quantum well is sandwiched between two semiconductor barrier layers of different material with higher bandgap and is engineered to define the transition energy and hence the wavelength of emission of the SDL. The Fabry-Perot subcavity between the semiconductor interface and the DBR can be designed to form a resonant or anti-resonant configuration. In a resonant design the anti-node of the standing wave is at the semiconductor surface, maximizing the confinement factor thus enhancing gain while reducing the threshold. In an anti-resonant configuration, in which the node is instead located at the semiconductor surface, the confinement factor is instead reduced, favouring broader gain bandwidth and thus broad wavelength tuneability, at the cost of lower gain and higher threshold than in the resonant case [43].

Two ways of optically-pumping the SDL exist: in-well pumping and barrier pumping. As the pump is fully absorbed in a single pass by the gain region, the barrier pumping is the most preferred option. During pump absorption, the electrons are promoted from the valence to the conduction band and, upon non-radiative transition to the lowest level of the quantum well, the carriers are ready for radiative decay to the valence band, either spontaneously or by stimulated emission. The offset of the conduction band should be also large enough to forestall leakage of electrons from the quantum well back to the barriers. Whereas pumping the barriers is relatively simple, the energy difference between the pump and the laser photon energy (i.e. quantum defect) generates heat in the medium, thus increasing the temperature of the device. In-well pumping, on the other hand, has the advantage to reduce the quantum defect. However, pump absorption occurs only in a very limited portion of the active region as the quantum wells cover around 100 nm in total, against few micrometres during barrier pumping. To enable higher pump absorption, in-well pumped SDLs are designed such that the DBR is also reflective at the pump wavelengths for multi-pass configurations, but this adds another step to the fabrication process [44].

During barrier pumping regime, the control of the transition energy must also be performed considering the temperature of the device during laser operation. As the heat is transferred to the material by optical pumping, the bandgap reduces, the lattice cell dilates and, consequently, the energy states within a quantum well becomes dependent on the temperature following Varshnis equation [45]. As a practical result of this, the higher the intensity of the pump, the longer the emission wavelength. Wavelength shifts of the gain and the subcavity resonances must therefore be taken under consideration in the design criteria for further optimization.

The SDL active region can be designed for laser wavelength emission from 650 nm to 2.8 μm with III-V group materials, with a few low-power demonstrations using IV-VI materials (lead salt) for emission in the 4-6.5 μm range [46–48]. In addition to quantum well-based SDLs, there are several demonstrations of SDLs based on quantum dots embedded in quantum wells, allowing spectral extension towards those wavelengths that require semiconductor alloy compositions beyond the strain tolerance of the material [49].

2.1.2 Strain

Bandgap engineering begins with the material selection of quantum wells and barriers. The $\mathbf{k} \cdot \mathbf{P}$ analysis of the energy-band structure identifies in semiconductors the energy dispersion of electrons and holes in the conduction and valence band. Depending on the atomic composition, the transition from between two permitted energy bands can be either direct ($\Delta k = 0$) or indirect ($\Delta k \neq 0$). In indirect bandgaps (e.g. Si) the transition of an excited electron to the valence band is assisted by the addition of a phonon momentum (k-wavevector), which is an inefficient process for laser emission. In contrast, direct bandgap materials (e.g. GaAs, InAs) gather the most attention for optical applications as the photon absorption and emission does not involve the phonon momentum.

The energy bandgap of a binary compound in bulk state depends on the atomic species at a fixed temperature. When two binary compounds are mixed to form a ternary or quaternary, the lattice constant varies by changing the relative amount of

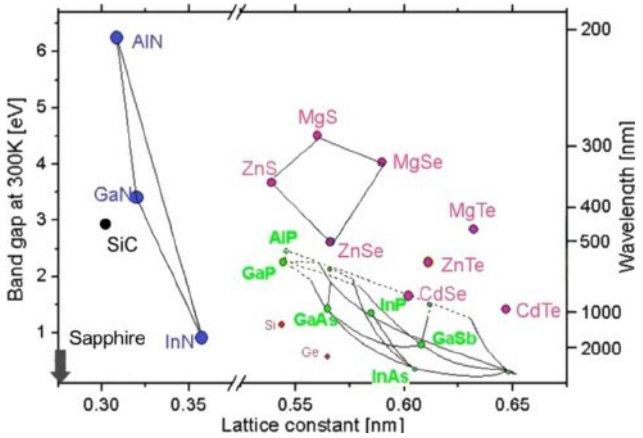

Figure 2.2: Bandgap energy diagram with lattice constant for commonly used semiconductor lattice compounds. Image from [50].

atoms, which can be expressed by the weighted sum of each binary compounds lattice constant in their relaxed form (Vegards law). The corresponding bandgap energy of the simplest case of a ternary compound varies accordingly as

$$E_{A_xB_{1-x}C} = xE_{AC} + (1-x)E_{BC} - x(1-x)b \tag{2.1}$$

where E_AC and E_BC are the energy gaps of the AC and BC compounds alone, while x is the mole fraction and b is the bowing parameter that diverts the linear trend to a quadratic one due to perturbations established by the two structures. The lattice constant dependence of the bandgap energy is illustrated in Fig. 2.2.

The lattice constant should be chosen to match the substrate to limit the amount of defects that worsen the luminescence efficiency. For most SDLs working in the visible and near infrared spectrum, the appropriate substrate for lattice-matched epitaxial growth is typically GaAs. Lattice matching can be still obtained under a minimum strain, which is produced by the relative difference between the substrate and the epilayer lattice constant. If the lattice constant of the layer is smaller than that of the substrate, the layer is under tensile strain; otherwise the strain is compressive. Small amounts of strain can be accommodated elastically up to the critical thickness [51]. Typically, the tolerance acceptance range of the lattice mismatch is below around 3.5% for stable layers [52]. Beyond the critical thickness, it becomes energetically favourable

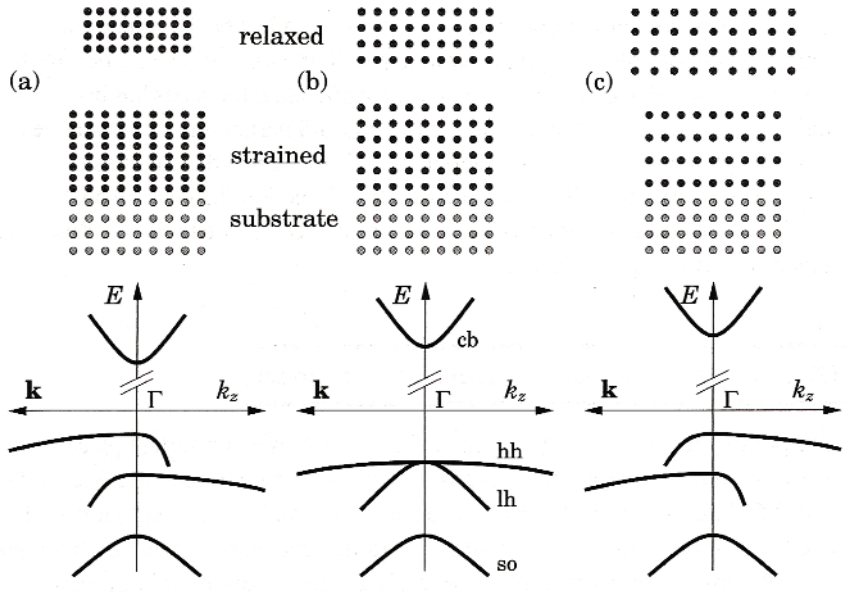

Figure 2.3: Scheme of the energy band-gap in a quantum well under (a) tensile strain, (b) relaxed (or bulk), and (c) compressive strain. k_z is the growth direction wave-vector module; k is the in-plane wave-vector (Image of ref. [55]).

to form dislocations. Strain can be also advantageous in reducing the threshold and polarizing the gain according to the laser beam direction [53,54]. The band structure of a bulk semiconductor can be approximately represented around the direct bandgap as per the diagram of Fig. 2.3. As shown in Fig. 2.3(b), with no strain the ground state is populated by the heavy holes, whose band dispersion symmetry does not match the conduction band due to different effective mass. Under compressive strain [Fig. 2.3(c)], the lattice symmetry is distorted in the plane and the degeneracy of the heavy and light holes at the Γ point of the valence band is removed so that the heavy holes band dispersion is lifted and becomes similar to the conduction band. Since the density of state is proportional to the carriers effective mass, compressive strain reduces the number of carriers required for population inversion, thus decreasing the laser threshold.

Due to lattice distortion produced in quantum wells, strain also favours stimulated emission with a certain polarization as the electronic transition is governed by the selection rules. In general, the wave functions that describe the top of the valence band are p-like orbitals as illustrated in Fig. 2.4 [54]. With no strain, the transition from

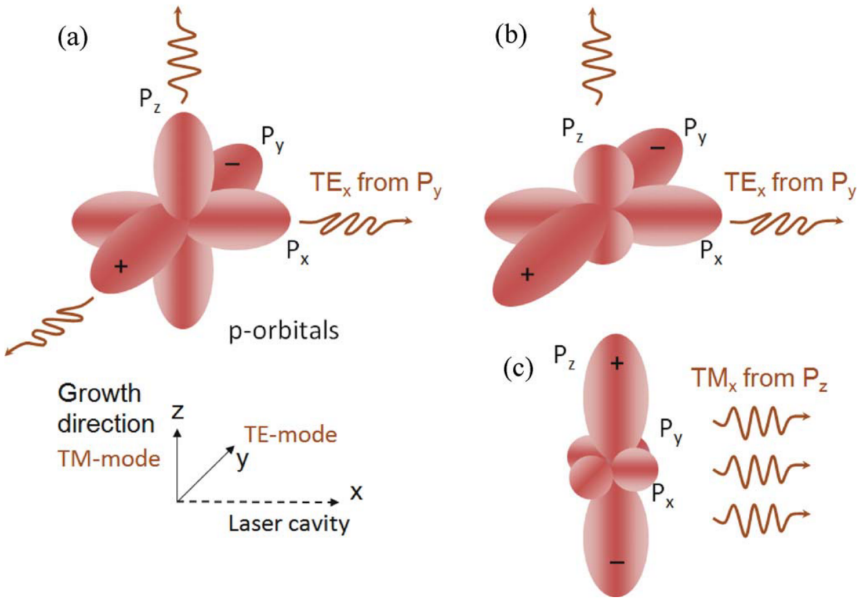

Figure 2.4: Representation of the p orbitals and TE and TM emission with (a) no strain, (b) compressive strain, and (c) tensile strain. Image from [54].

the s-like conduction band to the p-like valence band produces a photon whose electric field is polarized in the plane of the layer (i.e. TE mode). Tensile strain leads to decrease the lattice constant in the growth direction, z, enabling electronic transition with electric field polarized along the growth direction (i.e. TM mode). On the other hand, compressive strain is exerted along the x and y axis, favouring TE-polarized gain stronger than the TM gain. As SDLs are vertical emitters, quantum wells are therefore required to be compressively strained.

The total strained layers in a device may add up to be larger than the critical thickness with strain compensation. This is obtained by incorporating layers of opposite strain to reduce to zero the stress throughout the heterostructure [56]. Strain compensation is widely employed in many SDL devices to ensure high quality crystal growth throughout the structure.

2.1.3 Distributed Bragg reflectors (DBR)

The DBR is a multilayer dielectric mirror grown monolithically on the substrate as a pattern of $\lambda/4$-thick layers, alternating two different materials with high and low

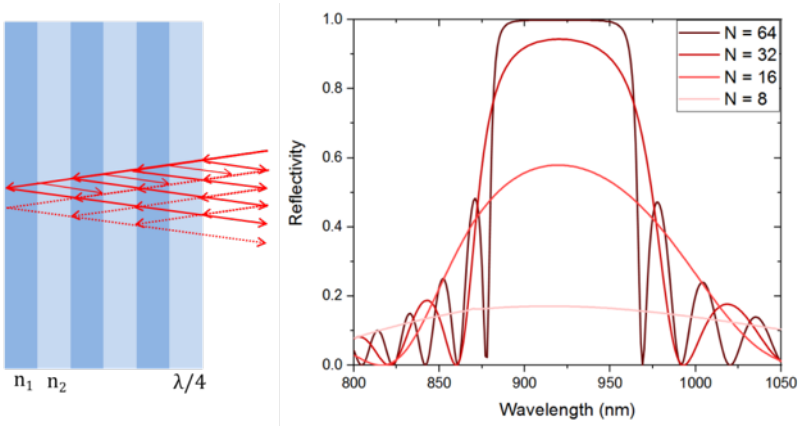

Figure 2.5: (left) Alternating layers of different refractive index to form the DBR; (right) reflectivity of the DBR by changing the number of layers.

refractive index [Fig. 2.5 (left)]. The quarter-wave thickness ensures that the reflections at the interfaces between the layers constructively interfere to achieve high reflectivity (Bragg condition).

The deposition of two layers with high index contrast, defined by $p = n_{low}/n_{high}$, achieves high reflection over a broad range of wavelengths. To reach reflectivity close to $\simeq 100\%$ several repeats are required, typically between 25 and 30 given the refractive index contrast achievable with III-V semiconductors. The reflectivity spectrum can be modelled with the transfer matrix method [57], and an example of the result is shown in Fig. 2.5 (right). The peak reflectivity, R, can be taken as an effective value for considering the DBR as single mirror. The bandwidth, $\Delta\lambda$, defines the wavelength range of high reflection. Effective reflectivity and bandwidth are given respectively by [57]:

$$R = \left(\frac{1 - qp^{2N}}{1 + qp^{2N}}\right)^2 \tag{2.2}$$

$$\Delta\lambda = \frac{4\lambda}{\pi}\arcsin\left(\frac{1-p}{1+p}\right) \tag{2.3}$$

Where $q = n_{in}/n_{out}$ is the refractive index ratio of the incident and the emerging light; λ is the central wavelength; N is the number of pairs. High-reflectivity and broadband DBRs therefore require multiple stacks of high-index contrast layers.

Combining high and low-index materials is not the only design consideration for

a high-performance DBR. To avoid thermal issues, DBRs should be also transparent to the pump and the laser wavelength. The layer number should be optimised to balance high thermal conductance, which decreases with N, and the high-reflectivity. For instance, GaAs/AlAs DBRs are well known for their high thermal conductance, high refractive index contrast, and they are grown lattice-matched to GaAs substrates for laser operation within the ∼900-1200 nm wavelength range. Below 900 nm, however, absorption in GaAs becomes an issue, and AlGaAs must be used with increasing Al content at the expense of reduced refractive index contrast and reduced conductivity. For gain materials lattice-matched to InP, an InGaAsP/InP (or AlGaAs/GaAs) DBR is suitable for laser operation within 1320-1550 nm [12] (or 670-850 nm [6]) but the low-index contrast requires a thicker DBR and hence a lower thermal conductivity. Conversely, high-index contrast materials of only 20-25 pairs of AlAsSb/GaSb layers can be deposited for laser operation in the 1.8-2.8 μm range, but, due to the increased thickness, the low thermal conductivity limits the performance [58, 59]. Thermal issues in DBRs can be addressed by reducing the thickness and including metallic layers of Al, Ag, or Au to compensate for the lower reflection [60]; bypassing the DBR using a transparent heatspreader on the intracavity surface (see Section 1.3); or with the fabrication of a DBR-free SDL [61].

2.1.4 Wafer bonding of DBR for >1.2 μm emission

One of the most critical issues in developing a long-wavelength SDLs has been the low quality DBRs that can be grown monolithically. As seen above, for example, InGaAs SDL emitting above ∼1200 nm would require too high lattice mismatch between the active region and the GaAs substrate, incurring an unreasonable number of point defects that increase the non-radiative carrier recombination rate. In particular, SDL operation in the 1250-1700 nm wavelength range can be achieved using InGaAs quantum well with lattice constant close to 0.6 nm (see Fig. 2.2) with InP substrates. At such lattice constant, however, there is not a suitable DBR with sufficient high refractive contrast and modest thermal conductivity that can reasonably balance the performance.

The wafer fusion technique can assemble two semiconductor compounds of un-

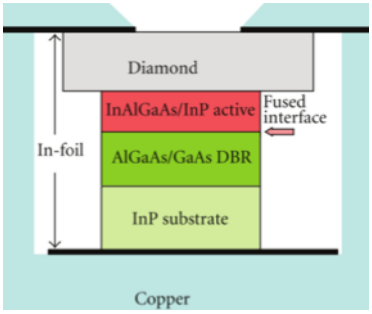

Figure 2.6: Schematic of a wafer-fused gain mirror for an InAlGaAs/InP-based SDL. Indium foil is applied to ensure good contact with the copper heatsink. Image taken from [13]

matched lattice constant that cannot be grown monolithically, such as GaAs and InP. Wafer bonding is a relatively complex process that can be attained by various methods, among which are fusion bonding, hydrophobic bonding, hydrophilic bonding and UHV bonding [62–65]. The gain assembly of an SDL is schematically illustrated in Fig. 2.6 from Ref. [13]. Unlike monolithical epitaxial growth, wafer fusion adds more steps and complexity to the SDL fabrication cycle.

Nevertheless, this technique has been adopted for fabrication of telecom VCSELs as well [12]. More recently, the wafer-fusion process integrated AlGaInAs/InP quantum wells with high-quality AlGaAs/GaAs DBRs to produce SDLs with output power greater than 30 W at 1275 nm [66], 5 W at 1140 nm [67], and 4.7 W at 1580 nm [68].

2.2 Thermal management

The absorption coefficient in semiconductor materials is about three times higher than in solid-state gain media. For similar pump spot size, the heat density generated in SDL materials is a thousand times higher than in standard solid-state lasers and thereby thermal management is required to maintain high the efficiency of SDLs [5,69]. Effective thermal management is therefore essential to extend the pump power tolerance.

The main challenge of thermal effects in SDLs originates from the temperature-induced spectral shift of the QW photoluminescence and the change of the optical thickness in the active region. On the one hand, the photoluminescence peak of the

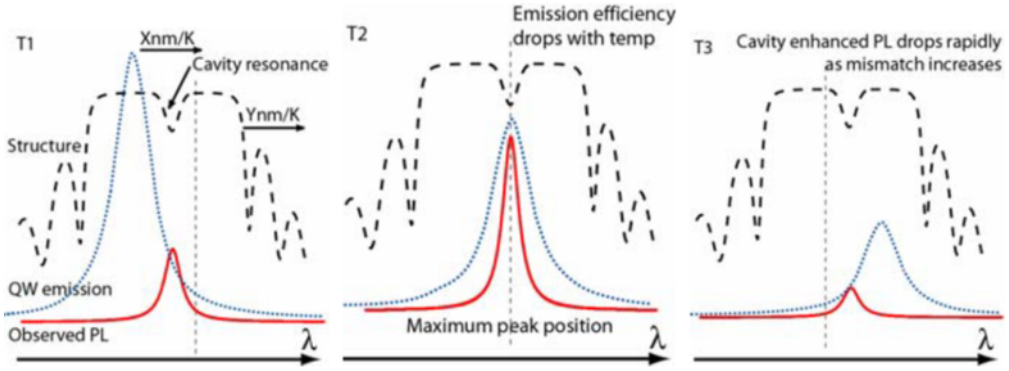

Figure 2.7: Evolution of the quantum well emission (blue dots) and resonantly-enhanced photoluminescence (red), shown with respect to the reflectivity spectrum (dashed) at three different stages of temperature of the SDL (T1, T2 and T3). Image taken from Ref. [70].

QWs shifts towards longer wavelengths at a certain rate (nm/K) as this is dominated by the bandgap shift with the temperature [45]. On the other hand, the temperature rise is also responsible for the RPG shift at a different rate, since the refractive index increases with the temperature. Figure 2.7 illustrates the QW spectral emission while walking through the subcavity resonance at different temperatures. Therefore, in active region design, the cold quantum well peak wavelength has to be offset with some nm to be matched with the RPG wavelength at the working temperature [70]. Once the QW emission wavelength mismatches the subcavity resonance at relatively high pump intensity, the SDL output power drops in what is called thermal rollover. Thermal management for extending the pump power range before thermal rollover occurs is of paramount concern in SDLs.

Other than mounting the SDL chip on a heatsink (typically brass or copper) kept at constant temperature to remove the heat, two more sophisticated approaches can be implemented to manage the heat: thin device and heatspreader device - illustrated in Fig. 2.7 [71]. If the device is simply taken as grown and actively cooled to the heatsink, the heat generated by the pump flows through the DBR and the substrate, whose thermal resistivity, if high, impedes the device from cooling and thus reaching high efficiency. Alternatively, the substrate can be etched [4] so that the active region is in direct thermal contact to the heat sink, but this requires the wafer sample to be

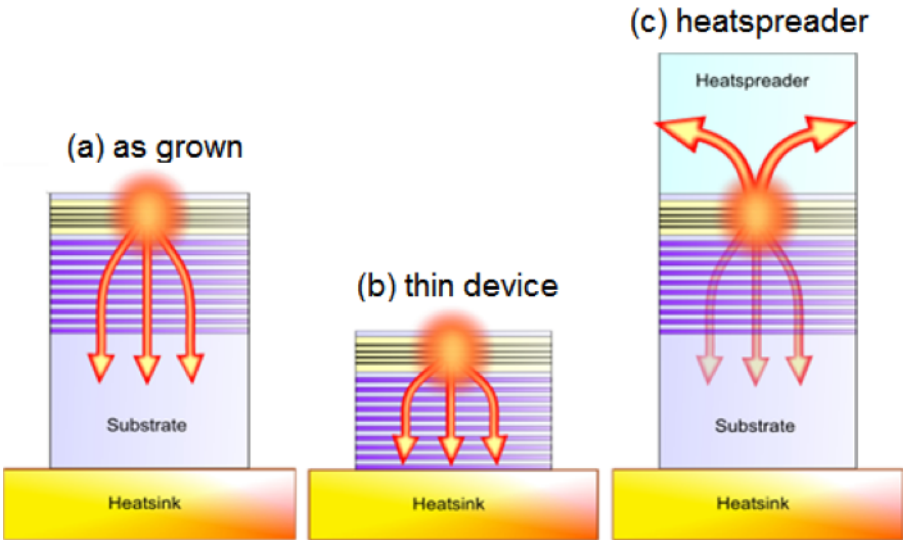

Figure 2.8: Thermal management techniques for SDLs. Image taken from [71].

processed further, making the fabrication procedure more complicated. Commonly, the chip is left as grown and bonded to a transparent heatspreader on the surface. With this method [72], using a high-thermally conductive material, the heatspreader extracts most of the heat from the top, creating a highly efficient SDL. Whereas crystals such as SiC [73] and sapphire remove the heat relatively efficiently, diamond is so far the best material for thermal management [69] thanks to its unrivalled thermal conductivity of about 2000 K/Wm, against 500 K/Wm for SiC and 0.046 $\mathrm{Wmm^{-1}}K^{-1}$ for sapphire. Nevertheless, achieving uniform bonding via liquid capillarity [74] to establish thermal contact at the atomic scale between the heatspreader and the SDL is also critical for efficient heat extraction.

2.3 Wavelength coverage

The bandgap energy modulation of the quantum wells as seen in Section 1.2 allows engineering SDLs for direct emission from 665 nm to 2800 nm [6, 75]. The emission wavelength must be within the stopband reflectivity of the DBR ($R > 99.9\%$), along with lattice-matching and good thermal resistance. However, the DBR and active region cannot be always grown together for any desired wavelength due to the limited

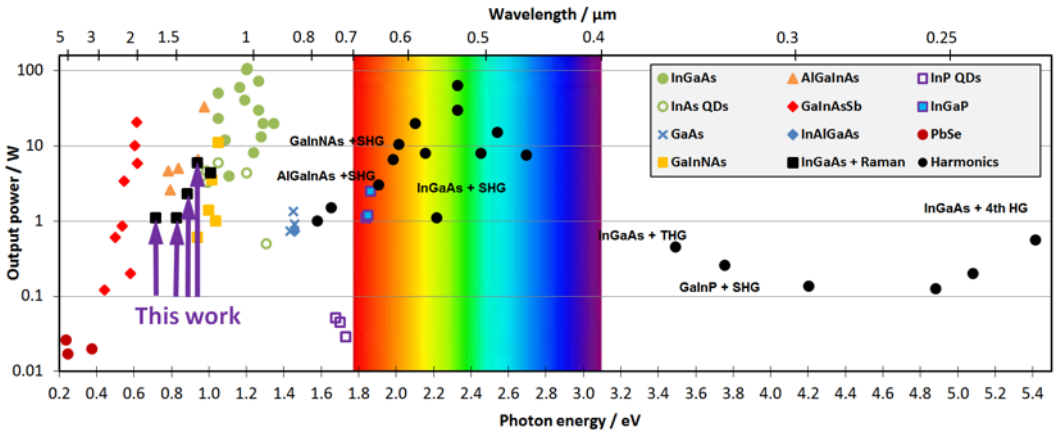

Figure 2.9: Maximum output power versus wavelength emission covered by CW SDLs. Figure of courtesy of Jennifer Hastie.

availability of the material compounds and the pump source. Figure 2.9 plots the maximum output power and the relative wavelength emission of most continuous-wave SDLs reported using different gain materials. With the help of the most recent review published by Guina et al. [7], Table 2.1 summarises the material compositions used for SDLs to date.

Whereas the emission wavelength is generally defined by the whole design structure of the subcavity, the maximum output power depends mostly on external factors, such as thermal management approach, growth quality of the gain structure, cavity mode, pump power, and output coupling.

It can be seen that most SDLs provide direct emission in the near-mid infrared spectral region (0.92-1.5 μm) with several Watts of output power; while visible SDLs are limited to the red region of around 665 nm. Below 665 nm, it becomes more challenging finding an appropriate gain material that provides direct emission from the blue to the yellow-orange spectrum. The shortest direct wavelength was accomplished using an InGaN-based SDL emitting at 390 nm [76]. However, emission at such short wavelengths requires a UV pump source, which in this case is provided by a complex optical scheme and is not continuous-wave. Above 2800 nm, SDL active region of PbSe and PbTe have demonstrated operation up to 6500 nm in pulsed operation and at very low cooling temperature [48, 77], with just one exception of laser operation above room

Table 2.1: Materials compositions for direct emission of SDLs (after Guina et al. 2017 [7]).

Wavelength range (nm)	**Gain material**	**DBR**
360 – 540	InGaN/GaN	AlGaAn/GaN
630 – 700	AlGaInP/GaAs InP/GaAs (QDs)	AlGaAs/GaAs
700 – 800	GaAsp/GaAs InP/GaAs (QDs)	AlGaAs/GaAs
800 – 920	AlGaAs/GaAs AlInGaAs/GaAs InGaAsP/GaAs	AlGaAs/GaAs
920 – 1200	InGaAs/GaAs	AlAs/GaAs
1300 – 1500	Diluted-nitride InP/GaAs (QDs)	AlAs/GaAs
1250 – 2100	AlInGaAs/GaAs InGaAsP/GaAs	AlAs/GaAs (wafer-fused)
1900 – 3000	InGaAsSb/GaSb	AlAsSb/GaSb
3300 – 6500	PbSe/Si PbSe/BaF_2	PbEuTe/BaF_2

temperature [78].

When bandgap engineering is nontrivial for laser generation at a particular wavelength, ultraviolet, visible and infrared emission can be attained by other means. For instance, placing a $\chi^{(2)}$-type crystal cut for phase-matched second harmonic generation (SHG) within the cavity of an infrared-emitting SDL (e.g. lithium triborate (LBO), barium borate (BBO), or periodically-poled lithium tantalite (PPLT)) is advantageous in reaching the visible [6]. Intracavity conversion enables nonlinear conversion efficiency to the visible (or UV) that can be, at least in principle, as high as the optimum output coupling of the fundamental radiation. Likewise, emission towards the infrared spectrum can be accessed with the implementation of Raman active materials (focus of this work), such as diamond and tungstate-based crystals, as demonstrated for the first time by D. Parrotta et al. with a tungstate-based crystal in Ref. [35] and later with a diamond [79]. Unlike SHG, to enable Raman conversion and thus a Raman laser, the Raman crystal must be inserted within a doubly-resonant cavity designed for both the fundamental and the Raman wavelengths. Indeed, although crystalline Ra-

man media cannot be tuned as they have the spectral gain limited to a few or fraction of wavenumbers, the wide gain bandwidth of the SDL enables tuning of the SDL and thus, by Raman shift, the Raman laser tunes as well over a large wavelength span, only limited by the SDL gain bandwidth, which is typically around 300 cm^{-1}. More details on the Raman laser systems will be elucidated in Chapter 3.

2.3.1 Near-infrared (850-1730nm)

SDL emission in the 850 nm region is possible with binary quantum wells of AlGaAs. Hastie et al. of the Institute of Photonics, Strathclyde demonstrated SDL operation at 850 nm with 500 mW of output power, pumped by 2.5 W at 660 nm of a diode laser [73]. GaAs SDL output efficiency was improved up to 50% at the same output wavelength by in-well pumping, resulting 1.6 W output power [80].

InGaAs/GaAs structures offer laser operation at around 1000 nm and are the most efficient and reliable of those used for SDLs, leading the field thanks to the growth quality, output power, spectral features and pulsed operation. Indeed, such structures can emit directly multiple tens of Watts output power in continuous-wave and up to 40% slope efficiency. Chilla et al., for instance, demonstrated, with a relatively low content of indium in the quantum wells, InGaAs SDLs emitting maximum output power of 20 W at 920 nm [25]. A near-diffraction-limited 20-W output beam at 960 nm was also reported by Rudin et al. [26]. Heinen et al in 2012 reported the highest output power ever achieved from a single SDL chip: 106-W in a multimode beam at 1028 nm and 45% diode-to-SDL conversion efficiency [27]. For longer wavelengths, the high indium content in InGaAs strains the structure to the point that compensation layers of GaAsP at the nodes are added to balance out the total strain and allow efficient emission up to 1180 nm. Using this system, single-frequency operation at 1180 nm with a few Watts of output was demonstrated by Alford et al. in 2013 [81]. Strain compensation of a highly-strained InGaAs SDL enabled laser emission up to 50 W emitting at 1180 nm [82]. Longer-wavelength InGaAs-based SDLs are not reported yet, as higher indium content leads to a greater amount of point defects [83] and hence the growth quality of these devices is compromised.

Direct emission at wavelengths longer than 1200 nm is nonetheless possible with the incorporation of a small amount of nitrogen into the quantum wells. Hopkins et al. in 2004 demonstrated the first InGaAsN SDL, which operated at 1320 nm with 600 mW of output power, rolling over at a few Watts of pump power despite a relatively modest pump spot radius (75 μm) [10]. Low rollover point in this system could be due to the fast detuning of the cavity resonance over a reasonable small pump range. Operation above 1 W directly in the 1.2-μm region was later reached with an improved InGaNAs SDL structure [84, 85]. Moreover, when monolithic growth on a GaAs substrate is no longer feasible (with the exception of a demonstration at low output power with a monolithic 1550 nm SDL [86], wafer-fused SDLs are capable of reaching multi-Watt output power in the eye-safe spectral region, particularly at 1310 nm, 1480 nm, and 1550 nm [13, 33]. Very recently, Leinonen et al. demonstrated a SDL emitting at 1275 nm with a maximum of 33 W output power with heatsink temperature below 0°C [66]. The flip-chip configuration was very effective in removing the heat. Earlier, higher conversion efficiency of 59% from the same system was attained [87]; however, the same thermal management approach has not yet been reported for operation at longer wavelengths. When the quantum defect becomes higher at long wavelengths, the intracavity heatspreader method is preferred with a thermally resistant DBR. With an intracavity diamond heatspreader, emission at 1580 nm was demonstrated with 4.6 W maximum output power [68] and single-frequency operation at 1 W output power [88].

However, the complexity of the growth and the wafer-fusion process has motivated further research into more practical alternatives, such as the implementation of Raman-active materials to Stokes-shift the emission wavelength of most mature gain structures (InGaAs SDLs) towards the region accessed by monolithic GaSb-based SDLs (1.9-3 μm) [59]. In this regard, the first demonstration of Raman conversion of a commercialized InGaAs-based SDL was reported by Parrotta et al. [35] in 2011 at the Institute of Photonics. They implemented a potassium gadolinium tungstate crystal ($KGd(WO_4)_2$) in a partially-shared cavity within a 1040-nm emitting, InGaAs-based SDL to generate a tunable Stokes-shifted output centred at 1140 nm. Later, the same team reported, with the same SDL gain structure, output power of 4.4 W via intracavity Raman conversion

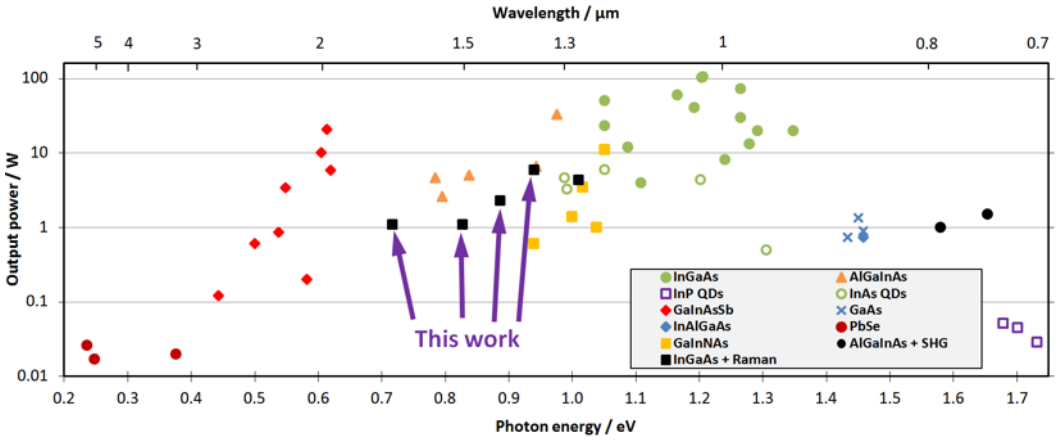

Figure 2.10: Output power of SDLs reported in the literature using a variety of III-V materials with the inclusion of PbSe.

with a higher-gain material, specifically a synthetic diamond, to target the 1230 nm spectral region [89]. Given the recent demonstration of high-power 1180 nm InGaAs materials [82], we exploited a synthetic diamond for intracavity Raman conversion to explore the eye-safe region. With this system we obtained 2.3 W output power at 1.4 μm with 0.1 nm FWHM linewidth. These results are reported in Chapter 5 of this manuscript as well as published in ref. [90]. During this work, we also demonstrated 1320 nm Raman laser operation at 2.7 W maximum output power via Stokes-shift of 1180 nm SDL [91] using a KGW as Raman medium. Another advantage of Raman laser is the possibility for generating longer wavelengths by multiple Stokes shifts in cascade. Intracavity cascaded Raman conversion of an SDL has not been reported prior to this work to the best of our knowledge. This manuscript reports for the first time, along with our report in ref. [92], a cascaded KGW Raman laser with output coupling at the three Stokes wavelengths: 1320, 1500 and 1730 nm, with maximum output power of 6.1 W at the first Stokes and 1 W at the second and third Stokes wavelength. Emission at 1730 nm from an SDL system also addresses the SDL spectral coverage gap, paving the way for potential application in the medical field, such as optical coherence tomography due to the high water transmission compared to the standard technology exploiting the less-transparent 1.5-μm region of water vapour [93–95].

Table 2.2: Most of near-infrared SDLs and relative gain composition (SHG: second harmonic generation; QD: quantum dot).

λ (nm)	Output power (W)	Gain material	Method	Reference
739	0.052	InGaP/AlGaInP	InP QDs	[96]
750	1.5	AlInGaAs/InP (wafer-fused)	SHG	[97]
785	1	AlInGaAs/InP (wafer-fused)	SHG	[68]
850	0.5	GaAs/AlGaAs	Direct em.	[73]
850	1.6	GaAs/AlGaAs	In-well pump	[80]
920	20	InGaAs/GaAs	Direct em.	[98]
980	40	InGaAs/GaAs	Direct em.	[98]
1028	106	InGaAs/GaAs	Direct em.	[27]
1064	60	InGaAs/GaAs	Direct em.	[99]
1119	4	InGaAs/GaAs	Single freq.	[81]
1140	12	InGaAs/GaAs	Direct em.	[100]
1180	50	InGaAs/GaAs	Direct em.	[82]
1200	1.6	GaAs/InGaAs/GaAsSb	Direct em.	[101]
1228	4.4	InGaAs/GaAs	Raman conv.	[89]
1255	4.6	InAs/GaAs (QDs)	Direct em.	[9]
1275	33	AlInGaAs/InP (wafer-fused)	Direct em.	[66]
1305	6.6	AlInGaAs/InP (wafer-fused)	Direct em.	[68]
1320	6.1	InGaAs/GaAs	Raman conv.	[102] (this work)
1400	2.3	InGaAs/GaAs	Raman conv.	[90] (this work)
1480	4.8	AlInGaAs/InP (wafer-fused)	Direct em.	[103]
1500	2.3	InGaAs/GaAs	Raman conv.	[102] (this work)
1580	4.6	AlInGaAs/InP (wafer-fused)	Direct em.	[68]
1730	2.3	InGaAs/GaAs	Raman conv.	[102] (this work)

2.4 SDL applications

The unique blend of low-noise, high-brightness output, single-frequency operation, and wavelength coverage, opens the door for many applications. For instance: in medicine,

continuous-wave yellow SDLs are being used in place of commercial pulsed dye lasers in dermatology [104], allowing treatment of the local disorder deeper and more accurately while an SDL operating around 1.7 μm could exploit the low-scattering and absorption in water to be potentially applied to medical imaging, such as optical coherence tomography [105]; in long-range sensing and lidar, a tuneable narrow-linewidth SDL source from the 1.5 to 1.8 μm wavelength could be used to probe several gas features through the water vapour transmission window. In the following paragraphs, a brief review of few commercial SDLs and potential applications will be further discussed. An initial application of SDLs was proposed in 2002 for pumping erbium/ytterbium-doped fibres for optical communication [106, 107], but commercialisation towards the telecom market was soon dominated by edge-emitting technology. Today, optically-pumped SDLs are commercially-available from Coherent Inc. at visible and UV wavelengths under the name of Optically-pumped semiconductor laser (OPSL), where they have developed highly reliable InGaAs-based SDLs with intracavity frequency doubling. Coherent supplies OPSLs from the UV to the green from 10 mW to 10 W output power to replace conventional and bulky gas and solid-state lasers (e.g. argon ion, doped vanadate) and make them portable for forensic and skin treatment applications [8, 28]. Yellow SDLs have indeed found many relevant applications in dermatology. Yellow (585 nm) radiation is employed for correcting skin lesions and aberrations as it is well-absorbed by superficial blood vessels [108]. Previously pulsed dye lasers were used; however, nowadays, CW yellow 577 nm SDLs are implemented in a medical product by Asclepion Laser Technologies for exploiting the maximum haemoglobin absorption [104]. With the emission in CW, medics can specifically cauterise blood vessels without causing collateral damage to surrounding tissues, as with pulsed lasers. More recently, the Optoelectronic Research Centre of Tampere University of Technology, in collaboration with INSERM, built the first unit that implements a CW 585 nm SDL [7].

Tuneable single-frequency SDLs in the near infrared are important for gas spectroscopy, of particular interest in sensing of atmospheric pollutants, such as methane, ammonia and carbon monoxide [109, 110]. Tuning the laser wavelength across the gas absorption spectrum identifies the particular molecular content. Low-noise SDLs with

narrow linewidth are commercialised by Innoptics, which develops and sells compact devices for spectroscopic application in the 1-2 μm range [38].

The first demonstration of high-sensitivity gas spectroscopy with an SDL was reported in 2004 by Gherman et al. with a mode-locked SDL (passively modelocked with a SESAM), where the frequency comb was matched to the one produced by the sample high-finesse cavity containing acetylene [111]. When compared to the standard Ti:Sapphire laser source [112], SDLs can access gas spectral region with higher resolution, thanks to the reduced frequency noise bandwidth in the sub-kHz range [113]. M Squared Lasers launched the first commercial ultrafast SDL, which operated in the 1 μm wavelength region for nonlinear microscopy in living organisms [114].

In the field of quantum technology, tuneable SDLs with ultra-narrow linewidth are now being exploited for atomic, molecular and optical physics applications. To achieve ultra-stable single-frequency operation, the SDL requires active stabilisation using a high-finesse external reference, typically a Fabry-Perot cavity or a mono-atomic gas. Recently, a frequency-doubled 571 nm SDL was demonstrated for cooling and manipulating trapped magnesium ions [115]. Also, Pabœuf et al. [116] at the Institute of Photonics reported a wavelength-stabilized AlInGaP SDL working at 689 nm with 6 kHz FWHM linewidth suitable for second stage cooling of strontium atoms in a magneto-optical trap.

2.4.1 Potential developments of long-wavelength SDLs for optical coherence tomography (OCT)

At wavelengths longer than 600 nm soft biological tissues become less absorptive and lasers find more applications in medical imaging. Depending on the tissue constituency, the absorption coefficient varies from 0.1 to 1 mm^{-1}, while scattering coefficients are in the 10-100 mm^{-1} range for incident light in the 600-1300 nm spectrum [3], which is also called therapeutic window [117]. Conventional lasers operating in the deep-red and near-infrared spectrum have been used as light sources for capturing high-resolution three-dimensional images via optical coherence tomography (OCT) [3].

An OCT scheme is based on the principle of operation of a Michelson interferom-

eter, in which a laser beam is split and sent to a reference and a sample arm. While the delay time of the backscattered reference beam emerging can be changed by moving the reference mirror along the beam propagation, the light experiences within the sample different refractive indices depending on the inhomogeneity of the biological tissue. The detector collects the highest intensity whereby the reference beam interferes constructively with the sample beam after a round-trip. This scan can be performed in the time domain while translating the arm of the reference mirror longitudinally, or in the Fourier domain [3, 118], with the advantage of a fixed arm while collecting the backscattered light with a spectrometer and thus reconstructing the tomographic image of the biological sample. The theoretical axial resolution, Δz at FWHM, of a Gaussian laser source can be written as [3]:

$$\Delta z = \frac{2\ln 2}{\pi}\frac{\lambda^2}{\Delta\lambda} \tag{2.4}$$

Where $\Delta\lambda$ is the FWHM of the laser linewidth operating at the centre wavelength, which is λ. Equation 2.4 also defines the coherence length, within which the beams generate the fringes. This is an important parameter that is required to detect different biological constituents in depth. Incidentally, the lateral (or in-plane) resolution is an independent factor that depends only on the probing laser properties and the optics of the OCT system used. This corresponds to the laser waist spot radius, or theoretically defined by [3]:

$$\Delta x = 2\sqrt{\ln 2}\frac{\lambda}{\pi\Theta} \tag{2.5}$$

where Θ is the diverging angle of the Gaussian laser beam. Also, the depth of focus (DOF) (or imaging range [93]) is an important parameter of the laser for imaging and is defined as equal to the confocal parameter, which is twice the Rayleigh range, that is:

$$\mathrm{DOF} = \frac{2\pi w^2}{M^2\lambda} \tag{2.6}$$

where w and M^2 are, respectively, the waist spot radius (or the transversal resolution) and the beam quality factor of a generic multimode beam. The higher the DOF, the

sharper the image in depth. It also important to note that there is a trade-off between lateral resolution and DOF, because a highly-divergent probe beam focuses very rapidly in a small diameter, with a corresponding excellent lateral resolution but with a short DOF. On the other hand, laser beams with low Θ focuses with a greater beam diameter but with a long DOF [119].

Many broadband light sources have been utilized for high-resolution OCT in the spectral-domain (SD-OCT). This includes superluminescent laser diodes, LEDs, Yt-terbium, Erbium, or Thulium-doped fibre lasers, photonic crystal fibres, and thermal tungsten halogen [3]. These light sources have access to the 675-1800 nm region with different bandwidths, between 10 and 370 nm FWHM, and thus different resolution depth, from about 0.1 to 20 μm [3]. Unlike such broadband light sources, narrow-linewidth tuneable lasers, on the other hand, take the advantage of higher resolution depth and higher scan rates when rapidly tuned. When they are implemented into an OCT, this becomes swept source OCT (SS-OCT) [120]. Rapid wavelength tuning allows very fast scanning rates over most standard SD-OCTs, reaching, for example, the MHz level using a 1 μm mode-locked laser [121].

Most commercial OCT systems employ laser sources with low numerical aperture (i.e. low Θ) to provide a good DOF of the order of the millimetres, and lateral resolution of $\sim$20 μm [119]. No SDL system has been reported yet for use in OCT imaging. When compared to the standard technology mentioned above, the continuous-wave SDL-pumped Raman laser beam in the 1.7 μm region we report in this manuscript (see Chapter 5) features similar properties to the current technology: DOF $\sim$ 3 mm, $\Delta x \sim 20$ μm, and $\Delta x \sim 20$ μm. In conclusion, broadly-tuneable SDLs may be included in the OCT technology as alternative for a few aspects: (i) CW operation and high-quality beam provide homogeneous probing beams throughout the tissues, avoiding uncontrolled effects for which high-power peak pulsed lasers may instead provoke; (ii) low-noise operation increases the laser tuning rate due the relaxation time falling within the nanoscale, in contrast to the standard solid-state sources, which are limited by long relaxation time of the excited carriers ($\sim\mu$s); (iii) great wavelength flexibility towards the high transmission window (1.5-1.7 μm) in water is best suited for penetrating more

into the biological tissue with lower scattering noise when compared to the common window centred at 1.3 μm [105, 122, 123].

Chapter 3

Raman laser

3.1 Introduction

The spontaneous Raman effect is the inelastic scattering of photons by molecules or a crystal lattice. The energy difference between the scattered and the pump photons is called a Stokes shift, which does not depend on the pump photon energy and thus characterises any Raman material. After demonstration of spontaneous Raman scattering in 1928 [124], for which Chandrasekhara Venkata Raman and Kariamanickam Srinivasa Krishnan won the Nobel prize, along with an independent experiment on crystals performed by Grigory Landsberg and Leonid Mandelstam [125], it was many years before the stimulated Raman scattering effect (SRS) was shown, following the first laser demonstration: in organic liquid cells in 1962 [126, 127]; in natural diamond and calcite [128]; and in gases, e.g. hydrogen and methane [129]. Since the outset of solid-state lasers, Raman lasers have been investigated as a practical tool for extending wavelength coverage. The wavelength shift is a fixed property of the material and is independent of the pump wavelength (hereafter called the fundamental) as long as the medium is sufficiently transparent to the fundamental wavelength. Typically SRS is used to reach spectral regions that are challenging to achieve directly from a practical gain medium.

SRS is a third-order nonlinear process that needs high-intensity pump fields to be observable, typically on the order of MW/cm^2. Unlike second-order nonlinearities, as

used in most optical parametric oscillators (OPOs), SRS can be said to be automatically phase-matched, and the key optimisation parameter is orientation of the pump field vector to the optical axis that maximises the Raman intensity. In the 60s, the knowledge of Raman polarizabilities was limited and the main approach to reach the threshold was to increase the pump intensity in the Raman sample.

Continuous-wave Raman laser operation was demonstrated in 1974 using long fused-silica fibres as amplifiers, typically characterised by a low value of Raman polarizability, enabling low-threshold laser emission by confinement of the CW pump over the long distance [130]. CW Raman fibre lasers nowadays fuel a modest portion of the laser technology thanks to the great adaptability of their properties to a wide range of laser applications [131].

In contrast, among solid-state Raman materials, achieving CW laser operation has been rather a difficult task due to the low average power. To compensate for low pump power, crystalline Raman media have to be enclosed in a high-finesse cavity for the CW regime, and the first demonstration had to wait several years for the fabrication of highly-reflective coatings to be developed [132]. A CW crystalline Raman laser was reported for the first time only in 2004 by Grabtchikov et al. [132]. They used an Ar^+ gas laser at ∼514 nm as a continuous source to pump a $Ba(NO_3)_2$ crystal and obtain a Stokes-shifted laser at ∼544 nm, well above the threshold. The high-finesse resonator enabled a high-intensity beam with low input power. Later, Demidovich et al. [133] developed a Raman laser pumped by a commercial diode source. In this study, a neodymium-doped $KGd(WO_4)_2$ crystal (Nd:KGW) was directly pumped at 808 nm to excite the Nd states for laser oscillation at 1167 nm and enable Raman conversion at 1180 nm within the same medium [133] (the description of this and other cavity setups will be later discussed in Section 2.4). In the same year, Pask et al. also demonstrated an intracavity-pumped Raman laser using a pure KGW crystal, reporting a low threshold of only 4 W [134]. These results were significant milestones in achieving cw operation with crystalline Raman media, and they demonstrated two key attributes: first, Raman lasers are capable of emitting multi-Watts of output power in the continuous regime with low pump power when arranged in a high-finesse cavity; second, when

$\chi^{(2)}$-type materials are also implemented, multiple wavelengths are possible throughout the visible and near-infrared via cascaded nonlinear processes, such as cascaded SRS and intracavity frequency mixing [36, 135].

The range of wavelengths attainable by these systems can be further enlarged if the fundamental gain material is a tuneable source, as tuning the fundamental wavelength automatically tunes the Raman wavelength due to the fixed Stokes shift. In fact, due to the natural narrow gain bandwidth in crystalline Raman media, crystalline Raman lasers are unsuitable for direct tuning. SDLs on the other hand are capable of broad tuning as their gain bandwidth is typically $\sim$300 cm^{-1} [5]. Also, being low-gain lasers, the intracavity intensity in SDLs becomes sufficiently high to achieve high output power with low threshold and low output coupling for the Raman laser.

SDLs have been investigated as pump sources for Raman lasers relatively recently. The first demonstration of an SDL-pumped Raman laser was reported in 2011 by Parrotta et al. of the Institute of Photonics. They employed an InGaAs-based SDL engineered for fundamental emission at 1040 nm to intracavity pump a pure $KGd(WO_4)_2$ crystal (KGW) and achieve a tuneable Raman laser from 1133 to 1157 nm with 0.8 W maximum output power [35]. Later, the same group demonstrated, in a similar Raman laser system, greater efficiency using a synthetic diamond [79], capable of emitting >4W of output power at longer wavelengths, from 1208 to 1256 nm, thanks to its greater Stokes shift and higher Raman gain when compared to the KGW case.

One of the main challenges in Raman lasers that often limits the output power is thermal lensing. Due to the inelastic nature of Raman scattering, the thermal power deposited in the crystal is directly linked to the Stokes output power generated during Raman laser operation and the associated thermal lens hinders the laser efficiency in turn [34]. Among all crystalline Raman materials, diamond is the least susceptible to thermal lensing thanks to its unmatched thermal conductivity of $\sim$2000 $Wm^{-1}K^{-1}$ [136], whereas most common Raman materials fall below $\sim$200 $Wm^{-1}K^{-1}$ [137], for which thermal effects are more significant. Unlike the CW regime, a pulsed pump source reduces this limitation if the pump photon lifetime is shorter than the thermal build-up time constant, which is typically on the order of 10 ms [34]. When implementing a

thin-disk solid-state laser for intracavity pumping the Raman medium, thermal lensing impacts on both materials with opposite sign and the achievement of a stable cavity in CW at high power can be very challenging [138]. In SDLs, on the other hand, thermal lensing is exiguous and hence negligible [139, 140].

As a parametric process, the Raman laser threshold depends mostly upon the pump intensity and it can be virtually extended to any desired wavelength (at a fixed Stokes shift) when the Raman laser becomes sufficiently intense to reach the threshold at the next Stokes wavelength. This is referred to as a cascaded Raman process. In general, for the continuous-wave case, the realization of high-quality broadband optics is often the decisive technological factor for the realization of a cascaded Raman laser. The first report of a CW cascaded Raman laser was indeed published in 2010 by Lee et al., using a neodymium-doped vanadate crystal with broadband antireflection coating (R$<$ 0.2%) extended to the second-Stokes wavelength [135]. In SDLs, the first demonstration of the Raman cascaded process was observed in the very first SDL-pumped Raman laser ([35], due to the presence of a small Stokes shift in the particular orientation of the crystal (KGW). In the last twenty years, the development of SDLs towards the challenging 1.3-1.7 μm region has been of interest for a number of remote gas sensing and medical imaging applications as discussed in Section 1.5. SDLs are very flexible devices that can incorporate Raman materials to reach relevant wavelengths and maintain their properties for that particular application.

In this chapter, we describe the theory of spontaneous and stimulated Raman scattering, following Chapter 3 of Demtröder's book *Laser Spectroscopy* [141]; review most gain materials so far exploited, with particular emphasis on diamond and KGW; illustrate some cavity designs and outline the main challenges that were previously mentioned above, such as spectral broadening and thermal effects.

3.2 Spontaneous Raman scattering

Raman scattering is an inelastic scattering of incident photons in a Raman-active material. To conserve the total energy, this phenomenon must be expressed by the following

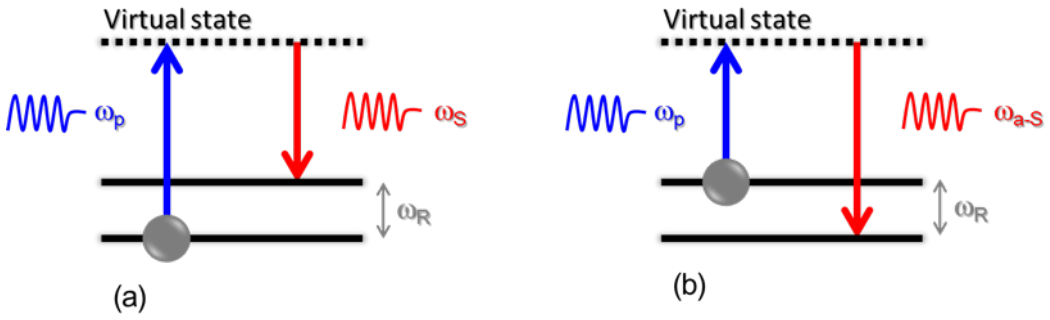

Figure 3.1: Scheme of Stokes (a) and anti-Stokes (b) Raman scattering. ω_p,ω_S,$\omega_{(a-S)}$, are the frequency of the pump (fundamental), Stokes-shifted, and anti-Stokes-shifted photon respectively; ω_R is the Raman shift frequency.

expression:

$$h\nu_p + E_i = E_f + h\nu_f \tag{3.1}$$

where $h\nu_p$ is the energy of the incident (or pump) photon, $h\nu_f$ is the energy of the scattered photon, and E_i and E_f are, respectively, the initial and final energy of the interacting Raman-active medium. The Raman shift $h\nu_R = E_i - E_f$ can be the result of a change in electronic, vibrational or rotational energy of the molecule. In particular, if a photon $h\nu_p$ interacts with a Raman-active molecule which has initial energy E_i and it is scattered with the same energy, the effect is called Rayleigh scattering or the resonant Raman effect ($E_i = E_f$). If the energy of the scattered photon is less (or more) than the incoming photon energy, the energy shift is called Stokes (or anti-Stokes). A diagram of Raman scattering is depicted in Fig. 3.1. At thermal equilibrium, the population level of the excited vibrational states is lower than at the ground state, thus the anti-Stokes effect is less likely than Stokes emission. A semi-classical theory is still sufficient to describe the Raman scattering process. Raman scattering is one amongst several nonlinear effects in a material when it is subject to high-intensity fields. When the intensity of the incident photons is high enough, the nonlinear terms in the induced macroscopic polarization, P, in the medium are not negligible any longer and it can be expressed as

$$P = \varepsilon_0 \left(\chi^{(1)} |\mathbf{E}| + \chi^{(2)} |\mathbf{E}|^2 + \chi^{(3)} |\mathbf{E}|^3 + \cdots \right) \tag{3.2}$$

where χ and ε_0 are, respectively, the optical susceptibility tensor and the permittivity of free space; and

$$\mathbf{E}(z,t) = \mathbf{E}_f e^{-i(\omega_f t - k_f z)} + c.c. \tag{3.3}$$

is the electrical field vector of the incident radiation, where the subscript f denotes 'fundamental' for consistency with the terminology used in this manuscript; $\mathbf{E}_f$ is therefore the field amplitude.

When subject to weak fields, the medium response is linear to the field amplitude and describes some well-known linear optical properties such as refraction, birefringence, dispersion and absorption. For high-intensity fundamental fields, the nonlinear terms become dominant. Nonlinear terms involve, in particular, multi-wave mixing of elastic and inelastic processes, such as second harmonic generation by the $\chi^{(2)}$ term, Raman scattering (either spontaneous or stimulated) and stimulated Brillouin scattering by $\chi^{(3)}$ [19]. However, since we are focusing on the inelastic process of Raman scattering, the $\chi^{(3)}$ becomes more dominant over $\chi^{(2)}$ in crystals that feature inversion symmetry, for which $\chi^{(2)}$ is zero. This can be displayed conceptually, in scalar approximation, by considering the external high-intensity field interacting with the vibrational modes of the crystal, i.e. phonons, causing the atoms of the lattice to vibrate against each other, inducing a macroscopic polarization $P_{NL} = \chi^{(3)} |\mathbf{E}|^3$ that sets the Raman shift as indicated in Fig. 3.1. Raman transitions from the ground to the excited level take place when the derivative of the polarizability, α, of the crystal cell with respect to the normal coordinate, q, does not vanish, i.e $\partial\alpha/\partial q \neq 0$, and this occur for those class of crystals that posses a centre of inversion [19].

3.3 Stimulated Raman scattering

A Raman laser is based on the stimulated Raman scattering effect: when the field of the Stokes (or anti-Stokes) radiation produced by the phonon relaxation stimulates another molecule in its virtual state, this generates stimulated Raman scattering. Even in a solid material, the event probability for Raman scattering is around 10^{-6} of the incident radiation intensity through 1 cm. Under high-intensity radiation, SRS can

be 10% the incidence intensity [19]. In practice, ∼MW/cm^2 of intensity is needed to reach the threshold. A schematic illustration of the SRS process is depicted in Fig. 3.2. During SRS the external field of Eq. 3.3 is the contribution of both the fundamental and the Stokes field, which becomes

$$\mathbf{E}(z,t) = \mathbf{E}_f e^{-i(\omega_f t - k_f z)} + \mathbf{E}_S e^{-i(\omega_S t - k_S z)} + c.c. \tag{3.4}$$

where ω_f,ω_R are the fundamental and the Raman frequency respectively. A simplified formulation of the SRS gain can be given by classical theory. The third-order nonlinear term of the induced macroscopic polarization, $\chi^{(3)}$, includes a negative imaginary part due to damping term, γ, of the harmonic oscillator, which is subject to the external force of Eq. 3.4. Under high-intensity fields, the radiation wavevector propagating in the medium experiences exponential growth, i.e. gain, as the Raman susceptibility $\chi^{(3)}$ is always negative. It can be demonstrated that the gain becomes [19]

$$g(\omega_S) = \frac{\omega_S}{n_S^2 c}\frac{\varepsilon_0 N}{m}\left(\frac{\partial\alpha}{\partial q}\right)_0^2 \frac{2\gamma(\omega_f - \omega_S)}{\left[\omega_R^2 - (\omega_f - \omega_S)^2\right]^2 + 4\gamma^2(\omega_f - \omega_S)^2} \tag{3.5}$$

where $_s$ is the refractive index at the Stokes wavelength. At the resonance frequency $\omega_S = \omega_f - \omega_R$

$$g(\omega_S) = \frac{N}{n_S^2 m c^2}\left(\frac{\partial\alpha}{\partial q}\right)_0^2 \frac{\omega_S}{2\gamma\omega_R}, \tag{3.6}$$

which can be approximated to $g(\omega_S) \sim \lambda_S^{-1}$. The linear dependence between gain and Stokes frequencies has been verified experimentally, e.g. in hydrogen gas [142] and diamond [143]. A few considerations: $\partial\alpha/\partial q$ is wavelength-independent for those materials where the electronic transition frequencies are much higher the fundamental field frequency [144]; the gain linewidth, 2γ, is the reciprocal of the dephasing time, within which the vibrational states are in phase (typically ∼10 ps for most crystalline Raman media) and is generally a temperature-dependent factor. Note that the monochromatic expression of the gain of Eq. 3.6 applies for continuous-wave operation, or the steady-state regime, in which the duration of the fundamental/Stokes pulse is much longer

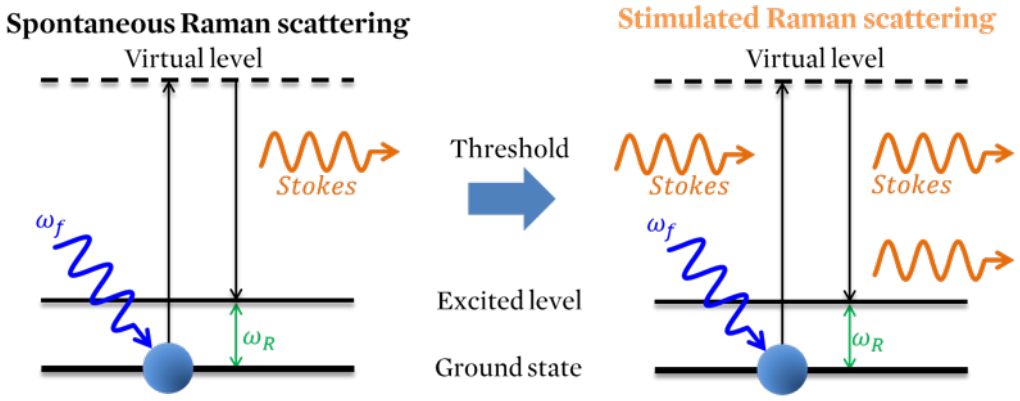

Figure 3.2: Diagram of the stimulated Raman scattering phenomenon.

than the dephasing time. The steady-state regime is relevant for the work reported in this thesis, which is all CW, and is all that will be considered here.

The classic model of SRS gain is rather generic as it does not take into account the occupation number of the quantum states at the ground and upper level in the stationary case, and the polarization vectors do not emerge. For quantum-mechanical calculation of the gain, the rate equation of the Stokes phonons during SRS is proportional to the expectation value of the interaction Hamiltonian between the Stokes and fundamental fields, and the population density at the initial and final states [144]. This is Fermi golden rule. The rate equation for the Stokes photons is hence [144]

$$\frac{dN}{dt} = \left(\frac{\partial\alpha}{\partial q}\right)_0^2 \left(\frac{4\pi^2}{n_p n_S mc}\right) I_f \sum_{k_S} \frac{\omega_S}{\omega_R} \mathbf{e}_f \cdot \mathbf{e}_S [1 + N_S + N_V] \Gamma(\omega_S - \omega_f + \omega_R), \quad (3.7)$$

where n_p and n_s are the refractive indices at the fundamental and Stokes wavelengths, N_s and N_v are the Stokes and phonon populations, Γ is the spectral profile of the Raman transition that assumes a Lorentzian shape when homogeneously broadened, and $\mathbf{e}_f \cdot \mathbf{e}_S$ is the scalar product between the fundamental and the Stokes field vector orientation, which is maximized for parallel field propagation when $\partial\alpha/\partial q$ is scalar. In reality $\partial\alpha/\partial q$ is a tensor, which can have off-diagonal terms and the polarization can be thereby determined [34], through which the steady-state gain can be represented as

follows

$$g(\omega_S) = \left(\frac{4\pi^2}{n_p n_S mc}\right) \frac{\omega_S}{\omega_R} \sum_i |\mathbf{e}_S R_i \mathbf{e}_f|^2 \tag{3.8}$$

Where R_i is the Raman tensor include the $\partial\alpha/\partial q$ terms [137] in an off-diagonal 3×3 matrix, which describes the strength of the interaction at each Raman oscillation mode $i = 1, 2, 3$. In diamond, for example, maximum gain is obtained when the fundamental and the Stokes field are both linearly polarized and aligned with the <111> axis, which corresponds to the vibration of the carbon-carbon bond in the lattice. Imperfections of the crystal structure induce the fields to rotate and hence diminish the Raman gain.

3.3.1 The effective Raman gain

The general formulation of the Raman gain so far outlined is appropriate for a monochromatic fundamental spectrum. In the case when the fundamental spectrum is broader than the Raman gain bandwidth, the Raman gain can be reduced and the so called effective Raman gain must be considered [145].

When Raman laser photons are produced, their spectral similarity to the fundamental spectrum shape depends on the degree of correlation between their respective fields. However, due to some instrument limitations, the intensity fluctuations may be too fast to be captured by a nanosecond-response detector such that it becomes more convenient to measure directly the spectral intensity curve in order to determine to what extent correlation occurs and how much this inhibits the performance [146]. In this sense, provided that the gain coefficient is defined by the growth term of the rate equation of the Stokes field as

$$\frac{\partial \bar{I}_S}{\partial z} = g_{eff} \bar{I}_S \bar{I}_S \tag{3.9}$$

the time-phase fluctuations that are embedded in the general expression of the laser intensity can be instead included in the effective Raman gain, g_{eff}, that is

$$g_{eff} = \varepsilon g_0 \tag{3.10}$$

where ε is the reduction factor (dimensionless), and g_0 the monochromatic Raman gain

coefficient. The laser intensity $I(z,t)$ in Eq. 3.9 is averaged over the time fluctuation t. By this, regardless of the dynamic behaviour due to intensity and phase noise fluctuations, which are often nontrivial to measure, the laser properties become thus directly attributed to the effective Raman gain. It can be demonstrated [146, 147] that the gain reduction factor is defined by

$$\varepsilon = \frac{\left|\sum_j F_i S_j^*\right|^2}{\sum_j |F_j|^2 \sum_j |S_j|^2} \tag{3.11}$$

where the subscript j refers to the longitudinal mode number of the fundamental or Stokes field, indicated by F and S respectively. According to the Schwarzs identity, it turns out that $0 \leq \varepsilon \leq 1$. Amplitude and phase noise is represented by the phonon field term $F_j S_j^* \propto e^{i\phi_f - i\phi_S}$, which is fixed if the pump and the Stokes are correlated, while it fluctuates if correlation does not occur and the phase noise changes over the dephasing time of the phonon field. So far it has been assumed that the fundamental laser field is very broad compared to the Raman linewidth, that is $\Delta\omega_f \gg \Delta\omega_R$, and the separation between two consecutive fundamental modes is much greater than $\Delta\omega_R$ [146]. In the time-domain, $\Delta\omega_f \gg \Delta\omega_R$ means that fundamental longitudinal modes fluctuate much quicker than the dephasing time of the phonon.

If the correlation is established, the fundamental photons correspond coherently to the Stokes photons and both spectra are identical such that $\Delta\omega_f = \Delta\omega_S$. In this case, the phonon field reaches steady-state and monochromatic gain is achieved, thus $\varepsilon = 1$. For poor correlation, instead, the phonon field phase varies randomly that the effective Raman gain is diminished, and hence $\varepsilon \leq 1$.

What drives the two fields to be correlated is the degree of dispersion in crystals, which accounts for the difference of the group velocity between pump and Stokes photons. For no dispersion, the fundamental and Stokes fields are correlated. When dispersion occurs, the dispersion prevents the synchronization between the two fields and correlation is not established any longer. To determine whether the fields are

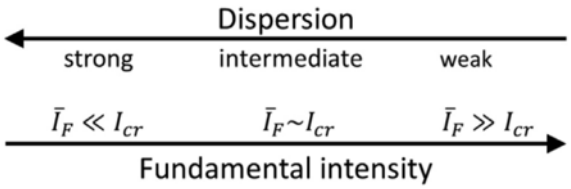

Figure 3.3: Diagram of the dispersion level. Image taken from [146].

correlated or not, a critical intensity can be defined [146]

$$I_{crit} = \frac{\Delta\omega_f |\mu_\pm|}{g_0} \tag{3.12}$$

where $\mu_\pm$ is the difference of group velocity and $\Delta\omega_f$ is the FWHM of the fundamental spectrum. In the ideal case of monochromatic radiation, $I_{crit} = 0$, dispersion is absent and the fields are fully correlated. However, dispersion can be considered zero or negligible also when the fundamental intensity is $I_f \gg I_{crit}$. In this case, the dispersion is weak and correlation is held, inhibiting effective gain reduction. Conversely, the system is under the highly-dispersive regime for relatively weak fundamental fields, and hence correlation is lost and the effective Raman gain consequently becomes reduced. An intermediate situation can be created when $I_f \sim I_{crit}$, in which the lasers are partially driven into correlation. The diagram in Fig. 2.3 summarises these three scenarios [146]. The case of a very broadband laser field is applicable to gaseous Raman media, whose Raman gain linewidth is very narrow owing to the typical narrow feature of the single-molecule Raman transition in gas.

It is a different case for many crystalline Raman gain media. In these systems, dispersion is of particular relevance since gain suppression diverts the Raman laser from its maximum performance. As a result, the two spectral fields have different width, from which the gain reduction factor can be analytically estimated to be [146]:

$$\varepsilon = \int [f(\omega) * R(\omega - \omega_R)] S(\omega) \mathrm{d}\omega \tag{3.13}$$

Where $f(\omega) * R(\omega - \omega_R R)$ is the convolution between the Raman lineshape (amplitude normalised to the unit) and the fundamental spectrum; ω_R is the Raman shifted fre-

quency. Both $f(\omega)$ and $S(\omega)$, the Stokes spectrum, are normalized to the area. Full mathematical derivation of Eq. 3.13 can be found in Eq. (3.29-3.30) of ref. [146]. For the special case in which all curves can be approximately considered Lorentzian-like, the reduction factor is simplified to

$$\varepsilon = \frac{\Delta\omega_R}{\Delta\omega_R + \Delta\omega_f + \Delta\omega_S} \tag{3.14}$$

Continuous-wave intracavity Raman lasers mostly operate in the high-dispersion regime owing to the relatively high critical intensity [145, 146], causing the laser to broaden and diminish the effective Raman gain. Spectral control of the fundamental in order to achieve $\Delta\omega_f \ll \Delta\omega_R$ is therefore advantageous in maximising the laser performance.

3.3.2 Phase-matchless SRS and intracavity Raman beam clean-up

The Raman beam clean-up effect [148] is Raman laser oscillation towards TEM_{00} from a multimode intracavity pump beam in an intracavity set-up (see Section 1.4.3). This can be explained by a few theoretical considerations [148]. Raman Stokes amplification is a four-wave mixing process in which the phase-matching condition is automatically satisfied, which is true for monochromatic radiation and forward propagation for which the relative phase field between the fundamental and Stokes is actually cancelled. When the amplitude of the fundamental field is oscillating with either the k_{f1} or k_{f2} wavevector, that is [148, 149]

$$E_f = E_{f1}\delta(\mathbf{k} - \mathbf{k}_{f1}) + E_{f2}\delta(\mathbf{k} - \mathbf{k}_{f2}) \tag{3.15}$$

and, for simplicity,

$$E_S = E_S\delta(\mathbf{k} - \mathbf{k}_S) \tag{3.16}$$

the polarization amplitude $P_S^{NL} = \chi_R^{(3)}|\mathbf{E}|_f^2 E_S$ becomes

$$\begin{aligned} P_S^{NL} = \chi_R^{(3)}[|\mathbf{E}_{f1}|^2 E_{S1} + |\mathbf{E}_{f2}|^2 E_{S1}]e^{i\mathbf{k}_S\cdot\mathbf{z}} + \\ + E_{f1}E_{f2}^* E_S e^{i(\mathbf{k}_{f1}-\mathbf{k}_{f2}+\mathbf{k}_S)\cdot\mathbf{z}} + E_{f1}E_{f2}^* E_S e^{i(\mathbf{k}_{f1}-\mathbf{k}_{f2}+\mathbf{k}_S)\cdot\mathbf{z}} \end{aligned} \tag{3.17}$$

The first two terms are phase-cancelled and the relative polarization amplitude propagates periodically in the medium with the phase term $\exp(-i\mathbf{k}_S \cdot \mathbf{z})$, called 'primary Stokes components' [148], and they replicate the fundamental field intensity distribution. On the other hand, the 'secondary Stokes components' [148] are not collinear with the fundamental field as the secondary photons field direction follows the probability distribution governed by the phase-matching condition, filling the void in the aberrated fundamental field intensity generated by Stokes-converted beam and hence leading to a Raman laser output beam with higher brightness. Thus, Raman lasers are also efficient brightness converters.

3.4 Raman cavity arrangements

Raman lasers can be generated with quite diverse configurations, among which are: the single-pass resonator for the pulsed regime; extracavity and intracavity for quasi- or continuous wave operation; and the self-Raman laser. Depending on the design, Raman media can also be considered along with frequency-doubling crystals to enable laser operation in a more difficult spectral region. What makes $\chi^{(3)}$ nonlinear materials attractive for frequency conversion is the phase-matchless nature of SRS. Indeed, unlike second-order nonlinearities of standard optical parametric oscillators (OPOs), in which different techniques are required to achieved phase-matching, SRS design is more straightforward and robust as phase-matching is automatically satisfied. The consequent Raman beam clean-up is also advantageous in designing a stable cavity as it partially compensates thermal defocusing to which most Raman bulk media are prone. With the exception of glass fibre Raman lasers, SRS it is not directly tuneable due to the natural narrow Raman gain lineshape of crystalline materials. When the pump source has a broad gain bandwidth, the cavity can therefore be tailored for fundamental wavelength tuning, typically with an intracavity birefringent filter, allowing to tune the fundamental and, in turn, its Stokes-shifted wavelength. Raman media are well adaptable to a wide range of most mature laser media as well as easily applicable to the SDL technology in a variety of designs which will now be discussed.

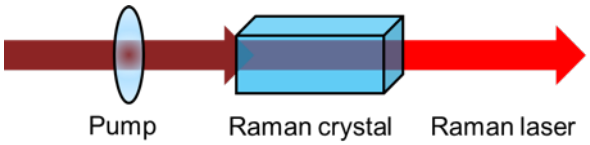

Figure 3.4: Single-pass Raman generator diagram.

3.4.1 Raman generator

The first SRS was produced in a so-called Raman generator as previously introduced in the introduction section of this chapter. With this design, a train of single pulses is focused tightly into the medium which amplifies the spontaneous scattered Stokes radiation in the same direction. Though a Raman generator is cavity-free, sometimes a mirror can be placed to reflect the pump light back to the Raman medium and achieve higher power. Schematic representation of a Raman generator is illustrated in Fig. 3.4. SRS is reached above a certain critical intensity of around 100 MWcm^{-2} or even above for typical crystalline Raman gain media. Typically, at this order of magnitude, the media can be subject to a severe thermal stress, which incurs self-focusing and optical damage. Most Raman generators, such as tungstate, nitrate, and molybdate are pumped by nano and picosecond laser sources in the green and 1μm region. High-intensity peaks also produce multiple Stokes and anti-Stokes photons in cascade towards undesired wavelengths, which may be difficult to select in a cavity-free design. Due to the high-intensity threshold, Raman generators are still good converters of pulsed laser sources [150].

3.4.2 Extracavity Raman laser

When a Raman medium is placed in a high-finesse cavity separated from the pump light, appropriate HR/AR mirror coatings can be designed for output-coupling at a specific Stokes wavelength. In comparison to the Raman generator, the Stokes wavelength resonates in the cavity. The customisation of the coatings therefore inhibits the stimulated emission of parasitic wavelengths. In this cavity configuration, the Raman material is pumped by the output of an external pulsed or (quasi-)cw laser source and is schematized in Fig. 3.5. The Raman laser threshold is attained when the round-trip

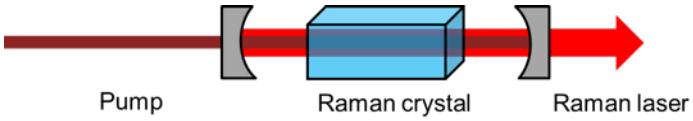

Figure 3.5: External cavity Raman laser diagram.

gain balances out the round-trip loss. Considering a l_c-long Raman material with gain g_R, aligned between two lossless mirrors having reflectivity R_1 and R_2, the equation that governs pump intensity threshold I_{th} and gain is [134]

$$R_1 R_2 \exp(4 g_R l_c I_{th}) = 1, \tag{3.18}$$

where the factor 4 is associated with the backward and forward SRS in a round-trip. Whereas R_1, R_2 and l_c are fixed parameters of the cavity, g_R I_{th} depends on the spatial overlap between the pump size and the Raman cavity mode across the crystal [145]. For a Raman gain of 5 cm/GW the intensity of the incident pump must be around 10 MW/cm^2. This level of intensity is difficult to achieve with a CW pump source and the literature records only few cases. For instance, the first CW Raman laser was demonstrated to function in an external-cavity geometry for the first time (2004) by Grabtchikov et al. [132]. In that experiment, a $Ba(NO_3)_2$ crystal was pumped by a multimode CW Ar^+ laser to reach a maximum output power of around 164 mW with 5.5 W of incident pump power. Later, most high-efficiency external-cavity Raman lasers were employed in Q-switched operation using solid-state lasers for conversion to the eye-safe region and intracavity frequency conversion to the visible and ultraviolet [151]. Nevertheless, demonstrations of extracavity quasi-CW Raman lasers were reported very recently. In quasi-CW operation the Raman laser reaches the steady-state regime and at the same time the thermal effects remain too weak to be detrimental to the output power. Within this limit, Kitzler et al. reported an analytical model to describe the operation of a diamond Raman laser with 23-W of output power at 1240-nm [152]. Later, Williams et al. expanded the model of a similar system to the second Stokes wavelength in diamond at 1.5 μm with 114 W average output power [37]. Through active cavity stabilisation of an external-pumped diamond Raman laser, single-frequency operation

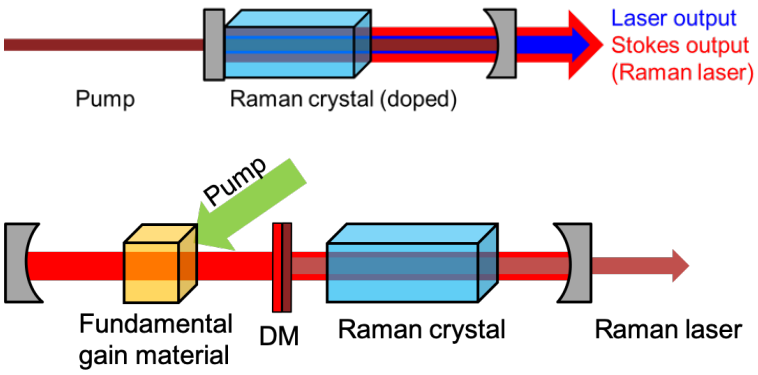

Figure 3.6: Illustration of intracavity Raman lasers in (*top*) self-Raman and (*bottom*) coupled-cavity arrangements. DM: dichroic mirror.

at 1486 nm was demonstrated for water vapour detection [153]. Multi-Watt operation is therefore attainable with long pulses. When the pump source approaches 100% duty cycle (i.e. CW), the Raman laser becomes significantly susceptible to thermal lensing at high power impeding the laser from power scaling [154].

3.4.3 Intracavity Raman laser

In an intracavity Raman laser system the fundamental gain material is aligned within the same cavity as the Raman crystal. In this geometry, the fundamental gain is pumped by an external source (typically a laser diode) and the Raman wavelength generated resonates in the same cavity to allow high intracavity power and thus low threshold. Mirrors must be coated for minimum leakage at the fundamental wavelength and partially-reflective at the Stokes-shifted wavelengths for high-power output coupling. Two main cavity configurations are possible: self-Raman laser and coupled-cavity Raman laser. Schematization of such systems are depicted in Fig. 3.6. For wavelength emission towards shorter wavelengths the Raman cavity can also be extended to accommodate a $\chi^{(2)}$ material for either second harmonic or sum frequency generation. In a self-Raman laser, the fundamental and the Raman laser are emitted from the same material source. Typically, in a Raman-active crystal optical absorption is forbidden for the reason previously explained in Section 1.2. When it is doped, the impurities can be optically pumped and the subsequent laser emission can feed the

medium for self-Raman laser action.

In a coupled-cavity geometry, the fundamental gain medium is separated from the Raman crystal by a dichroic mirror, which is highly-transparent at the fundamental wavelengths on one side to allow beam penetration in the Raman material, and highly-reflective at the Stokes-shifted wavelengths for Raman laser.

Unlike external-cavity Raman lasers, fundamental and Raman laser behaviour depend upon each other when they resonate within, or at least partially, the same cavity. By having two partially shared cavities the spectral control of the sole fundamental via the insertion of optical filters automatically dictates in turn the spectral behaviour of the Raman laser. In CW operation, small cavity mode radii are essential for low threshold. In a self-Raman laser a low threshold can be achieved by side-pumping. The large availability of high-power laser diodes in the 800 nm range helps in achieving population inversion of Nd^{3+} levels in most Raman materials. When the Raman material is undoped, the cavity parameters should be arranged for minimum focusing.

The first intracavity Raman laser demonstrated was a diode-pumped self-Raman laser from a Nd-doped KGW crystal with 56 mW maximum output power at 1181 nm [133]. In the same year, 2005, a Nd:YAG/KGW system was developed for higher power (0.8W) at the same wavelength [134]. Later, several intracavity systems have been demonstrated at the Watt-level in CW. The record of output power of 6.1 W has been reported twice from the first Stokes wavelength of a KGW crystal. In the first system the KGW was included in a Nd:YLF laser cavity for Stokes generation at 1139 nm with a relatively poor beam quality [155]. In the same experiment the fundamental cavity was slightly adjusted to accommodate a diamond Raman crystal, which offered less power at 1217 nm (5.1 W maximum) but the beam quality was improved to the diffraction-limit. In our experiment presented in Chapter 5, a maximum output power of 6.1 W was reached at 1320 nm from the first Stokes shift of an InGaAs SDL with greater conversion efficiency (∼6% against 4% in the solid-state case), with a possible strong limitation due to thermal lensing generated at higher power.

Bonner et al. investigated and measured the thermal lensing in an intracavity Raman laser [138]. In the case of a Nd:YVO_4 gain disk, both the fundamental and the

Raman beams are subject to opposite focal length sign [138]. In the particular case of a compact SDL-pumped system, thermal lensing is negligible at high diode pump power [7]. When the diamond is implemented for Raman conversion, its highest thermal conductivity makes the SDL-pumped diamond Raman laser a solid setup to avoid thermal lensing distortions. Parrotta et al. demonstrated multi-Watt output power operation at 1228 nm with such a system [89]. In this work, the cavity was optimized at high pump power for minimum thermal focusing distortion due to intracavity optics, such as the birefringent filter and dichroic mirror. This enabled maximum linear differential efficiency of 23% reaching a maximum output power of 4.4 W with high spatial and spectral beam quality [89].

CW intracavity Raman lasers are therefore a very compact and efficient solution to reach long wavelength. The complex interplay between the fundamental and the Stokes beams has attracted attention in developing models to explore the potential of such systems. Spence et al. studied the characteristics of CW intracavity Raman lasers to determine the performance of the output power, considering second harmonic generation [156] and spatial and spectral effects between the fundamental and the Stokes field [145, 146].

In the next section Spence model of a CW intracavity Raman laser will be presented.

3.5 Spence model

D. Spence described in 2007 the behaviour of a CW intracavity-doubled Raman laser system, providing some numerical calculations and comparison with previous experimental work [156]. In that model, the fundamental and the Stokes-shifted beam spectral profiles were considered monochromatic. The two beams propagate uniformly in the transversal cross-section such that the overlap between the fundamental and the Stokes beams is perfect. Based on that and on the work of P. A. Apanasevich (such as ref. [157]), in 2013 Spence adjusted the theoretical model by implementing the actual behaviour of the transverse and longitudinal propagation of both beams inside the crystal. When the spectral linewidth is also taken into account with respect to the natural

Raman lineshape, the Raman gain turns out to be affected as well. Both spatial and spectral dependences are therefore explicitly evaluated in the latest model.

Following these considerations, the rate equations of a solid-state-pumped intracavity Raman laser are [145]:

$$\frac{dn}{dt} = \frac{P_p}{hc/\lambda_p} - \frac{2\sigma}{A_L hc/\lambda_f} n P_f - \frac{n}{\tau} \tag{3.19a}$$

$$\frac{dP_f}{dt} = -\frac{2c}{l\lambda_f/\lambda_S}\frac{l_c g_e}{A_e} P_s P_f + \frac{c\sigma}{lA_L} n P_f - \frac{c}{2l} L_f P_f \tag{3.19b}$$

$$\frac{dP_S}{dt} = -\frac{2c}{l}\frac{l_c g_e}{A_e} P_f P_S + \frac{c}{2l}(L_S + T_{OC}) \tag{3.19c}$$

where λ_f,λ_S,λ_p are the wavelengths of the fundamental, Stokes and the laser diode pump; n, σ, τ, A_L are properties of the fundamental solid-state gain medium and indicate, respectively, the population density of the inverted ions, the gain cross-section, the lifetime of the inverted ions at the upper level, and the effective area; P_p, P_f, P_S are the diode pump power, the intracavity fundamental and Stokes power respectively; L_f, L_S are the internal losses due to optical absorption and Fresnel reflection at the fundamental and Stokes wavelengths respectively; l, l_c are the optical cavity and the crystal length respectively; T_{OC} is the output coupler transmission at the Raman wavelength. Finally, g_e, A_e are the effective Raman gain and the spatial overlap between the fundamental and the Stokes laser intensities along the crystal. While the effective Raman gain is $g_e = \int [f(\omega) * R(\omega)] S(\omega) d\omega$, the effective pumped area A_e is [145]

$$A_e = \left(\int \bar{I}_f \bar{I}_S dA \right)^{-1}, \tag{3.20}$$

with $\bar{I}_f$ and $\bar{I}_S$ the area-normalized beam intensity of the fundamental and Stokes lasers, integrated across the beam transverse area A throughout the entire crystal length. Longitudinal and transverse modes can vary with pump power.

Equations 3.19 have a positive term due to the diode and fundamental pump power, a negative factor related to the spontaneous scattering loss, round-trip loss due to absorption and transmission loss. Also, being co-resonant, the fundamental beam is automatically subject to deterioration above the Raman threshold, as the Raman con-

version process is actually a loss for the fundamental. The loss term associated with it is therefore proportional to the Stokes power.

Considering the spontaneous scattering rate negligible, at the steady state, all equations in 3.19 must be zero, which returns the value of diode pump power required to reach the Raman laser threshold

$$P_{th} = \frac{(T_{OC} + L_S)L_f}{4l_c}\frac{\lambda_f}{\lambda_S}\frac{A_e^{th}}{g_e^{th}} \tag{3.21}$$

and the output power of the Stokes laser

$$P_S = \frac{T_{OC}}{T_{OC} + L_S}\frac{\lambda_p}{\lambda_S}P_p - \frac{T_{OC}L_f}{4l_c}\frac{\lambda_f}{\lambda_S}\frac{A_e}{g_e} \tag{3.22}$$

where the A_e^{th}/g_e^{th} factor is valued at the threshold. Ideally, once the Raman threshold has been reached, the Stokes output power will increase linearly with maximum slope efficiency given by

$$\eta_{eff} = \frac{T_{OC}}{T_{OC} + L_S}\frac{\lambda_f}{\lambda_S} \tag{3.23}$$

and the fundamental intracavity power, P_f, becomes independent of the pump power, i.e. it clamps at the Raman threshold value

$$P_f = \frac{L_f A_e}{4l_c g_e} \tag{3.24}$$

However, A_e/g_e is likely a complex function of the pump power due to, for instance, competing modes reaching threshold. When this is the case, the fundamental intracavity power increases and the Raman gain extraction efficiency is hence reduced. There are a few other factors that are to the detriment of the Raman laser efficiency, such as thermal focusing of intracavity optics and pump power dependency of the laser emission wavelength. For the specific case of a SDL-pumped Raman laser, the internal conversion efficiency factor of the SDL itself, η_{SDL}, which counts the relative number of pump photons converted to SDL photons, can be added as a multiplication term to Eq. 3.23. Variation of η_{SDL} caused by thermal rollover, pump efficiency, etc. will also influence the performance of the Raman laser.

This model gives an approximate prediction of the intracavity Raman laser behaviour when the laser parameters have been determined independently. Besides the model, the Raman laser efficiency can be optimised by choosing a crystal that minimises optical absorption and maximises the $\sim g_R l_c$ factor. Low threshold is achieved when the mean size of the fundamental cavity mode is minimised in the Raman crystal. Tight focusing nevertheless enhances thermal lensing when high Stokes output power is also achieved.

In an ideal intracavity Raman laser as schematized in Fig. 3.6, while the external pump increases, the fundamental gain increases as well up to the point in which the gain is equal to the round-trip losses and the pump power reaches the threshold at the fundamental wavelength. Now that the fundamental laser emission is established, the fundamental gain is clamped and the fields resonate within the Raman cavity. While the pump power further increases, the fundamental intensity increases as well, and the Raman gain becomes proportional to the intracavity fundamental fields intensity. While the fundamental intensity is growing as the pump power increases, the Raman gain at the Raman wavelength becomes high enough to balance out the round-trip losses and the Stokes field will resonate too. At the Raman threshold, the Raman gain is clamped equal to the Raman cavity round-trip losses, and the fundamental intracavity intensity must be clamped to maintain steady state. However, as the fundamental and Stokes fields oscillate within the same cavity, the fundamental laser necessarily experience loss due to Raman conversion. The loss is proportional to the Stokes intensity and thus the fundamental gain increases to be equal to the round-trip loss.

The literature has only a few experimental works in which the Raman gain extraction efficiency is close to ideal. For instance, Parrotta et al. reported the case of the intracavity diamond Raman laser pumped by a SDL (see Fig. 3 of Ref. [89]). To achieve high power at the Raman wavelength of 1227 nm, the system was optimized at high pump power. In this region, the fundamental intracavity power of the SDL was clamped and the Raman laser differential efficiency was 23%, against the predicted slope efficiency of 31%, using $T_S = 2.2\%$, $L_S = 0.8\%$, $\lambda_p = 808$ nm of Eq. 3.23 multiplied by $\eta_{SDL} = 65\%$. Below this region, the Raman laser behaviour became more

complex, suggesting that the evolution of the spatial and spectral mode overlap between the fundamental and the Stokes beams within the medium were detrimental to the ideal slope efficiency [89]. This trend is most typical in those Raman lasers that have exploited SDL technology. With the exception of diamond, thermal lensing is more prominent in the Raman material than in the SDL chip such that the maximum conversion efficiency can be achieved via cavity adjustment. Continuous-wave intracavity Raman lasers are generally so sensitive to the optical losses that in most cases the output power behaviour becomes more dependent, at least within a relatively limited range of pump power, on thermal effects and spectral/spatial beam fluctuation rather than the pump power itself. Nevertheless, this model illustrates and highlights the main optical parameters for an optimal design of an efficient Raman laser.

Spences model can be extended to an arbitrary number of Stokes modes in cascade, but although this work takes advantage of the cascaded Raman conversion to achieve novel wavelengths at 1.7 μm, a more general model of the CW intracavity-pumped cascaded Raman laser is therefore interesting for future investigations to predict the optimum conversion efficiency.

3.6 Raman materials

A variety of Raman media have been employed for SRS, such as gases, liquids and solids, including crystals and glass fibres. This thesis is focused primarily on crystalline Raman lasers but a general overview to the other forms is first given in this section. The inherent properties of gases benefit Raman lasers with large Stokes shift and low scattering loss. Hydrogen, deuterium and methane have been mostly exploited for wavelength conversion of high-power pulsed laser sources such as Nd:YAG. Gas Raman lasers offer large Stokes shift, typically 2 or 3 times higher than common crystalline media. However, they suffer from low gain and need to be implemented in bulky cells, which make them impractical for commercial application.

Liquid Raman materials have the disadvantage of absorption in the visible and infrared wavelengths. Being also quite toxic and volatile near room temperature, the

literature is limited to a few cases, such as liquid nitrogen at 77 K [158].

Glass fibres, on the other hand, are relatively compact and Raman laser operation relies on high-purity material over the long interaction length (up to a few hundred meters) in the fibre core, which compensates the low gain (<0.02 cm/GW). The most popular material is pure fused silica, which enables frequency conversion over its long transparency range (<2 μm) by multiple Stokes shifts of $\sim$440cm^{-1} in cascade. Nowadays, the fabrication of reliable long fibres is so well-established that Raman fibre lasers are available commercially for telecom purposes (1.3-1.5 μm). In contrast to gases and crystals, Raman fibre lasers are tuneable as the natural Raman gain spectrum of amorphous materials is characterized with a very broad feature, typically $\sim$200 cm^{-1} for fused silica [159]. However, in fibres SRS is generated by amplification in a non-resonant cavity. This precludes fibres from exploring shorter wavelengths with intracavity SHG.

Crystalline Raman lasers have been introduced for the first time in 1963 using a natural piece of diamond, calcite and a Ruby laser [128]. Since then, the availability of high-quality long synthetic crystals was rather limited and the first functioning Raman laser in pulsed operation with high efficiency (as high as 77%) was presented several years later, in 1977 [160]. In recent years, the establishment of the fabrication of high-purity single crystals spurred laser research and development towards crystalline SRS. Solid-state materials for Raman lasers include diamond tungstate-based crystals (e.g. $KGd(WO_4)_2$ in its pure and doped form) vanadate, iodate, nitrate and molybdate structures. Such crystals have good mechanical properties, which make them implementable with other solid-state laser sources. The Raman gain is between $\sim$1-20 cm/GW and they generally offer Raman shifts of $\sim$1000 cm^{-1}. Despite high gain, crystal length is also chosen to compensate optical absorption and birefringence loss when the medium is used for intracavity or extracavity configuration. The most relevant Raman gain materials for this thesis are synthetic diamond and pure KGW, to which are dedicated the two subsections below.

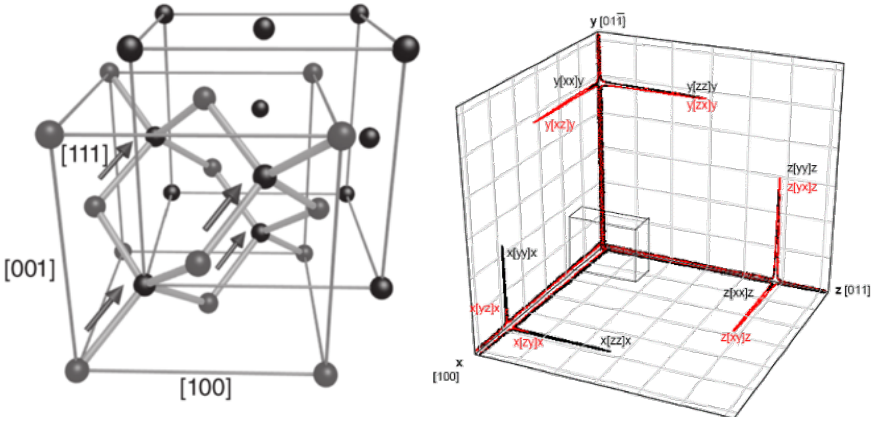

Figure 3.7: (Left) Diamond crystal structure representation in three dimensions. (Right) Spontaneous Raman spectra of diamond for different polarization directions. Image taken from Ref. [137]

3.6.1 Diamond

The crystal structure of the diamond unit cell consists of two interpenetrating face-centred cubic (fcc) lattices shifted by a/4 along the principal diagonal (<111> direction), where a is the unit cell parameter (see Fig. 3.7). The primitive cell is a tetrahedron with a carbon atom in the centre and with four covalent sp_4 bonds linked to the nearest atoms. The strong covalent bonds between such low-mass atoms are responsible for its high mechanical rigidity and highest thermal conductivity. Despite this, diamond can be contaminated by few similar elements of different groups, such as boron and nitrogen. When an impurity takes place, however, the point defect leaves a dangling bond responsible for optical absorption and stress, which causes in turn birefringence [161, 162].

Due to its high symmetry, diamond has threefold degenerate acoustic modes (F1u) and three degenerate optical vibration modes (F_{2g}). In particular, F_{2g} modes are given by the rigid oscillation of the two fcc cells, which are responsible for the single Raman shift of $\sim$1332 cm^{-1} and $\sim$1.5 cm^{-1} linewidth (FWHM), which both slightly vary by isotopic content and temperature shifts respectively [161].

Bulk diamond has large energy bandgap, allowing absorption at 230 nm and in the 5 μm region by two-phonon absorption. Natural diamond is classified type I or type II

[163] depending on the nitrogen content [164]. Imperfections in a single-crystal diamond can vary from sample to sample [165] that is disadvantageous for laser application. When diamond is synthetically grown, birefringence can still vary by one order of magnitude across the sample [162], which leads to a reasonable depolarization loss when inserted for intracavity Raman conversion.

For laser application, diamond should be chemically pure and single-crystal to minimise absorption and birefringence loss. Two processes are known to synthesise diamond: high-pressure high-temperature (HPHT) [166, 167] and chemical vapour deposition (CVD). HPHT synthesis recreates the thermodynamic condition under which natural diamond is formed. Typically, a carbon-rich melt undergoes a pressure of 5-6 GPa at around 1500°C. Depending on the conditions, small grains or single crystals of physical dimensions of some millimetres can be produced. In this case, diamond may have too many nitrogen impurities (up to 200 ppm [164]) for being used as an active medium in continuous wave. They are mostly exploited for cutting tool applications. In contrast, CVD growth on a diamond substrate forms a single crystal diamond up to 10x10 mm^2. In the CVD technique, a dilute concentration of methane gas in a low-pressure environment of hydrogen is the seed of the diamond crystal. Under microwave excitation, a plasma state of carbon atoms is created in a range of temperature between 700 and 1200°C. When a diamond substrate is present, graphite tends to build up over the epitaxial surface and is etched away by the hydrogen radicals, enabling formation of the diamond structure along the crystallographic orientation of the diamond substrate. Other than carbon atoms, a minimal content of nitrogen in the chamber can take the place of the carbon deposition, at the lowest level of 20 ppb [168]. This low nitrogen content makes diamond usable as laser gain material. Nowadays, Element Six Ltd. is the biggest company in the world that fabricates and commercializes high-purity CVD diamonds. Production cost has been reduced in the last decade such that diamond is nowadays competitive with other Raman crystals.

When considering diamond for a Raman laser, the crystal orientation with respect to the pump field polarization has to be taken into account to maximize the performance. The atom disposition in the (011) plane is represented in Fig. 3.8. The Raman

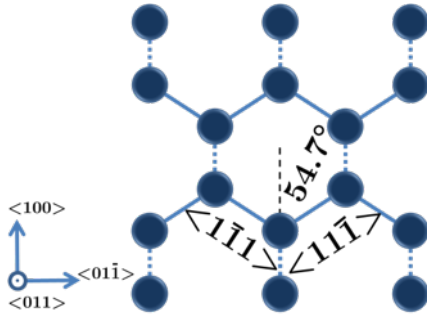

Figure 3.8: Schematic of the bulk diamond structure in two dimensions. Dashed lines represent covalent bonding in the (011) plane (parallel to the page), while dashed lines connect carbon atoms in a direction not parallel to the page.

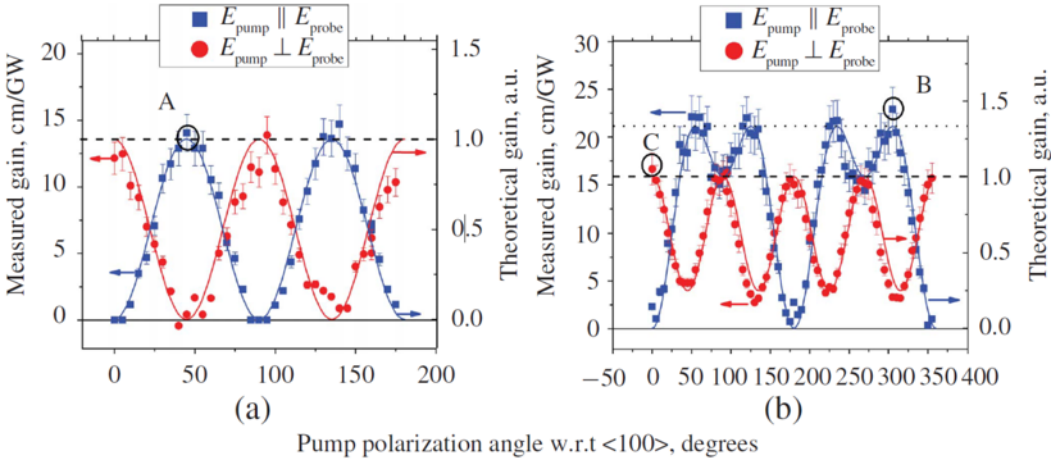

Figure 3.9: Diamond Raman gain polarization at 1064 nm for crystal orientation such that the beam propagates along the <110> (*left*) and <100> direction (*right*). Image taken from ref. [170].

gain magnitude is determined by the polarization direction of the pump field relative to the direction of the carbon-carbon bonding [169]. Savitski et al. in 2012 measured the Raman gain as a function of the angle of the pump polarization field via the pump-probe technique for two crystal orientations [170], whose main results are depicted in Fig 3.9. It was demonstrated that the polarization dependence of the gain has the same periodicity as the lattice (54.7deg). The same group (2013) showed maximum gain of 17 ± 2 cm/GW at 1064 nm with $\sim 1/\lambda$ dependence from 355 to 1280 nm for pump polarization parallel to the <111> direction [143]. The literature on synthetic diamond Raman lasers starts from 2004, when Kaminskii et al. demonstrated a single-pass Raman laser

with multi Stokes and anti-Stokes generation, pumped by an ultrafast laser [171]. At that time, the content of nitrogen impurity was not less than 1 ppm [171]. While the fabrication of high-purity diamonds was under improvement, Mildren et al. in 2009 reported Raman laser operation of a high-quality diamond in an external cavity with a maximum conversion efficiency of 63.5% at the first Stokes wavelength [172]. A Raman laser with near-quantum-limited efficiency of 85.8%, was also reported at 1240 nm using a CVD diamond with low birefringence ($\Delta n < 10^{-6}$) [173]. To date, the highest average output power of 24.5 W was reported in 2011 by Feve et al., demonstrating Raman laser operation at 1193 nm under room and cryogenic temperature (77 K) [174].

When considering diamond for continuous-wave operation, laser efficiency becomes more sensitive to the material quality, in which a minimal amount of defects can still induce optical absorption loss and birefringence. This has a detrimental impact on the total conversion efficiency. To reach a low threshold, diamond is usually inserted within the fundamental cavity. At the Institute of Photonics of the University of Strathclyde, Kemp et al. demonstrated for the first time, in 2009, CW Raman laser operation at 1240 nm [175]. Since then many other results of CW diamond Raman lasers have been reported. For instance, Parrotta et al. (2013) reported 4.4-W output power ($>$ 14% conversion efficiency) from a SDL-pumped Raman laser with a single Stokes shift at $\sim$1200 nm (Parrotta et al., 2013). CW operation was also demonstrated in an external cavity for the first time in 2012 by Kitler et al. [176], reporting 10.1 W of maximum output power at 1240 nm with 32% input-to-output conversion efficiency. More recently, Raman laser operation was observed in an external cavity under single-mode oscillation with up to 3.5 W of output power pumped by a CW single-frequency distributed feedback laser [177]. When the second Stokes oscillation was enabled in diamond, the same group demonstrated a tuneable single-mode diamond Raman laser for water vapour detection in the 1480 nm region [153]. In 2018, Jasbeer et al. reported a high power diamond Raman laser in quasi-CW for frequency doubling conversion in the red-orange region using a LBO crystal intracavity, reaching up to 30 W output power at 620 nm with $M^2 = 1.1$ [178].

In the work described in Chapter 4, diamond will be included in the cavity setup

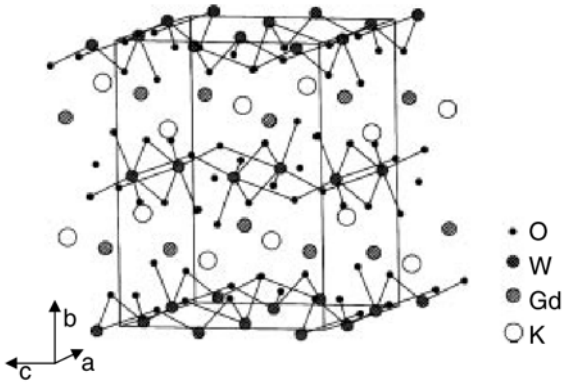

Figure 3.10: The $KGd(WO_4)_2$ lattice structure. Image taken from Ref. (Macalik, Hanuza and Kaminskii, 2002)).

of a CW infrared SDL. The large Raman shift of diamond (1332 cm^{-1}) is suitable to shift the laser emission wavelength towards nontrivial spectral regions, in this case well beyond the 1.2 μm upper wavelength limit of InGaAs-based SDL gain structures.

3.6.2 KGW

In contrast to diamond, the lattice symmetry of a potassium gadolinium tungstate oxide [$KGd(WO_4)_2$, or KGW] cell is less symmetrical. The more complex structure of such a material characterizes the KGW with more non-degenerate phonon oscillation modes than in diamond. The KGW unit cell is monoclinic and belongs to the C_2/c space group. Its schematic three-dimensional lattice structure is illustrated in Fig. 3.10. Due to the low symmetry of KGW, its mechanical, thermal and optical properties are anisotropic. Figure 3.11 shows the spontaneous Raman spectra of the KGW crystal. The crystal is often exploited for its most intense 901.5 cm^{-1} Raman peak [179]. The symmetric stretching vibration of the $(WO_4)^{2-}$ tetrahedra is responsible for the strongest intensity Raman modes located at 901 and 767 cm^{-1} depending on the pump field polarization [180]. These also correspond to the same oscillation modes in other potassium tungstate materials, such as KReW (where Re = Y, Lu, Dy, Yb) [181–183]. Minor Raman peaks in the 270-1000 cm^{-1} range can also be observable, mostly attributed to different modes of oscillation of $(WO_4)^{2-}$ ions [180]. Thanks to its large transparency (0.35-5.5 μm) and high damage threshold (¡10 GW/cm^2) and

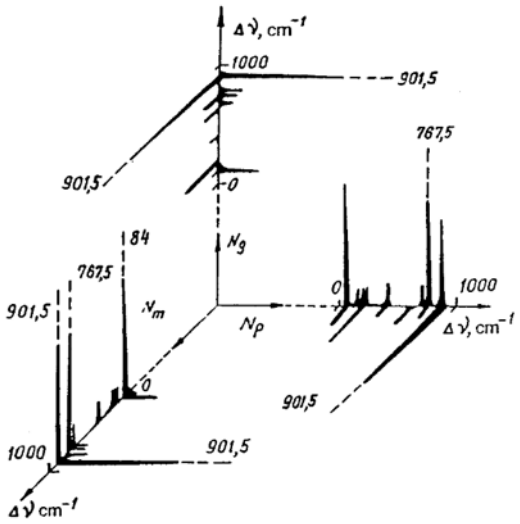

Figure 3.11: Spontaneous Raman spectra of KGW for different polarization directions. Image taken from Ref. [179].

good Raman gain (∼6 cm/GW at 1 μm [170]), single crystal KGW has been employed as a Raman shifter of several visible and infrared lasers, in both the CW and pulsed regimes. Typically, KGW is oriented such that the pump field is co-polarized to the 901 or the 767 cm^{-1} Raman mode. The 901 cm^{-1} Raman shift is dominant for pump beam propagation along the crystallographic $c-$axis (parallel to the optical N_p axis) when the electrical field is parallel to the N_m optical axis. This pump excitation scheme can be expressed as $p[mm]p$ [179]: $p[m$ denotes the pump beam propagation and its field polarization parallel to the N_p and N_m axis respectively; while $m]p$ is referred to the excited field orientation and propagation direction. The Raman shift at 767 cm^{-1} is instead achievable when the beam is propagating along the $N_p$axis and is polarized along the N_g axis ($p[gg]p$ excitation). The N_m and N_g axis are rotated by 24deg and 20deg respectively to the a and b axis [179], as shown in fig. 3.12. KGW can be doped with laser-active Nd^{3+} ions for laser emission at 1064 nm and self-Raman conversion at longer wavelengths within the same material [179]. Its laser proprieties have been considerably attractive for having a stimulated emission cross section comparable to those of Nd:YAG [184]. Sometimes, the apparent advantage of a compact self-Raman laser is dampened when one wants to optimize the cavity modes of the fundamental and the Raman laser independently. The first demonstration of self-conversion with Nd^{3+} doping

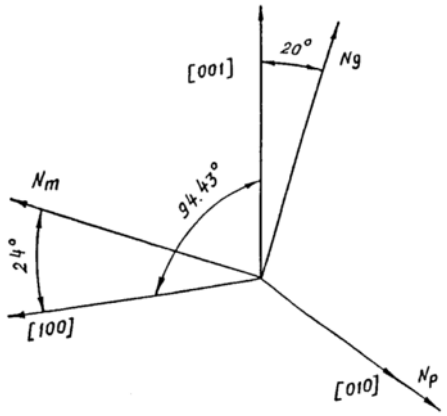

Figure 3.12: KGW optical axis orientation relative to the crystallographic direction. Image taken from ref. [179].

was reported in pulsed operation [185]. The continuous-wave regime was demonstrated several years later by Demidovich et al. [133], who showed a diode-pumped intracavity scheme of a Nd:KGW for self-Raman conversion at 1180 nm. This system was very compact as the input coupler was directly deposited on a KGW facet, while the other side was AR-coated at the fundamental and first Stokes wavelength, which was output coupled (HR) by the external mirror. Later, Dekker et al. employed an undoped KGW for intracavity Raman conversion of a diode-pumped Nd:GVO laser [186]. In the same cavity a LBO crystal was added for SHG in the yellow. More systems can be found in the review of ref. [150]. A more important development in CW KGW Raman lasers was achieved by Parrotta et al. in 2011, reporting a tuneable Raman laser at the 1180 nm region via intracavity Stokes conversion of a tuneable SDL [35]. In Chapter 5 we report multi-Watt output power from a KGW crystal adopting a very similar scheme. Despite good Raman gain, however, KGW thermal conductivity limits the performance as the laser becomes very sensitive to the cavity alignment at a few Watts of output power [154]. On the other hand, KGW has a similar optical absorption at 1064 nm as diamond (∼0.1%/cm [170]) that the round-trip loss are low enough for achieving multiple Stokes conversion in CW operation. Indeed, by the development of high-quality ion-beam sputtered deposition, broadband HR and highly-transmissive coatings paved the way for long-wavelength CW lasers. For the research reported in this thesis (see

Table 3.1: Diamond and KGW properties.

	Diamond	**KGW**
Raman shift	1332 cm^{-1}	901 cm^{-1} $p[mm]p$ 767 cm^{-1} $p[gg]p$
Raman gain at 1064 nm	17 cm/GW <111> [143]	5 cm/GW $p[mm]p$ [170]
Raman linewidth (FWHM)	1.5 cm^{-1} [36]	5.9 cm^{-1} [179]
Absorption at 1064 nm	< 0.001 cm^{-1} [143]	< 0.004 cm^{-1}
Thermal conductivity	$\sim$2000 $WK^{-1}m^{-1}$	3.8 $K^{-1}m^{-1}$ [189]
Thermo-optic coeff. dn/dT	9.6×10^{-5} K^{-1}	-1.6×10^{-5} K^{-1} [189]
Refractive index at 1064 nm	2.54	2.01
Size (this work)	8x4x4 mm^3	30x7x7 mm^3
AR coating (this work)	$R < 0.2\%$ per pass (1160-1420 nm)	$R < 0.5\%$ per pass (1280-1750nm)

Chapter 5), both KGW and fused silica mirrors were coated for CW laser operation at the 1.1 – 1.7 μm range via cascaded Raman conversion. However, as described in Chapter 5, having such broadband coatings and high intracavity power, leads to parasitic Raman oscillation at different Raman modes simultaneously, such as $\sim$200 cm^{-1} associated with the phonon mode of GdO vibrations [187, 188].

When compared to diamond, KGW is still a good competitor in achieving high-performance Raman lasers. Diamond crystal symmetry and robustness undoubtedly prevail over KGW, and the fabrication of high-purity samples is now mature. The most important material properties of KGW and diamond are listed in Table 2.1. As far as it concerns the intracavity use as a laser material, diamond does not lend itself to broadband, very-low reflectivity coatings. At the time of the experiment presented in Chapter 4, manufacturers had not been ready yet to fabricate and guarantee broadband coatings on diamond with $< 1\%$ reflection loss per pass. Being chemically very stable, diamond surface chemistry makes such multi-layer coatings structure less robust and hence less durable than those deposited on KGW.

3.7 Challenges

Crystalline Raman media have a low steady-state gain, which causes the laser performance to be very sensitive to losses. In the intracavity geometry, the issue is ex-

acerbated by the fact that the Raman action itself generates loss to the fundamental cavity, creating a complex pump-varying dependence of the loss. Other factors, such as spectral broadening, optical losses, and thermal lensing, influence the Raman laser performance. Understanding the process of these detrimental effects is of particular importance to optimize the efficiency.

The deposition of multi-layers of dielectric AR/HR coatings is nowadays so accessible that is possible to reduce the optical loss transmission below $\sim 0.01\%$. Other than Fresnel reflection, absorption and birefringence are rather intrinsic properties of the Raman crystal. Unlike solid-state lasers, Raman materials have to be transparent to the laser wavelength although absorption may still be relevant. For example, the diamond and KGW absorption coefficient is around ~ 0.005 cm^{-1} at 1 μm while the total loss depends exponentially on the crystal length [170]; a long crystal, at the same time, increases the gain per pass but it becomes more difficult to overlap the fundamental and the Stokes beams for mode-matching throughout the entire length. Therefore, a compromise has to be chosen to optimise the performance.

For maximum gain extraction, the electric field of the fundamental and Stokes lasers must be co-polarized. While the fundamental field orientation can be pinned by an intracavity birefringent filter, the Stokes field may experience depolarization loss by birefringent filtering while it propagates along the crystal. In an ideal crystal structure, both the fundamental and the Stokes fields track the direction of the optical axis. In reality, some imperfections may occur during the growth, such as impurities that infiltrate the structure from the external environment and the consequent formation of dislocations. Depending on the defect concentration, impurities produce optical absorption while dislocations induce stress and hence birefringence [190], which rotates the optical field out of the pinned pump field. The impact of birefringence on the diamond Raman laser behaviour was recently studied in more detail by Jasbeer et al. [162]. They mapped the birefringence magnitude parallel and perpendicular to CVD diamond growth direction, demonstrating that in the particular case of the CW regime, the Stokes laser polarization preferentially tracks the birefringence axes than the vibrational modes, even when the diamond is labelled as high-purity (i.e. low-

content nitrogen < 20 ppb [162]) and low-birefringence. Indeed, birefringence as low as $\Delta n \sim 10^{-6}$–10^{-5} is still sufficient to significantly affect the performance of a CW Raman laser [162].

Whilst pure CVD diamond is still susceptible to birefringence, its robust structure nevertheless provides high thermal conductivity and high damage threshold, which allows laser operation at high power with minimal thermal effects. In other more complex structures, such as KGW and BaWO, however, the heat deposited during Raman laser can severely affect the laser performance by thermal lensing, which will be the topic of the next subsection.

3.7.1 Thermal lensing

Unlike inversion lasers, in Raman media the stimulated Raman scattering is an inelastic process and the heat deposited in the crystal is hence directly proportional to the coupled output power rather than the absorbed pump power. The stored thermal energy generates a refractive index gradient across the crystal which modifies in turn the optical path of the beam, creating instability unless opportune compensation is established within the cavity. This is true when the Stokes pulse duration is longer than the time required for the crystal to build up thermal energy and relax, which is typically around more than few milliseconds. In the CW regime this condition becomes automatically satisfied.

The relationship between the thermal power loaded in the crystal and the Raman laser output power can be expressed as [34]

$$P_{heat} = P_S \left(\frac{\lambda_S}{\lambda_f} - 1 \right) \tag{3.25}$$

Where $\lambda_S, \lambda_f, P_S$ are the fundamental, the first Stokes wavelength and the time average Stokes power which can be considered in other terms the coupled Stokes output power. The second term of the right side of the equation is the relative difference of the energy between the pump and the Stokes photons that is deposited in the crystal during SRS. The strength of the thermal lens can be calculated by considering first the heat

propagation and the solution of the heat equation. Assuming radial flux of the heat generated from the point in which the Stokes photons are generated to the edge of the crystal, which is kept and controlled at constant temperature with an external heat sink, the heat distributes in the medium with a Gaussian profile and constant along the beam propagation direction, which is z in this case. Given these assumptions, the radial temperature distribution, $T(r)$, is the solution of the heat equation at steady-state

$$Q(r) = k_c \frac{\mathrm{d}^2 T(r)}{\mathrm{d}r^2} \tag{3.26}$$

Where k_c is the thermal conductivity of the Raman crystal; $Q(r)$ is the heat generated by SRS per unit volume, and r the radial coordinate. Once the gradient temperature is established, the refractive index changes consequently by the effect of three main factors: thermo-optical, end-face bulging, and the photoelastic effect. The refractive index change can be expressed by the following formula considering a cylindrical material with radius r_0 [34]

$$\Delta n(r) = \Delta T(r) \left[\frac{\mathrm{d}n}{\mathrm{d}T} + \alpha C_{r,\phi} n_0^3 + \frac{\alpha r_0 (n_0 - 1)}{l} \right] \tag{3.27}$$

Where dn/dT is the thermo-optic coefficient, α the thermal expansion coefficient, $C_{r,\phi}$ is related to the elasto-optic effects, n_0 and l are the refractive index and the length of the material respectively. Typically, in most end-pumped materials, the thermo-optical effect is the most dominant one and $\Delta n(r) \sim \Delta T(r) dn/dT$, where dn/dT is calculated to be 10^{-6}–10^{-5} K^{-1} for many Raman crystals.

Generally, the optical field passing through a thin lens experiences a phase shift, $\Delta\phi$, which can be demonstrated equal to [191]

$$\Delta\phi = \frac{kr^2}{2f}, \tag{3.28}$$

where k is the wavevector and f the lens focal length. For a thick material, the phase

shift is set by the refractive index gradient along the crystal length, l,

$$\Delta\phi = \int_0^l k\Delta n(r,z)\mathrm{d}z \tag{3.29}$$

For a material subject to thermal lensing in which the thermo-optic contribution is the greatest, the thermal lens strength can be derived by combining the temperature gradient profile given by Eq. 3.27 with Eqs. 3.26 and 3.28,3.29 [34, 191]

$$f_{th}^{-1} = \frac{\mathrm{d}n}{\mathrm{d}T}\frac{P_s}{\pi\omega_s^2}\frac{1}{k_c}\left(\frac{\lambda_S}{\lambda_f} - 1\right) \tag{3.30}$$

The focal length of the thermal lens can be an additional parameter to add in the cavity design for further optimization. Typically Raman crystals have negative focal length due to negative dn/dT, while solid state lasers tend to a positive thermo-optic coefficient. Whatever the sign is, thermal aberration modifies the Raman mode of the cold cavity ($\pi\omega_s^2$) and, in turn, the optical power. Oscillation towards lower TEM due to Raman beam clean-up is also advantageous in reducing beam quality degradation. Therefore, focal length, output power and Stokes cavity mode are rather mutually dependent that an indirect measurement of f_{th} using Eq. 3.30 can be inaccurate and the laser performance sensitivity becomes highly dependent on thermal lens fluctuation. There are different techniques to estimate directly the value of f_{th}^{-1}, such as lateral shearing interferometry [192], which measures the phase distortions of a probe beam to estimate directly f_{th}.

According to Eq. 3.30, the strength of the thermal focal length can be reduced by designing the cavity with a larger Raman beam size although the laser threshold is consequently affected. A material with high thermal conductivity and low dn/dT can simplify the system and make the Raman cavity more stable to thermal lensing. However, to date, only diamond is capable of resisting the thermal lensing. Indeed, compared to the other most common Raman materials, the thermal conductivity of diamond is about 2000 W/mK against tungstate, iodate, and molybdate materials [34], having $k_c \sim$ 1-20 W/mK. For example, the thermal lens focal length generated by a diamond Raman laser per Watt of output power can be calculated to be $\sim$ 1 m, which

is typically larger than cavity length and therefore becomes negligible. On the contrary, other Raman lasers exhibit a much stronger thermal lens focal length ($\sim$ 10 cm [34]) so that compensation with an intracavity cylindrical lens [154] is required to avoid beam aberration.

3.8 Conclusion

In this chapter the general theory of Raman lasers has been reviewed. Stimulated Raman scattering is a $\chi^{(3)}$-nonlinear process that is useful for wavelength conversion of many laser sources. Normally the Stokes emission is the most exploited owing to the phase-matchless nature of this phenomenon, enabling laser emission towards the mid-infrared. This enables not only more accessibility in designing a compact cavity, but it also bestows automatic improvement on the laser beam quality when the Raman medium is pumped within the cavity of the pump laser itself, thanks to the Raman beam clean-up effect, which also contrasts thermal aberration. As a third-order nonlinear process, the Raman laser requires a high-intensity laser source to reach threshold. For continuous-wave operation, the intracavity configuration is the most employed as the high intracavity pump power (up to $\sim$kW) attainable in such systems allows low threshold. Also, the wavelength coverage can be further extended via wavelength tuning of the fundamental the Raman laser itself is not tuneable, and via cascaded Raman conversion if the round-trip loss is low ($\sim$ 1%) at each Stokes wavelength. Continuous-wave intracavity Raman lasers operate, however, in a highly-dispersive regime, preventing correlation between the fundamental and Stokes fields, and hence reducing the effective Raman gain, particularly true for a broad multimode pump. In this case, effective gain reduction can be minimized when the pump spectrum is reduced in linewidth within the Raman gain bandwidth by the introduction of etalon filters.

Thermal effects also impact on the laser performance due to the heat deposited in the scattering process. Diamond is a suitable Raman tool for generating high output power with negligible thermal effects, thanks to its highest thermal conductivity. Chapter 3 will be dedicated to the performance of such material in the near and mid-

infrared when intracavity-pumped by a SDL. KGW, on the other hand, is a good candidate for Watt-level emission in CW though the modest thermal conductivity may limit its potential. With the benefit of broadband AR/HR dielectric coatings deposition, the performance of long-wavelength cascaded Raman laser will be demonstrated and discussed in Chapter 5.

Chapter 4

Diamond for Raman laser emission at 1.4 μm with an SDL

There has been an increasing interest in technology to develop lasers for tuneable emission in 1.4-1.7 μm region. Current optical coherence tomography (OCT) technology employs different types of conventional light source, e.g. mode-locked, super-continuum, etc., to probe a biological material and return a stratified image of the object (such as the eye or the brain [123]) bypassing the strong water absorption wavelength region at 1.4 μm. Likewise, a narrow-linewidth laser can be instead applied to detect absorption features of water vapour when tuned across the 1.4 μm region. The recent development of compact, continuous-wave, tuneable and narrow linewidth semiconductor disk lasers (SDLs) at infrared wavelengths can pave the way for their implementation in these medical and remote gas sensing systems and hence potential alternative sources to the bulk solid-state laser counterparts.

Nevertheless, there has been a lack of advancement in SDLs operating efficiently in >1.4 μm region. SDLs emitting directly in the 1.3-1.5 μm are typically realized with quaternary materials, but they present some complications. For instance, the realization of InGaAsAl QWs for emission around 1.3 and 1.5 μm prevents the integration of a monolithical DBR-SDL gain structure and consequently it makes use of alternative but complex techniques such as wafer fusion [13,33]. Our approach to reaching the eye-safe

wavelength region is via Raman conversion of the more robust and commercially-tested InGaAs material [89].

The recent development of high-power InGaAs SDLs towards 1180 nm has opened the possibility of extending the Raman wavelengths even further, thanks to the improved fabrication technique of strain-balanced InGaAs SDLs [14]. Indeed, we developed a laser at 1320 nm via intracavity Raman conversion of a high-strain InGaAs emitting SDL [91]. The down-conversion to 1320 nm was possible via the insertion of a pure crystal of KGW into the SDL extended cavity. KGW has multiple Raman shift features with the largest being 901 cm^{-1}, therefore crystals with a Raman shift far wider than 1000 cm^{-1} would be a suitable candidate to tailor InGaAs SDL for emission in the eye-safe region with a single Raman shift. Amongst all Raman-active crystalline materials, only diamond meets this characteristic having a Raman shift of 1332 cm^{-1}. Synthetic diamond has also become more accessible in recent years such that it has been incorporated in many Raman laser designs and components [137], enabling high-power operation as a result of high thermal conductivity and growth purity.

In this chapter we will show how laser operation at 1.4 μm can be reached via Raman conversion of the same InGaAs-based SDL structure emitting at 1180 nm using diamond. The next pages will be dedicated to the characterization of the InGaAs SDL used for the Raman experiments and the Raman results achieved with the diamond, giving also particular emphasis to the analysis of spectral broadening.

4.1 InGaAs SDL for 1180 nm

The SDL gain structure and sample mount used for this project was provided by the research group headed by Prof. M. Guina at the Optoelectronics and Research Centre in the University of Tampere (Finland) and it is similar to that one reported in Ref. [193].

The gain structure (see Fig. 4.1), was grown via molecular beam epitaxy and included ten 7-nm thick InGaAs/GaAs quantum wells, located at the anti-nodes of the anti-resonant standing-wave field of ∼1180 nm and monolithically grown on top of 25.5-pair AlAs/GaAs distributed Bragg reflector (DBR). Laser generation at 1180

Table 4.1: Materials and composition of the SDL gain chip used in this work.

Material	**Composition**	**Thickness (nm)**
Window layer	AlGaAs	20
Capping layer	GaAs	10
Quantum well	$10\times$GaAs/$In_{0.37}Ga_{0.63}As$	7
Compensating layer	$GaAs_{0.89}P_{0.11}$	not given
DBR	$25.5\times$AlAs/GaAs	not given

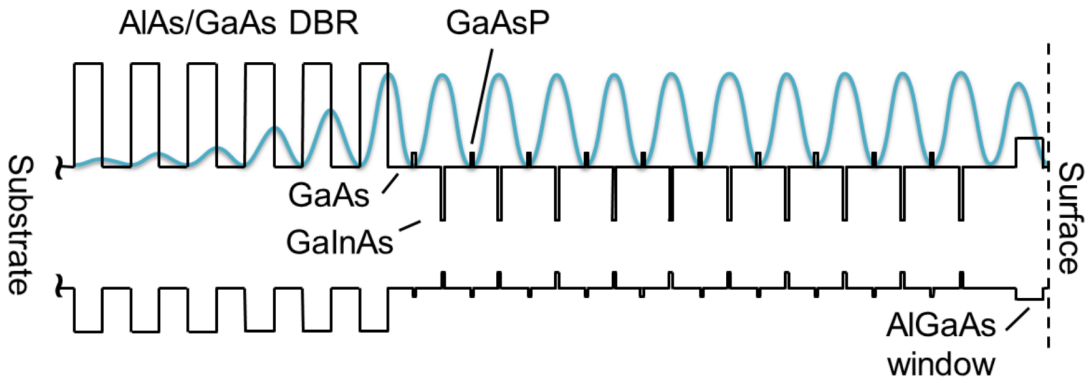

Figure 4.1: Schematic illustration of the SDL gain structure showing the semiconductor bandgap and alignment of the layers with the optical field (not to scale).

nm required indium fraction of 37%, which results in sufficient compressive strain such that barriers of tensile-strained GaAsP were needed, placed at the nodes of the standing wave to provide strain-compensation for the whole gain structure. A window layer of 20-nm thick AlGaAs and 10-nm thick GaAs was deposited on top to cap the structure and limit oxidation from the external environment. More details of materials and composition are listed in Table 1.

The wafer was cut into 2.5x2.5 mm^2 chips, bonded to a 300-μm thick diamond heatspreader via liquid capillarity using distilled water. Capillary bonding is a standard technique [74] to obtain a good thermal and optical contact between the diamond window and the semiconductor chip surface as the high surface tension of water establish an hydrostatic pressure that pulls the two materials to uniform contact as long as the surfaces are clean and smooth [74] . The diamond-bonded sample is eventually clamped to a water-cooled (10°C) brass mount (see Fig. 4.2) with an indium foil on the substrate side for thermal management. To avoid an etalon effect and enable continuous tuning,

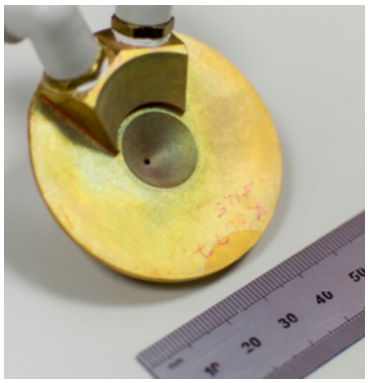

Figure 4.2: Photo of the mount used to clamp the SDL chip.

the heatspreader was wedged (2°) and anti-reflection coated at 1180 nm [14, 193].

4.1.1 Pump optics setup

The SDL was optically-pumped by an 808-nm fibre-coupled diode laser with a nominal maximum output power of 400 W. The pump light was emitted from the fibre with radius 200 μm, and numerical aperture 0.22 (or ∼0.22 mrad half-angle) and hence M^2 = 172. Given this high-divergence pump laser and the mount of the SDL (see Fig. 4.2), external focusing optics to direct the pump beam onto the sample were necessary.

Ideally, a set of aspherical lenses would offer a top-hat beam profile reducing chromatic aberration and also a uniform pump more beneficial to the SDL. The aspherical lenses available had ∼3 cm focal length, but were too big (∼5 cm diameter) to be mounted close to the SDL. Therefore, we used an aspherical lens for collimation and a smaller spherical lens with the same focal length for focusing, i.e. for direct imaging of the end of the fibre. Figure 4.3 shows the telescope system used.

To measure the actual size of the beam we focused the pump to a CMOS camera with a folding angle of ∼40°, which is the minimum angle with which the SDL beam can run compatibly with the cavity geometry. The maximum input pump power to the camera was limited to a few mW, therefore we reduced the input power with a neutral density filter. Figure 4.4 illustrates the image of the pump at low power and the data curves acquired along the horizontal and vertical axis.

The radius of the pump beam was measured to be 233 μm x 330 μm at $1/e^2$

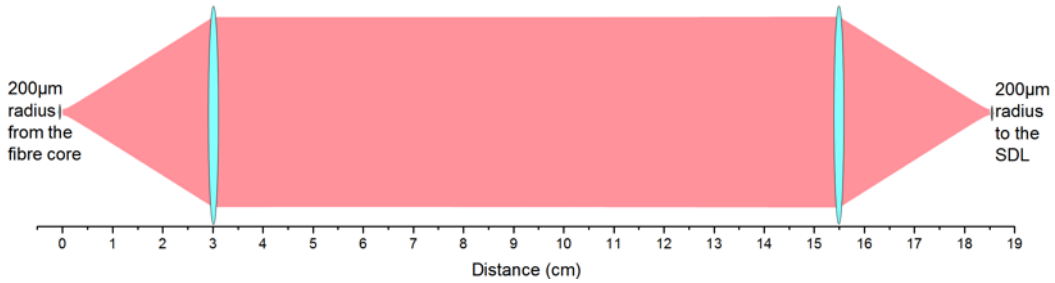

Figure 4.3: Diagram of the pump optics used to image the output of the pump fibre at the SDL gain structure.

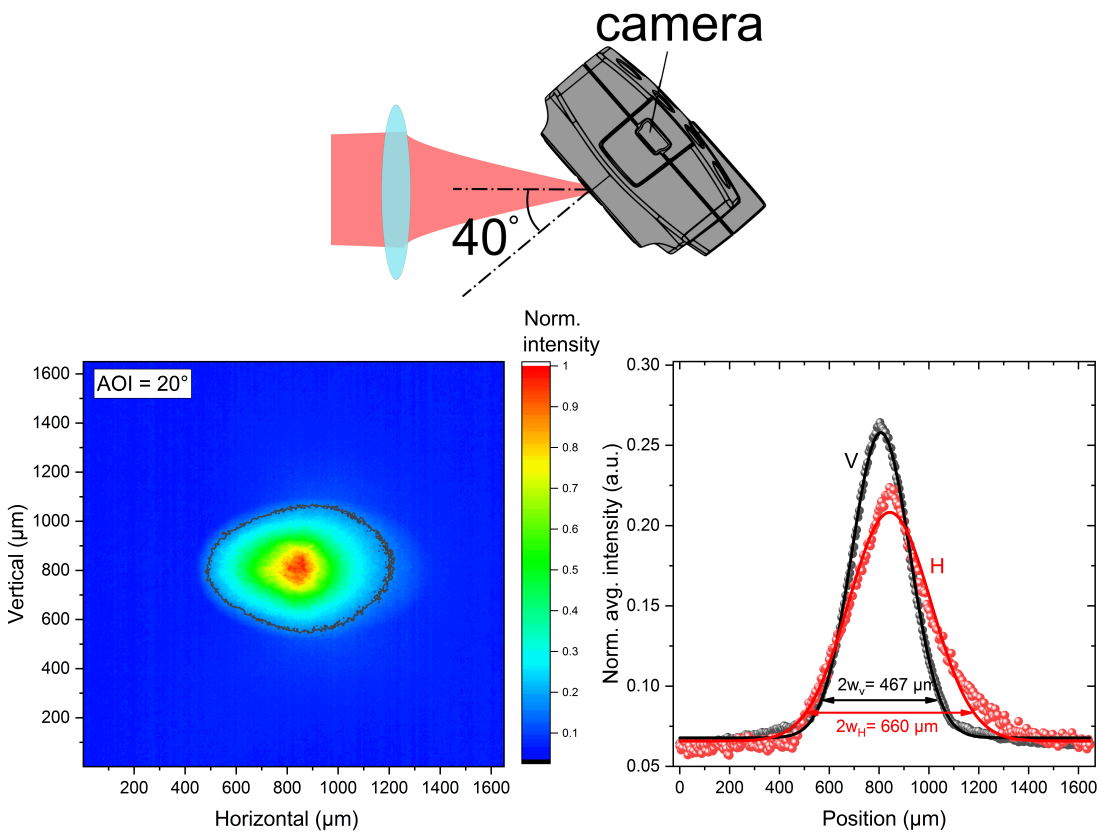

Figure 4.4: *Top*: Position of the CMOS camera with respect to the focusing beam. *Bottom left*: image of the 808 nm beam profile intensity at ∼1 W acquired with a ThorLab CMOS camera. The black isocurve indicates the points at which the intensity reaches $1/e^2$ of the maximum; *bottom right*: average of the beam intensity along the vertical and horizontal direction with the corresponding Gaussian fit. The full-width is indicated by $2w$ at $1/e^2$.

of the maximum value, but it can vary significantly by tweaking the distance of the focusing lens. Also, the index contrast between the diamond and the semiconductor

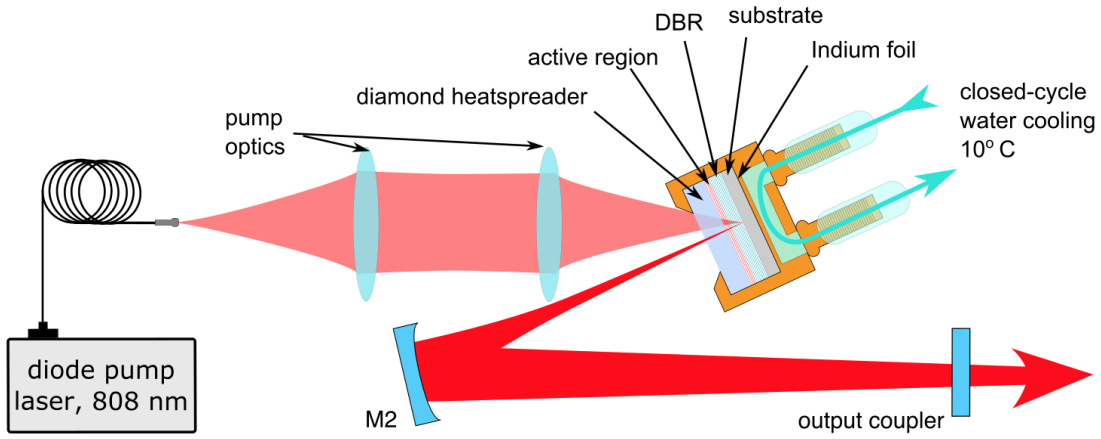

Figure 4.5: Diagram of the three-mirror cavity SDL. DBR: distributed Bragg reflector.

region reduces by some degree the angle of incidence and thus a small variation to the measured value needs to be taken into consideration. SDLs pumped by beams of such size require a few Watts of pump power to reach the threshold and several tens of Watt for a full power transfer characterization. However, the characterization of the beam profile was not possible at ≥ 1 W because the filters available for this experiment could not tolerate incident beam of such high intensity, so the actual beam shape and also dimension may vary at higher power.

4.1.2 SDL cavity design and characterization

The InGaAs SDL sample was tested in a V-shaped three-mirror cavity configuration consisting of a folding high-reflectivity concave mirror with 200 mm of radius of curvature, and (R >99.9%, 1160-1185 nm) and a plane output coupler as shown in Fig. 4.5. As the diamond heatspreader is bonded on the intracavity side of the chip surface, it can be calculated that the pump power that reaches the SDL gain structure (hereafter called absorbed pump power) is nearly 80% of the incident pump power after reflection.

We tested the samples in two different regimes: mode-matching, corresponding to a cavity mode radius at the SDL of 200 μm; and with a cavity mode radius of 100 μm, by changing the cavity length. A smaller cavity mode is also advantageous in the Raman experiment for reaching higher efficiency at the expenses of poorer beam quality [194] as Raman conversion automatically improves the output beam quality via the 'clean-up'

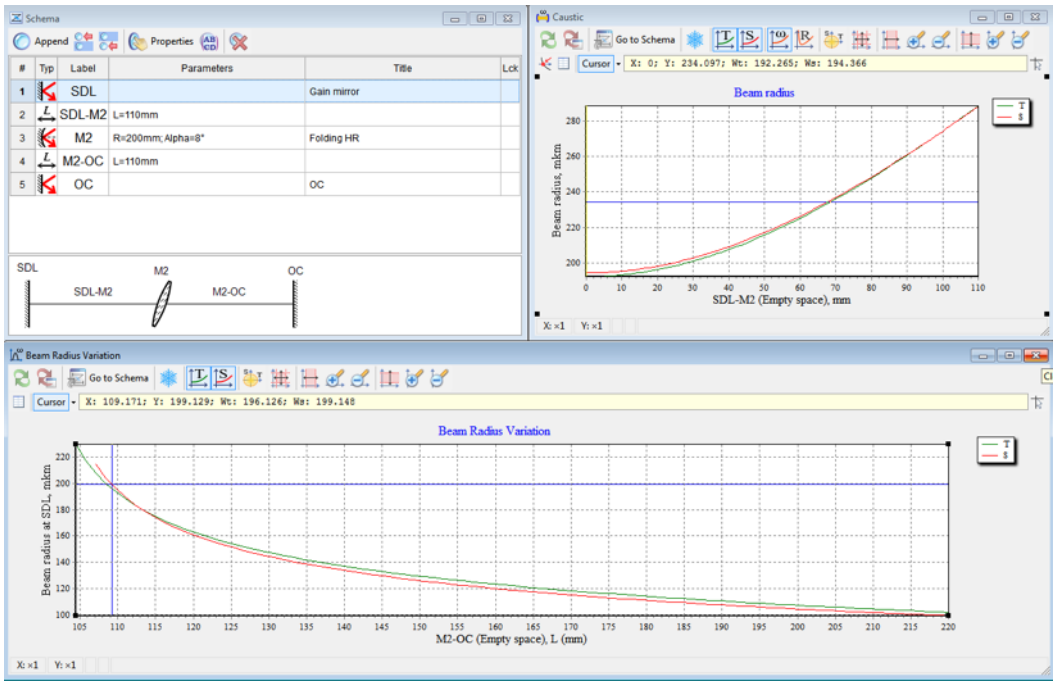

Figure 4.6: *Top-left*: cavity parameters; *top-right*: beam propagation along SDL-M2; *bottom*: beam size variation at the SDL chip as a function of the M2-OC distance.

effect [148]. Changing the laser cavity mode size was possible by extending the M2-OC arm from 110 mm to 200 mm, while the first arm length (SDL-OC) was maintained at 110 mm. The cavity arrangement was first designed by using ReZonator, which is software based on the ABCD matrix formalism. Figure 4.6 shows the screenshot of such software, which gives (top right) the beam propagation along the first arm SDL-M2 and (bottom) the variation of the cavity mode at the SDL chip while varying the M2-OC distance. For the characterization, a few output couplers with different transmissions at 1180 nm were used: 0.0038%, 0.8%, 1.6%, 2.7%. A comparison of the SDL power transfers in the two regimes for each output coupler (OC) is reported in Fig. 4.7.

The best performance was shown by the laser operating in the multi-mode regime, showing the highest output power of 17.5 W at 1.6% OC for 88 W of pump power, although the power did not decrease significantly during mode-matching operation, showing greater flexibility on the cavity design parameters for the Raman laser experiment.

Testing of the same gain structure had previously been carried out by our collab-

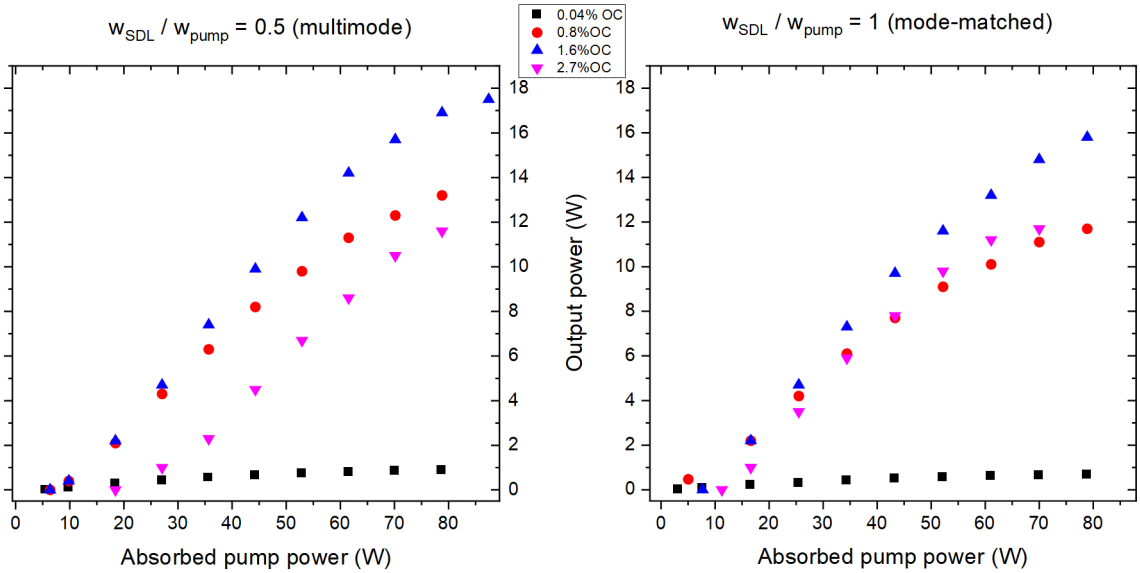

Figure 4.7: Power transfer characteristic of the InGaAs SDL at different output coupling (OC) in multi-mode operation (*left*) and mode-matching regime (*right*).

orators at the ORC, reporting congruent results with similar conditions [14]: ∼18 W at 1.5% OC for a water temperature of 5°C; but they recorded an output power even greater than 20 W with 3% OC when the coolant temperature was −10°C, while we reached a maximum output power of barely 12 W at 70 W of pump power with 2.7% OC when the water temperature was set at 10°C.

4.1.3 Caird analysis

In either regime, the output power is higher for higher output coupling up to an optimal OC, which is likely only a few percent due to the low-gain in this case ∼1.6% OC. By that, we can therefore estimate the cavity loss and the internal conversion efficiency taking into account the measured slope efficiencies plotted against the output coupler reflectivities and fit with the curve given in Eq. 4.1 [5], along the same lines of Caird analysis [195]. The Caird method is based on the linear relationship between the inverted slope efficiency and the inverted output coupler transmission [195]. Although Caird analysis was conceived for a 4-level laser [195], this method is still suitable for the estimation of the round-trip loss in an SDL if the losses are reasonably small and pump-dependent effects are negligible. As an alternative to this, Findlay-Clay analysis

is based on the relationship between the threshold pump power and the output couplers. However, given the variability of SDL threshold with the cavity set-up and pump power at optimisation, Caird analysis is better suited to this type of laser. Although Rigrod method [196] can be also utilized as it plots the output power as a function of the output coupler transmission and gain, we opted for the Caird analysis compatibly with most studies on SDLs to determine loss [7].

To tailor the Caird analysis to the SDLs, it is important to define the SDL slope efficiency and make some assumptions. The slope efficiency of an SDL (sometimes called differential efficiency [5]) can be simply thought as the relative number of photons converted into laser light. The slope efficiency is then limited by the quantum defect (η_{qd}), the internal conversion efficiency (η), the total reflection after a round-trip ($\mathrm{R_{tot}}$), and the output coupler reflection ($\mathrm{R_{OC}}$). This can be expressed as follows [5]:

$$\eta_{eff} = \eta_{qd}\eta\frac{\ln R_{OC}}{\ln R_{OC}R_{tot}} \tag{4.1}$$

Given the output coupler reflectivity, the quantum defect ($\eta_{qd} = \lambda_{pump}/\lambda_{laser}$) and the slope efficiencies determined by the power transfer in Fig. 4.3, it is possible to use the equation above as a fit function and extract the internal conversion efficiency and the derived round-trip loss trip, $L = 1 - R_{tot}$. A limitation is that Eq. 4.1 assumes no pump power dependency of the cavity loss and the internal conversion efficiency. This assumption can be expected true when the loss is low and before the rollover point. Otherwise, approaching the rollover, the antinodes of the standing-wave field shift towards longer wavelength, inhibiting an efficient resonant periodic gain, where conversion efficiency decreases with the pump power.

Both regimes did not affect the internal conversion efficiency, $\sim 60\%$ (see Fig. 4.8), while the SDL loss is somehow higher during mode-matched regime ($1.1\% \pm 0.2\%$) than multi-mode ($0.82\% \pm 0.22\%$), probably ascribed to a greater spurious laser absorption into the gain medium when the cavity mode was larger. Given higher performance in multi-mode regime, we therefore adopted this cavity mode radius for the Raman laser experiment. Also, intracavity-pumped Raman lasers do not require pumping with a

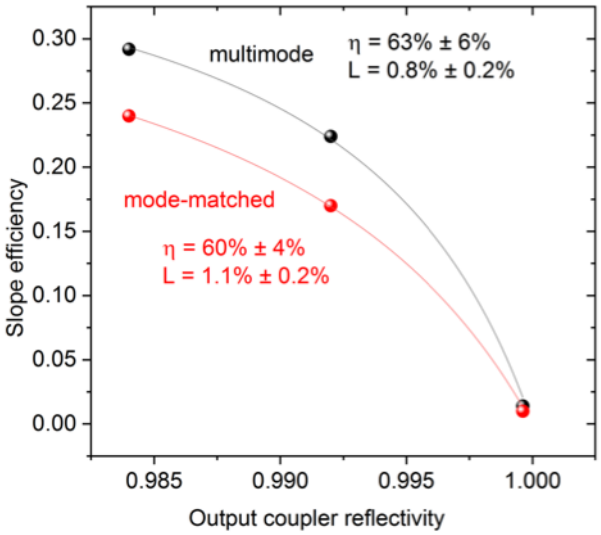

Figure 4.8: Slope efficiency as a function of the output coupler reflectivity fitted with the curve of Eq. 4.1.

single transverse mode as they can still be optimised for high beam quality, while taking advantage of the higher fundamental power, due to the beam clean-up effect [148].

4.1.4 Tuning

The anti-resonant design of the sub-cavity architecture of this SDL broadens the gain bandwidth and therefore broad laser tuning is possible [40]. To explore the entire gain bandwidth, we tuned the SDL emission wavelength with an intracavity 2-mm thick birefringent plate, pumping at medium pump power: 44 W, and 0.8% OC. This provided a maximum tuning range of 60 nm (see Fig. 4.9, violet data points), which corresponds to the gain bandwidth of the SDL. This was possible as the calculated free spectral range, FSR, of the 2-mm thick BRF, is FSR $= \lambda^2/\Delta nL = 76$ nm, where $\lambda = 1180$ nm, $L = 2$ mm and $\Delta n \sim 0.009$ for quartz.

Alternatively, we used a 4-mm thick BRF to tune the SDL wavelength over 37 nm (see Fig. 4.9, blue data points), which corresponded to the calculated free spectral range. The advantage of using a thicker BRF despite its limited free spectral range is a narrower emission linewidth, which is particularly convenient to achieve spectral-matching between the fundamental and the narrow Raman gain bandwidth of the

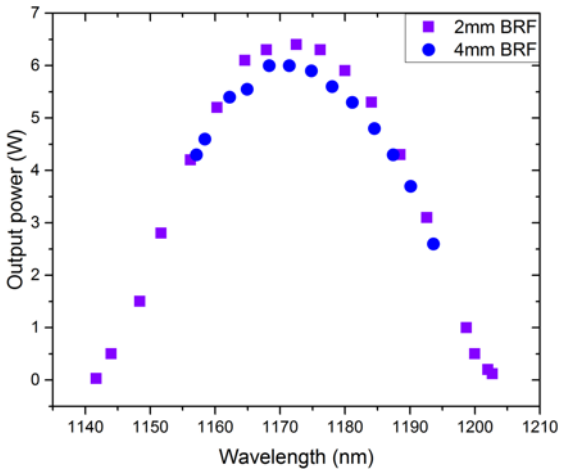

Figure 4.9: Wavelength tuning of the SDL with 2 and 4-mm thick birefringent filter (BRF). The SDL was pumped at 44 W and the output coupling was 0.8%.

diamond and hence improve Raman conversion efficiency.

The tuning results confirmed that the SDL operated with the highest power in the range between 1170 and 1180 nm, which was the wavelength range the SDL had been designed for. The maximum intracavity power was around a kW, which is beneficial for reaching Watt-level Raman laser conversion.

4.2 Raman cavity setup for 1400 nm emission

The extended version of the SDL with the diamond for Raman conversion at 1400 nm is shown in Fig. 4.10.

The SDL was optically-pumped with the commercial 808-nm fibre-coupled diode laser with the focusing optics as presented in the previous section. The distributed Bragg reflector (DBR) pass-band wavelength of the SDL was not designed to provide the desired high reflectivity at the Raman wavelengths, therefore we included the four-mirror Raman resonator within the fundamental cavity using a plane dichroic mirror (DM) with high reflection (R>99.9%) at >1290 nm and high transmission (T>99.9%) at <1200 nm. The flat dichroic mirror steered, with a folding angle of <5°, the Stokes beam onto the flat output coupler (OC). The other concave mirrors (M2, M3, M4, see Fig. 4.10) were high-reflection coated (>99.95%) for the 1150-1770 nm range. The

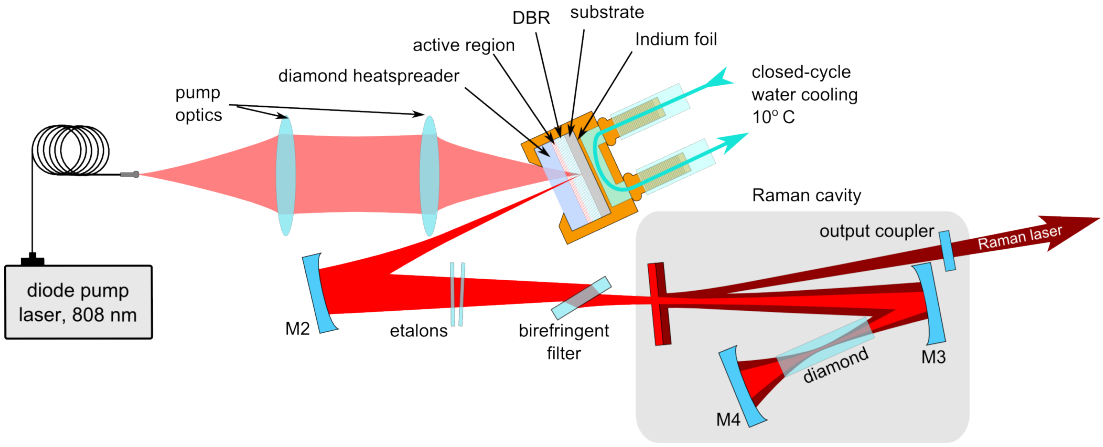

Figure 4.10: Schematic of the experimental setup of the SDL-pumped Raman laser. M2, M3, M4: high-reflectivity mirror; BRF: birefringent filter; OC: output coupler; RoC: radius of curvature; DBR: distributed Bragg reflector; HS: heat-spreader.

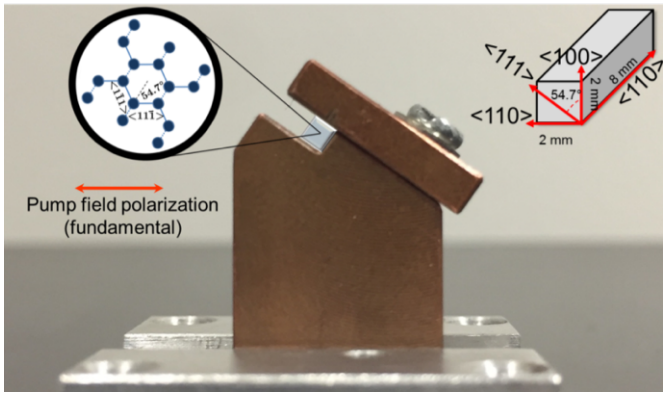

Figure 4.11: Photo of the brass mount that clamps the diamond for Raman scattering along the <111> axis. *Top-right*: schematic representation of the single-crystal diamond and its crystallographic axes.

whole Raman laser setup is shown in Fig. 4.10.

The extended cavity of the SDL, consisting of M2-M3-M4, was designed to produce a TEM_{00} beam with a calculated 160-μm spot radius at the surface of the gain sample and 41 μm beam waist radius at the centre of the 8-mm long diamond (mirror-mirror distance are given in Fig. 4.5). A 4-mm thick birefringent filter (BRF) was placed at Brewsters angle within the fundamental resonator to pin the polarization oscillation of the fundamental field along the horizontal direction and, at the same time, to enable tuning of the fundamental and thus the Raman wavelength. The Raman cavity shared

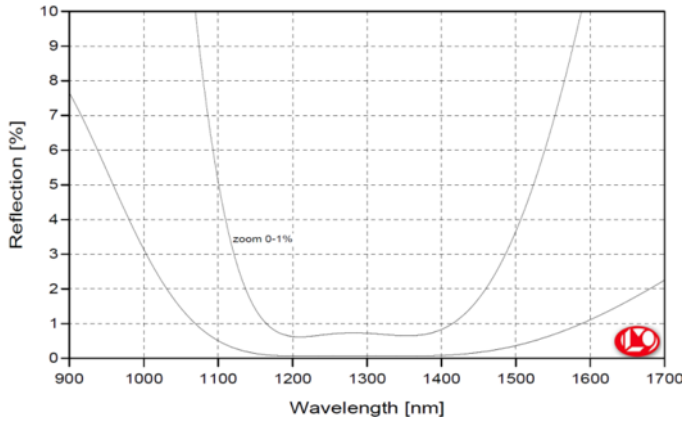

Figure 4.12: Calculated reflection curves of the diamond coatings (LaserOptik).

M3 and M4 with the fundamental and mode-matching in the diamond was possible by setting the M3-dichroic-OC distance to 340 mm.

To improve Raman pump efficiency and narrow-linewidth operation, Suprasil etalon filters with different thicknesses (50, 100 and 200 μm) were added within the SDL cavity and outside the Raman resonator for independent fundamental linewidth control.

4.2.1 Diamond sample

In this experiment we employed a synthetic single-crystal diamond for its broad high transparency in the near-infrared and the 1332 cm^{-1} Stokes shift to access laser operation in the 1.4-μm region. The diamond is 8x2x2 mm^3 and the 2x2 mm^2 facets were coated by LaserOptik for low reflection in the fundamental and Raman wavelength range, nominally R<0.2% at 1160-1420 nm. Calculation of the reflectivity curves of the coatings was provided by the supplier and shown in Fig. 4.12.

To improve the thermal contact with the brass mount, we wrapped the diamond with indium foil and no active cooling was performed. Unfortunately the square facets did not help us to see if the diamond <111> axis was placed horizontally or vertically. We therefore checked the laser performance twice, rotating it by 90°, to confirm the correct orientation.

The sample was plane-cut for beam propagation along a <110> axis and oriented such that the fundamental and hence the Stokes beam were co-polarised along the

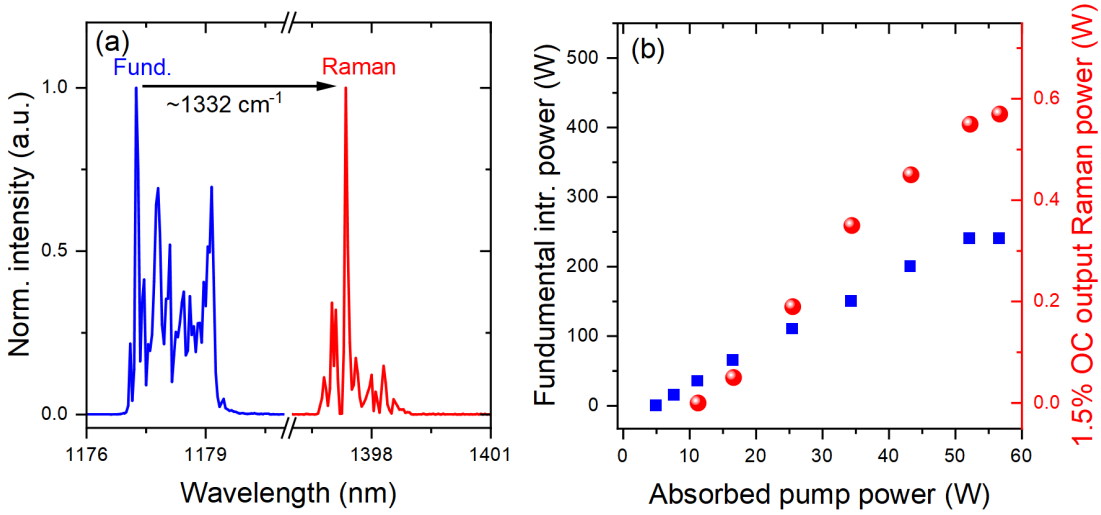

Figure 4.13: (a) Raman conversion spectrum of the InGaAs SDL. (b) Raman laser output power with 1.5% output coupling and intracavity power at the SDL wavelength (1180 nm) calculated as explained in the text.

<111> axis, corresponding to the carbon-carbon sp^3 bonding in order to access the highest Raman gain coefficient [169,173]. To orient the crystal, we clamped the diamond into a brass mount as shown in Fig. 4.11.

4.2.2 Broad emission and tuning

The diamond Raman laser was tested with 1.5%, 3% and ~ 4% output coupling (OC) for ~1400 nm emission. Figure 4.13(b) shows the output power transfer at 1.5% OC with a typical spectrum displayed in Fig. 4.13(a) (max resolution of the spectrum analyzer 0.05 nm). The Raman laser reached threshold at 10 W of incident pump power and ~50 W of intracavity power, which increased linearly up to 250 W, where the Raman laser exhibited a maximum output power of 0.6 W with ~ 1% total optical conversion efficiency. The fundamental spectrum was large ~3 nm (~20 cm^{-1}) leading to a broad Stokes-converted spectrum (see inset of Fig. 4.13). Note that the intracavity power of the SDL was calculated by dividing the leakage through the mirror M2 (see Fig. 4.10) and the transmission of the mirror at the fundamental wavelength.

Figure 4.14 shows tuning of the fundamental oscillation wavelength from 1161 to 1192 nm, via rotation of the intracavity BRF, which automatically tuned the Raman

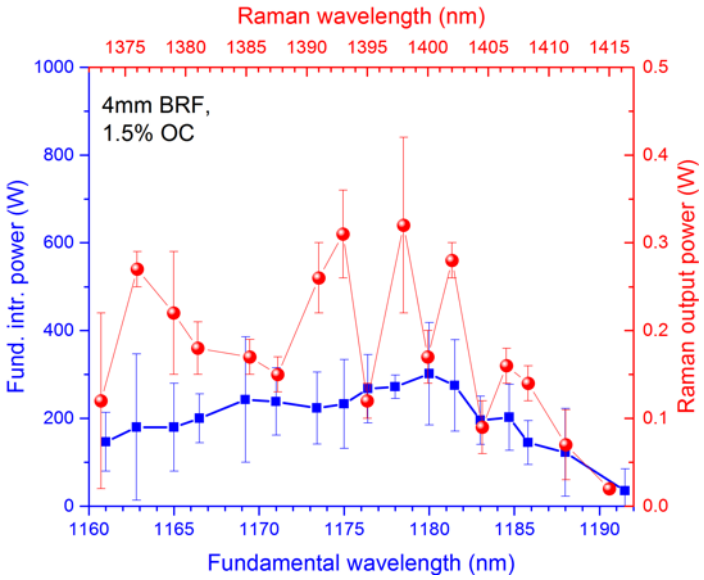

Figure 4.14: The tuning range of the intracavity fundamental field (blue) and the corresponding tuning range of the Raman laser output (red) for an absorbed pump power of 33 W with 1.5% output coupling.

laser from 1373 to 1415 nm. The tuning range, limited by the free spectral range of the 4-mm-thick BRF, was achieved with 1.5% output coupling. With rotation of the BRF, the fundamental oscillation demonstrated a relatively smooth tuning curve while the Raman laser tuning curve was discontinuous over the corresponding range. Discontinuous tuning in the 1400 nm region was also observed in a Cr:YAG laser [197] and was ascribed to varying absorption of water vapour in the atmosphere.

The estimated round-trip absorption loss due to water vapour can be calculated from the HITRAN database [95] for a 443-mm-long path of air (laser cavity length) with 50% relative air humidity 16°C, corresponding to a partial pressure of water vapour of 7 Torr. The resulting calculation of the water absorption spectrum from 1160 to 1740 nm is depicted in Fig. 4.15. It can be seen in Fig. 4.15(a) that water absorption in the fundamental tuning range is negligible or less significant (∼0.1%), while in the Raman laser tuning range the round-trip absorption spectrum varies with spikes greater than a few tens %, Fig. 4.15(b). This is indicative of the non-continuous tuning of the Raman laser. Indeed, intracavity Raman lasers have relatively low gain and therefore they are strongly affected by cavity loss of only a few percent. In our Raman laser resonator,

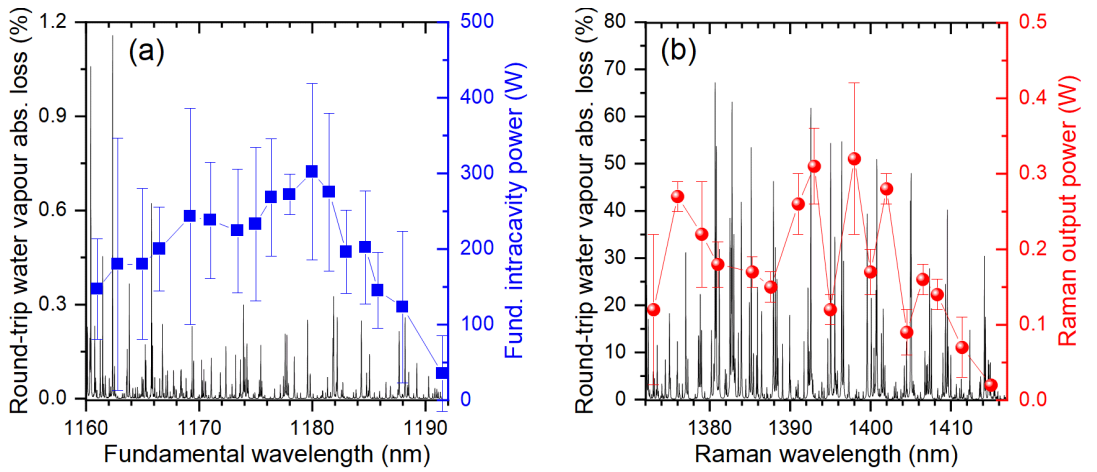

Figure 4.15: Estimation of the round-trip absorption loss due to atmospheric water vapour across the Raman laser wavelength range, calculated for our laboratory conditions using spectroscopic data from the HITRAN database (a)in the fundamental and (b) Raman wavelength.

the loss attributed to optics alone (i.e. dielectric coatings and diamond absorption) is calculated to be around 4.9%. A significant drop of performance was observed while tuning the laser to wavelengths at which the water vapour absorption is around 1% or higher. We believe that the performance of this laser could therefore be significantly improved with the implementation of an enclosed, dry air cavity. Incidentally, a single-frequency diamond Raman laser has recently been demonstrated for trace water vapour detection in the 1486 nm region with ∼5 nm tuning [153]. An SDL-pumped diamond Raman laser broadly tunable around 1400 nm (at the lowest extreme of the eye-safe spectral region), may also be attractive for this application.

In intracavity Raman lasers, spectral filtering of the fundamental field towards a narrower linewidth than the Raman gain lineshape has enabled the demonstration of optimum performance [89, 145, 198]. The emission bandwidth associated with our SDL spectrum was typically broader than the narrow Raman gain bandwidth of the diamond. Indeed, with no spectral filtering the fundamental exhibited, in the presence of Raman laser, a ∼20 cm^{-1} FWHM spectrum. The most recent measurement of the diamond Raman gain linewidth was made by means of transient coherent ultrafast phonon spectroscopy in a synthetic diamond grown by CVD [36]. This study reported a

Lorentzian-like Raman lineshape with 1.5 ± 0.07 cm^{-1} FWHM. Such spectral mismatch between the fundamental spectrum and the Raman gain bandwidth is detrimental to laser performance (see Section 2.3.1 and ref. [145]) and thus spectral control of the broadening mechanism has to be performed to reduce the fundamental spectral emission bandwidth, increase the effective Raman gain and hence the output power. Spectral control was achieved by inserting etalons, alone or in cascade, within the fundamental cavity in the arm between the SDL material and the dichroic mirror.

In general, the interference created by a Fabry-Perot etalon filter is determined by the thickness of the material, its refractive index, the reflectivity and the quality of the parallelism and flatness of the surfaces. The thicker the etalon, the smaller the separation between the transmission maxima (i.e. free spectral range); the higher the reflectivity the narrower the transmission peaks. The optical thickness depends on the angle of incidence, therefore the wavelength position of the transmission peaks can be slightly tuned by tilting the etalon plate. In these experiments we used only suprasil etalons with different thicknesses: 50, 100 and 200 μm. The wavelength-dependent transmission curve of an etalon can be theoretically calculated [199]

$$T(\lambda) = \frac{(1-R)^2}{1+R^2-2R\cos\phi(\lambda)}, \tag{4.2}$$

where

$$\phi(\lambda) = \frac{2\pi}{\lambda} 2nL\cos(\theta), \tag{4.3}$$

is the phase difference of the light field at the end etalon surfaces; R, λ, n, L, and θ, are the surface reflectivity, the laser wavelength, the refractive index, the thickness of the etalon material, and the angle of the incidence respectively. The separation between two maxima, the free spectral range (FSR), is thus given by

$$\mathrm{FSR} = \frac{\lambda^2}{2nL} \tag{4.4}$$

To better illustrate the impact of Raman laser oscillation on the fundamental spectrum and how this can be controlled, we show a comparison of the laser conversion spectra

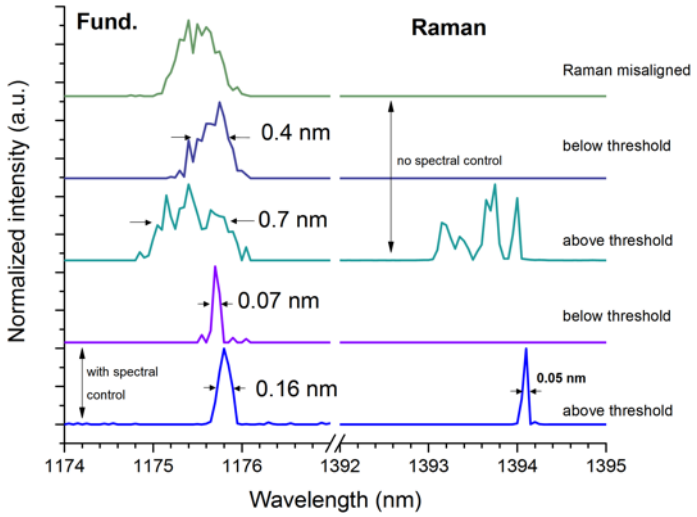

Figure 4.16: Fundamental and Raman laser spectra broadening. Linewidths are FWHM.

below and above the Raman threshold in Fig. 4.16. This shows the linewidth of the Stokes-shifted SDL emission without and with spectral control, under and above the Raman laser threshold. The fundamental spectrum at the same pump power in the absence of Raman conversion (Raman cavity misaligned) was taken as a reference. Spectral control was introduced via the use of intracavity etalon filters.

Without etalons, the fundamental modes oscillated within a 0.5 nm linewdith at the highest output power. (This differs from the larger width ($\sim$ 2 nm) of the fundamental spectrum reported in Fig. 3.8; however, the experimental conditions with which the two sets of measurements were performed such as mirrors and BRF alignment were not comparable.)

In either case depicted in Fig. 4.16, the fundamental spectrum FWHM enlarged by nearly a factor of 2 when just above the Raman threshold: from 0.4 to 0.7 nm and from 0.07 to 0.16 nm without and with the use of the etalons respectively. Despite the etalons, the fundamental emission still widened, most likely because the finesse did not guarantee narrower modulation. Ideally a reflection coated etalon plate would provide fundamental oscillation with higher finesse.

The spectral broadening mechanism of the fundamental in intracavity Raman lasers can be explained by the fact that when the fundamental modes within the Raman gain

linewidth reach the threshold, this induces a spectrally-varying loss, leading to a reduction of the intensity field spectrum of the fundamental and hence spectral broadening [198]. When the Raman gain linewidth is narrower than the fundamental linewidth, the effective Raman gain is therefore reduced, and this results in a non-optimal spectral overlap between the fundamental and the Stokes-shifted spectrum. In fact, Spence [145] suggested that in high-dispersion systems (SDL-pumped diamond Raman laser in this case) linewidths of the fundamental and the Stokes-shifted modes narrower than the Raman gain linewidth favour operation with higher effective Raman gain.

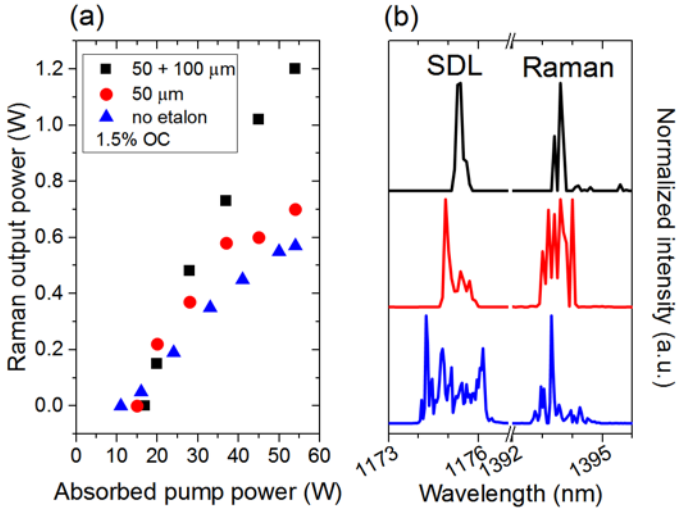

Figure 4.17: Raman laser power transfers for output coupler transmission of 1.5% with no etalon (blue triangles), with a 50-μm etalon (red circles), and with both 50 and 100-μm etalons (black squares) in the SDL cavity. (b) The emission spectra of the SDL and Raman lasers at 54 W of absorbed pump power with no etalon (blue), with 50-μm etalon (red), and 50 plus 100-μm etalons (black).

To illustrate how narrow fundamental emission led to higher output power, Fig. 4.17(a) shows the Raman laser power transfer with increasing filtering of the fundamental field: with no etalon, with a 50-μm etalon, and with both a 50 and a 100-μm etalon. At the highest pump power, the maximum output power was, respectively, 0.57, 0.7 and 1.2 W in each case. At the same time, as can be seen in Fig. 4.17(b), the additional etalons narrowed the full width at half maximum (FWHM) of the fundamental spectrum from ~2 nm (~14 cm^{-1} FWHM) to <0.2 nm (<1.4 cm^{-1} FWHM).

Further examination of the spectral evolution and the fundamental intracavity

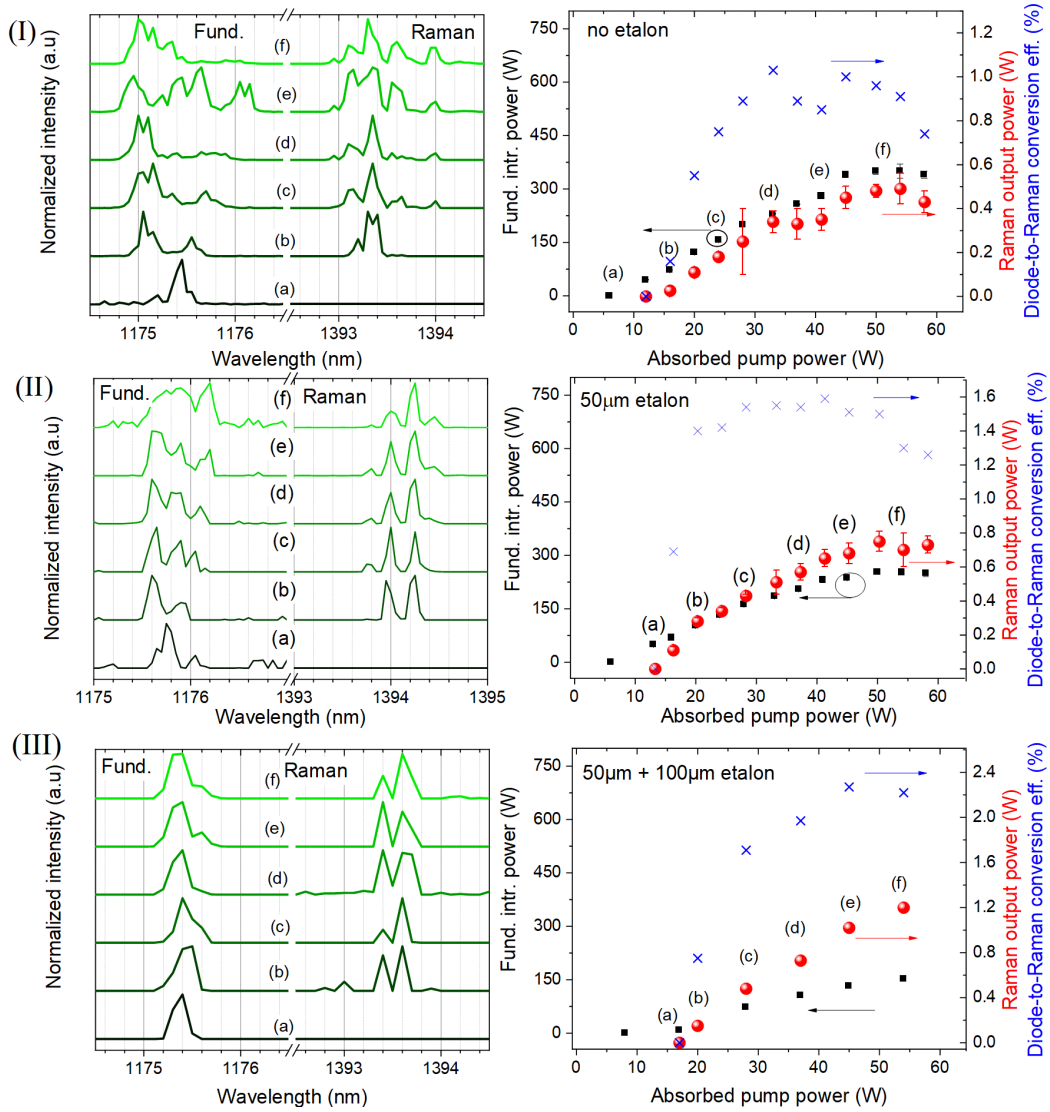

Figure 4.18: Raman laser output power with 1.5% OC (red spheres) and conversion efficiency (blue crosses) versus pump power without etalons (I); with spectral control using an intracavity 50 μm etalon (II); 50μm+100μm etalons (III). The fundamental intracavity power is also plotted (black squares). The evolution of the spectra were acquired with a 0.1-nm resolution optical spectrum analyzer and are coloured in gradient green. Note that the Raman output power and conversion efficiency share the same value in the right axis with the appropriate unit.

power over the full range of pump power is also reported in Fig. 4.18. In particular, the output power with 1.5% OC at the first Stokes wavelength and the Raman laser spectra versus the pump power were measured simultaneously with no etalon,

shown in Fig. 4.18(I); with 50 μm thick etalon, in Fig. 4.18(II); and with a pair of 50 and 100 μm thick etalons, in Fig. 4.18(III).

It can be seen that the use of the etalon filters to control the fundamental longitudinal modes contributed to increase the maximum output power of the Raman laser from 0.5 W when no spectral control was managed, to >1 W when a single peak was achieved. Conversely, the maximum fundamental intracavity power went down from 400 W with no etalon, to around 150 W with two etalon filters, showing that the pump-to-Stokes conversion efficiency has increased, although the additional loss due to etalons may have contributed to reduce the intracavity power as well. Spectra of both lasers over the full pump power range are reported in Fig. 4.18.

With no etalons (Fig. 4.18(I)), the Stokes laser reached the threshold at 12 W and was limited to a maximum of 0.5 W of output power, when the fundamental intracavity power clamped at ∼400 W. At pump power greater than 54 W the fundamental laser rolled off as well as the Raman one. In this configuration, the fundamental linewidth increased from 0.15 nm below the threshold to >0.5 nm above the Raman laser threshold. We observed multiple peaks equally separated by ∼0.25 nm at the fundamental wavelength that are not related to the etalon effect induced either by the diamond heatspreader or by the 6.35 mm thick dichroic mirror (these would give a free spectral range of ∼1 nm and ∼0.08 nm respectively), though we could not rule out that they contributed.

Figure 4.18(II) shows the power transfer and the spectral behaviour over the pump power with the 50-μm etalon. The maximum output power increased to around 0.8 W, higher than the previous configuration, but the linewidth was still as wide as 0.5 nm or even broader than the laser without etalons. Most likely, despite a calculated free spectral range of 9.6 nm at 1180 nm, the finesse of this uncoated filter was not high enough.

We then added a 100-μm thick etalon together with the 50μm etalon [Fig. 4.18(III)], which eliminated a few satellite peaks, increased the threshold to 17 W and improved the Raman laser to up to 1.2 W of output power. Indeed, when both etalons were added, the Raman threshold was maintained at around 15 W of pump power, leading to a

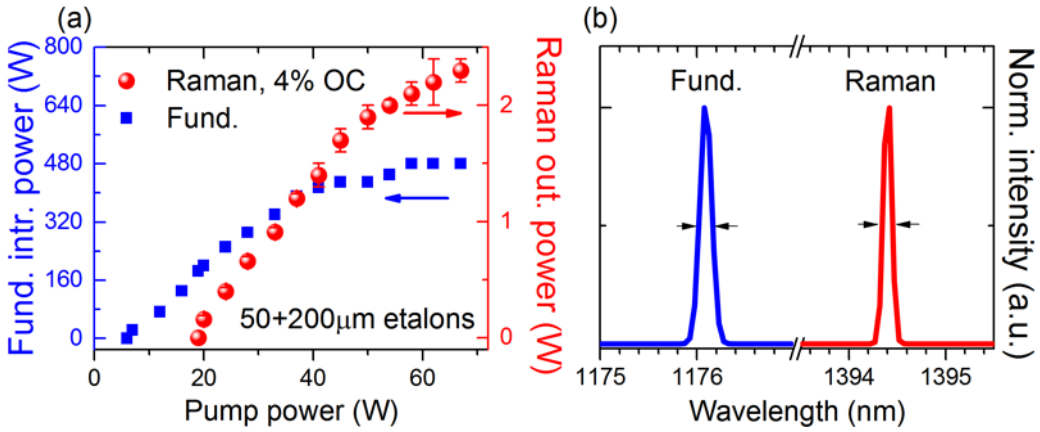

Figure 4.19: (a) Raman laser output power for 4% output coupler transmission with the 50-μm and 200-μm etalons in the fundamental cavity. The fundamental intracavity power is also reported (blue squares). The vertical red error bars indicate the maximum power fluctuation over 20 seconds. (b) The emission spectra of the fundamental (blue curve) and the Stokes-shifted laser (red curve) at high Raman power.

maximum output power of 1 W with 1.5% output coupling. The etalons were effective in supressing satellite peaks in the fundamental spectrum, though the Raman laser output power still exhibited a few etalon peaks. Albeit the employ of a single etalon with greater finesse would be preferred, two etalons were determinant to minimize any adverse spectral behaviour.

In fact, the combination of 50-μm and 200-μm thick etalons in the fundamental cavity determined the greater Raman output power with an output coupling transmission increased to ~4% at 1400 nm. Figure 4.19 shows the Raman laser power transfer along with the fundamental and Raman laser emission spectra at high power. The Raman laser emitted up to 2.3 ± 0.1 W with ~4% output coupler transmission at 1394.4 nm for a diode pump power of 67 W, where the error bar is referred to the maximum error. Above this, the output power of the Raman laser increased with a slope efficiency of 6% with respect to the pump power, and the fundamental intracavity field clamped at 480 W in the high-pump power region. Narrow emission linewidth was achieved at high power with 0.2 nm and 0.1 nm FWHM (instrument limited) respectively for the fundamental and Raman laser. Note that the vertical error bar of Fig. 4.19 is referred to the maximum error of the Raman laser signal over 10 seconds of acquisition.

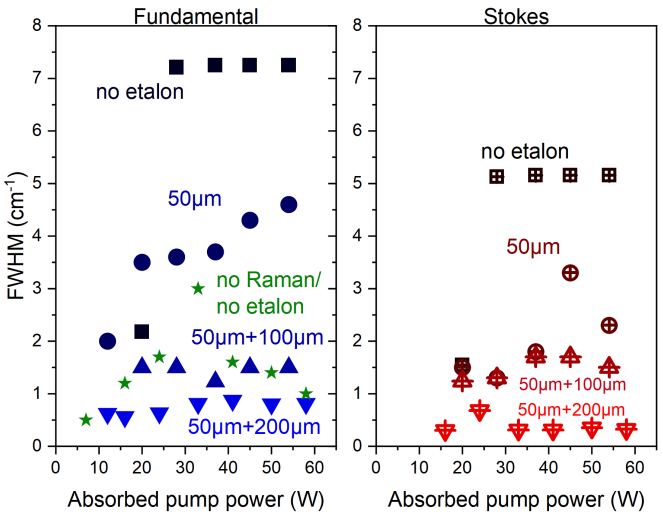

Figure 4.20: Full-width at half maximum (FWHM) of the fundamental (gradient blue) and Stokes spectra (gradient red) as a function of the pump power with and without etalons.

Such intensity fluctuations are mostly due to mechanical and thermal noise induced by water flowing and temperature-dependent effects. The laser stability can be therefore improved, for instance, via a temperature-stabilized thermoelectric cooling system for the SDL and the Raman material.

4.2.3 Spectral broadening evolution

A more careful investigation can be carried out by analysing the lasers spectra with and without etalons in order to better understand the spectral evolution and to what extent this affected the laser efficiency. Figure 4.20 shows the variation of the full-width at high maximum (FWHM) of the fundamental Stokes laser over the pump power range. The complex behaviour of most spectral shapes reported in Fig. 4.20 made it difficult to identify the exact width, but the FWHMs of all Gaussian fitting curves gave at least a general trend in the spectral broadening.

While the Raman laser was supressed by misaligning the output coupler of the Stokes cavity, fundamental modes typically broadened between 1-3 cm^{-1}. In the cases when the Raman laser was oscillating, the fundamental widened to 7 cm^{-1} with no etalon, 3-5 cm^{-1} with a 50-μm etalon, between 1-2 cm^{-1} with the 50μm+100μm

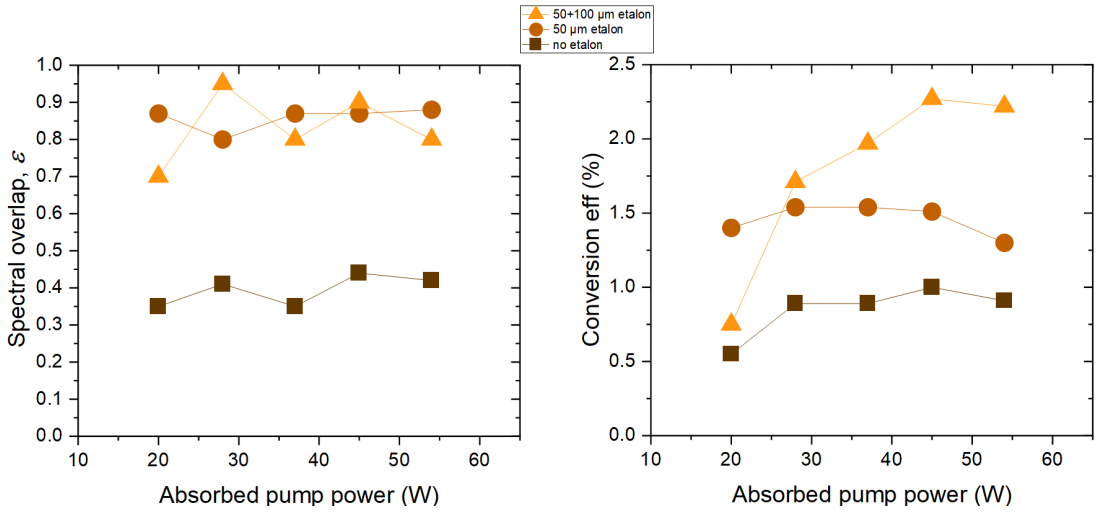

Figure 4.21: (*Left*) Spectral overlap factor data with and without spectral control; (*Right*) diode-to-Stokes conversion efficiency against diode pump power with different etalon thickness and 1.5% output coupling. The connecting lines serve to guide the eye.

etalons, and below 1 cm^{-1} when 50μm+200μm etalons were used. In either configuration the Stokes emission tended to narrower linewidth than the fundamental. Correspondingly, without any spectral management it can be seen that the Raman laser had a maximum linewidth of around 5 cm^{-1} (1 nm), which decreased to values between 1.5-3.5 cm^{-1} (0.3-0.7 nm) with a 50μm etalon and, with two etalons, the emission linewidth went down to a minimum of 0.3 cm^{-1} (0.06 nm), limited by the instrument resolution.

These spectral differences reflect on the performance of the Raman laser itself, a study of which could provide some insight into spectral effects of intracavity Raman lasers. Spence et al. in [145, 198] suggested that in intracavity Raman lasers the effective Raman gain is reduced by the suboptimal spectral overlap between the Stokes spectrum and the fundamental response in the Raman material. Raman performance loss typically occurs when the Raman gain bandwidth is narrower than, or at most equals to, the fundamental spectrum. The Raman laser is therefore more susceptible to spectral broadening, affecting pump efficiency and hence laser performance. To calculate the spectral overlap factor, ε, the spectra were normalized to their area and the Raman lineshape was a simulated Lorentzian-like curve with a FWHM equal to

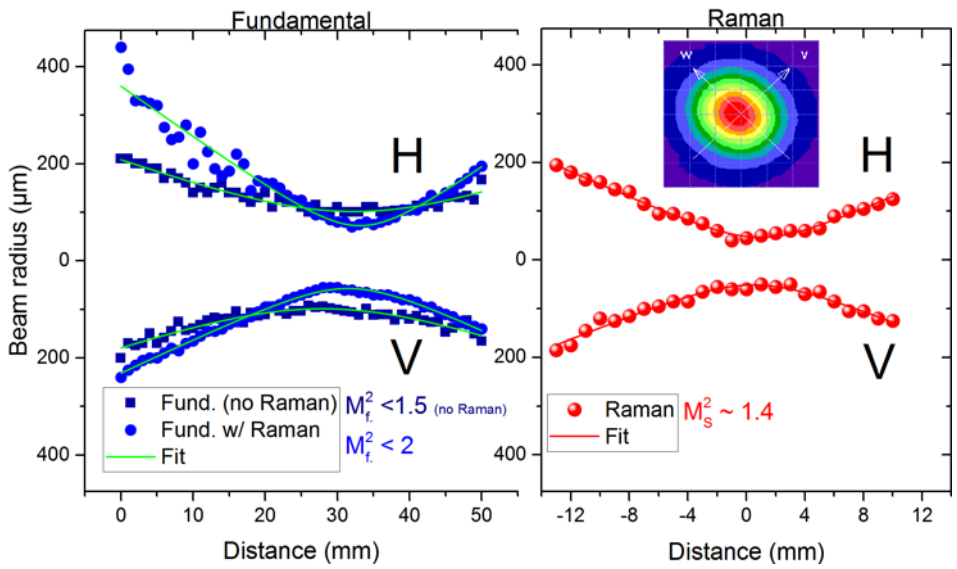

Figure 4.22: Beam radius variation of the fundamental (gradient blue) and Raman laser (red) along the horizontal (H) and vertical (V) axis. Inset: transversal near-field beam profile image at far field.

1.5 cm^{-1} and amplitude equal to the unit. Due to the narrow emission wavelength of these lasers, the external optics used for the spectra acquisition (e.g. mirrors, lens) did not require further calibration. According to the formula, the spectral convolution is calculated in wavenumber (cm^{-1}), therefore it was preferable to convert the spectra datasets in Fig. 3.17 to wavenumbers. Also, since the relationship between wavelength, λ and wavenumber , $\tilde{\nu}$, is non-linear, that is $\nu = \tilde{\lambda}^{-1}$, the calculation of the convolution needed a linear scale. Hence the wavenumber axis and spectral curves were interpolated to give a linear scale. The convolution was then multiplied by the area-normalized Stokes spectrum and its result integrated over $\tilde{\nu}$. The interpolation and convolution were calculated by the built-in function in the OriginPro software. The data of the spectral overlap factor and total conversion efficiency over the pump power with and without etalons are plotted in Fig. 4.21. Without etalons the effective gain was reduced by a factor between 0.35 and 0.45. When using the 50-μm etalon it increased to 0.8-0.9, and approached perfect overlap when two etalons were used.

Likewise, the use of etalon filters to achieve narrow-linewidth beams denotes, as shown in 4.21 (right), the improvement of the diode-to-Stokes conversion efficiency

from around 1% with no etalon to a maximum of nearly 2.5% with two etalon filters when a 1.5% of output coupler transmission was used.

4.2.4 Beam quality

In Raman lasers spatial mismatch of fundamental and Stokes beams also contributes to reduce laser performance [145]. Fig. 4.22 shows the variation of the radii of the focussed laser output beams with distance when operating with a single etalon peak at high power. Beam radii were measured by focusing the output beams onto the 7-razor knife-edge beam profiler (BeamMaster). The data points were fitted with the propagation function of a generic multi-mode beam in vacuum taken at $1/e^2$ [200] that is

$$w(z) = \sqrt{w_0^2 + \left(\frac{M^2\lambda}{\pi w_0}\right)^2 (z - z_0)^2}, \tag{4.5}$$

where w_0 is the beam waist radius at the focal point z_0. The Raman laser therefore propagated with $M^2 = 1.4$. Degradation of the fundamental beam quality from M^2 <1.5 to M^2 <2 was observed while SRS was occurring, as expected.

Typically, in intracavity Raman lasers systems the spatial modes degrade over the pump power [89] since oscillation of higher order transverse modes are favoured at higher pump power, but here we were not able to progress with an investigation of how the spatial modes evolved as we started seeing deterioration in the diamond coatings.

4.2.5 Polarization

Raman laser field polarization was measured with respect to the fundamental, by steering the output beams through a cube polarizer outside the cavity. Figure 4.23 shows the variation of the transmitted output power of the fundamental and Stokes-shifted beams with angle of rotation of the polarizer.

It can be seen that in the absence of the diamond the fundamental field polarisation produced the expected $\sim \sin^2$ behaviour (Malus law) and maintained, when the Raman laser was oscillating, the same orientation that was set by the intracavity birefringent filter at Brewster angle whereas the Stokes field was found rotated by $\sim 24^\circ$ with

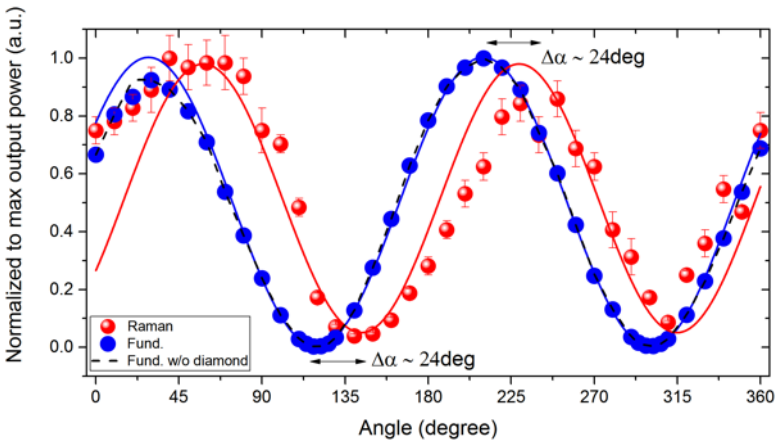

Figure 4.23: Normalized output power of the fundamental (blue) and Raman laser (red), transmitted bythe cube polarizer as it is rotated. The fundamental field polarization without the diamond (dashed curve) is fixed to the horizontal axis by the birefringent filter.

respect to the fundamental (it should be noted that the rotation scale of the polarizer was not calibrated such that 0° corresponded to the horizontal polarization). This difference can likely be attributed to the fact that whilst the diamond was orientated such that a <111> axis was parallel to the fundamental polarization, the residual birefringence, measured to be $\Delta n \sim 3 \cdot 10^{-6}$ (by ElementSix), constrained the Stokes-converted field to oscillate off-axis. Indeed, according to Jasbeer et al. [162], if the linear birefringent axes is not aligned to <111>, weak stress-induced birefringence fixes the Stokes field polarization to the local birefringence axes, preventing the gain from being maximized also when the fundamental field oscillates along the <111> axes. Other than birefringence, imperfections of the extinction ratio the Raman laser curve may be also attributed to alignment and sensitivity of the power meter, limited to ∼10 mW, whereas the fundamental wavelength was collected by an optical power meter with nW of sensitivity.

4.2.6 90°-rotated diamond Raman laser

Given the diamond crystal cut orientation and the geometry of the diamond mount (see Fig. 4.11), the possible directions of the <111> orientation are two: horizontal, and hence parallel to the pump field, giving the highest gain; or, when rotated by 90°

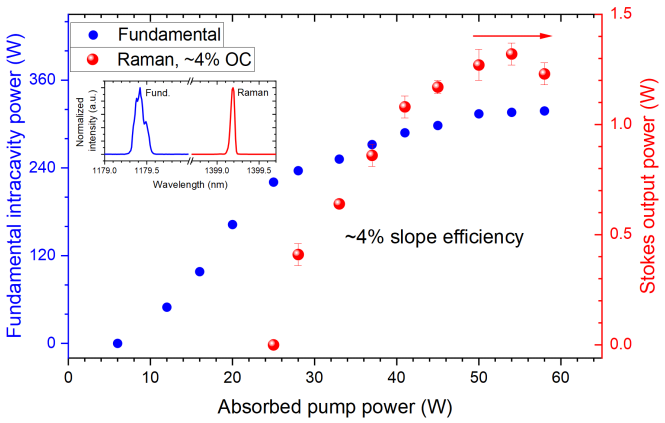

Figure 4.24: Power transfer characteristic of the diamond Raman laser after rotating the diamond by 90°. The inset shows the fundamental and Raman emission spectra at the highest power.

clock or anti-clockwise, <111> forms an angle of 35.3° with respect to the horizontal (or pump field) direction, which returns a lower gain. We turned the diamond by 90° around the beam propagation direction to characterise the effect on the Raman laser polarisation. The diamond mounting precluded rotation, hence we needed to demount it and rotate it manually. This might have tweaked the position of the diamond as well. At the time of this experiment, however, both the SDL sample and the diamond coatings started showing signs of deterioration, increasing the actual loss. We observed this as a significant variation in the power when we pump different areas of the crystal, owing to birefringence and degradation of the coating layers.

To allow a fair comparison with the previous diamond orientation measurements, we found the optimal diamond area by shifting its position along the horizontal and vertical axis. Once the Raman laser output power had been optimised, we carried out the power transfer of the Raman laser using the 50μm and 200μm etalons to provide single-peak oscillation with ~4% output coupling. The Raman laser power transfer, the fundamental intracavity power, and their spectra are reported in Fig. 4.24.

The 90°-rotated diamond Raman laser reached a maximum output power of 1.3 W, which is considerably less than in the previous experiment, and with much higher intracavity fundamental power at threshold. Within a standard deviation fluctuation of typically around 15%, the fundamental power likely rolled over, causing the Raman laser

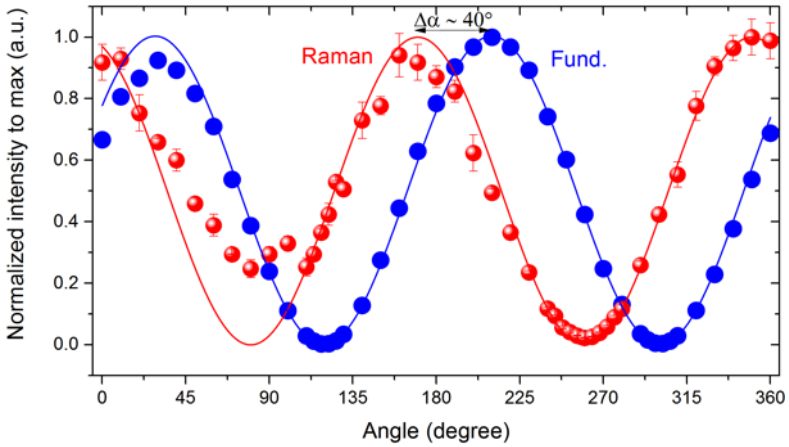

Figure 4.25: Fundamental and Raman laser polarization when the diamond was rotated by 90° around the beam direction. The solid curves are $\sim \sin^2 \alpha$ fits.

power to roll off too. As noted in Chapter 3, diamond can withstand a significant heat load during the Raman process with the cavity remaining unaffected. The calculated focal length of the thermal lens generated in the crystal when the Raman laser output power is over 1 W could be an order of magnitude greater than the cavity length itself. In fact, considering the thermal lens dioptric power as per Eq. 3.30 of Chapter 3, the focal length of the thermal lens is calculated to be +6 m for 1 W of output power, given 2000 W/mK thermal conductivity, 1.5×10^{-5} K^{-1} thermo-optic coefficient [137], and 41 μm Raman beam radius throughout the crystal length.

Given this diamond arrangement, we measured the Raman laser polarization compared to the fundamental, depicted in Fig. 4.25. Although it is not totally clear why the extinction ratio of the Raman laser was poor at 90°, the curve is quite clearly shifted by ~40° with respect to the fundamental, which remained unaffected by the new diamond alignment. With no birefringence, the Stokes polarization should be rotated by 19.4° and, if the birefringence contribution was the same, i.e. 24°, therefore the Stokes polarization was expected to be rotated by a total of 43.4°, which seems in good accordance to the shift observed (~40°). This presumably indicated that the former orientation of the diamond was configured for horizontal <111>, although birefringence hinders the laser performance.

It is worth noting there is some evidence from [162] that in high-Q cavities (i.e.

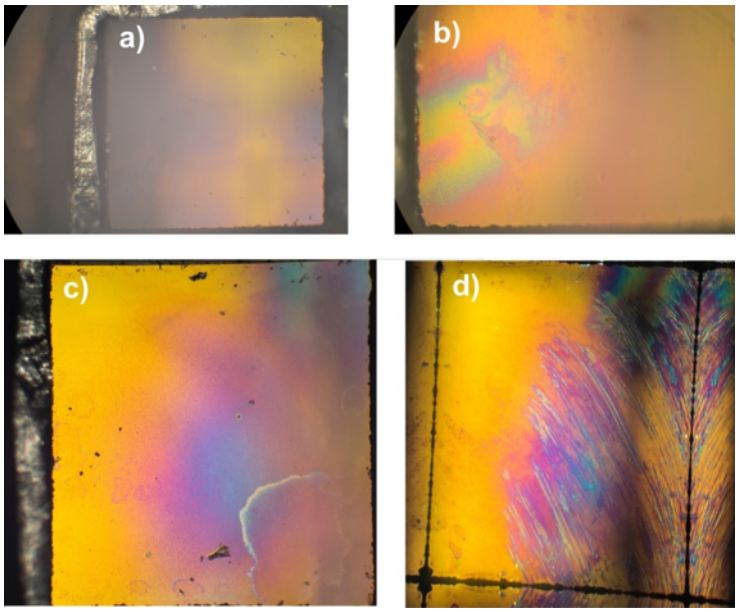

Figure 4.26: Photos of the diamond of the two end surfaces a) and c) after the Raman experiment. (b) and (d) are a close-up of (a) and (c) respectively.

quasi-CW or CW lasers) the best performance tends to track the birefringent axes, while in low-Q lasers (i.e. pulsed lasers) the highest performance tracks the gain. In this case the Raman scattering eigenmode vector (<111> in the diamond case) influences the Raman laser polarization [162]. In practice, not knowing the exact birefringence retardance map of the diamond, this Raman laser could be optimized by rotating the crystal until the retardance tracks the highest gain, hence the highest output power.

4.3 Conclusion

In this chapter we have demonstrated a continuous-wave SDL-pumped Raman laser operating in the lowest extreme of the eye-safe region. An 8-mm long diamond was used to down-convert the 1180-nm emission of an InGaAs-based SDL into the 1400 nm spectrum with a single Stokes shift. This is the longest wavelength achieved via intracavity Raman conversion of an SDL with a single conversion step. The Raman laser was wavelength-tuneable from 1373 to 1415 nm via rotation of a birefringent filter located in the SDL resonator. The Raman laser tuning range coincided with several

strong water vapour absorption lines, which was quite detrimental for the laser performance in a normal-humidity environment, exhibiting an irregular tuning curve. In future work an enclosed, dry-air cavity will be required to improve the laser performance. Nevertheless, output power in excess of 2 W was achieved at 1394 nm with ∼4% output coupling and spectral control of the fundamental wavelength via the insertion of etalons, enabling narrow-linewidth emission below 0.1 nm FWHM (instrument limited) and good beam quality ($M^2 = 1.4$) at high power. Although such system generally exhibited intensity fluctuations, these can be nevertheless dramatically reduced, for example, by implementing a temperature-stabilized thermoelectric cooling unit on the SDL and the Raman material.

Spectral filtering of the fundamental combining two different etalon plates in the fundamental cavity provided a deeper insight into the spectral broadening effect on the Raman laser performance in diamond. The fundamental spectrum was controlled by using 50-μm, 100-μm or 200-μm thick suprasil plates (alone and together in cascade), which made it possible to enhance the pump efficiency and increase the output power, limiting the spectral broadening that Raman materials with narrow gain bandwidth are inclined to.

The Raman laser field was rotated by $\sim 24^\circ$ with respect to the fundamental field, whose orientation was pinned by the birefringent filter set at Brewsters angle. Some residual birefringence in the diamond, induced by dislocations emerging from the CVD growth process, probably caused the Raman field to oscillate with a different orientation not parallel to the <111> direction. Both rotation of the diamond or polarization compensation in the Raman cavity with an intracavity waveplate could be implemented to reduce this retardance and improve the laser performance.

A tuneable SDL-pumped diamond Raman laser can be conceived in a stabilized, narrow-linewidth laser scheme to scan narrow lines of some absorption features in gases for molecular spectroscopy and gas sensing.

Our diamond Raman laser setup could be also tailored for a successive Stokes conversion step in cascade for emission in the 1.7 μm region, which is still of particular interest for gas detection and medical imaging applications (see next Chapter). To

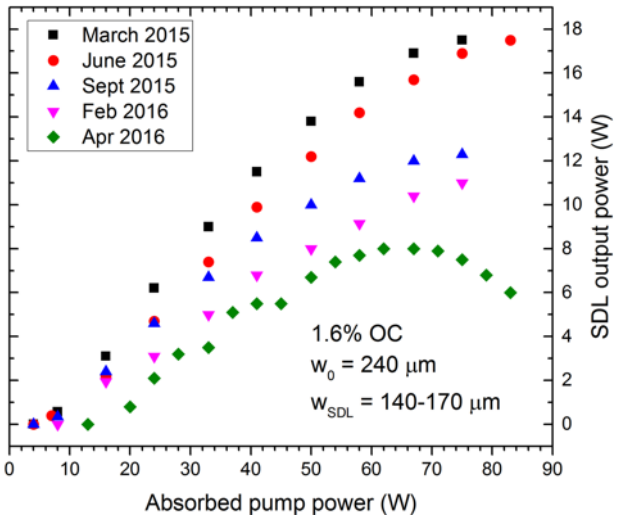

Figure 4.27: The power transfer of the SDL over twelve months before and after the diamond Raman laser experiment.

guarantee Raman laser emission up to 1.7 μm, however, it is still necessary to limit cavity losses to few percentages at each Stokes-shifted laser. Whilst high-reflectivity, broadband coating growth is fully accessible on fused-silica glass, at the time of the experiment coating technology was not yet at the point to ensure a growth of robust, broadband coatings on diamond for intracavity purposes where reflection losses below $\sim$0.5% are required.

The coatings of the diamond degraded over the course of the experiment such that it was difficult to target a working area and therefore we moved onto our experiments with KGW. Note that the diamond was cleaned less than the other optics (especially mirrors) because the cleaning process required removing the crystal from the cavity for immersion in an acetone bath. Swiping the surfaces with lens tissues and solvent could also have been deleterious. Therefore it is possible that the laser burnt some dust particles and accelerated the coating deterioration. When the experiment was finished, we removed the crystal and took some photos of the surfaces through the microscope in order to look over any damage (Fig. 4.26). The coatings seemed partially damaged, and it can also be seen that the surfaces present some scratches and coloured interference patterns in the areas where the laser was likely running through, suggesting that either the coating layers were slightly detaching from the substrate or they were simply dirty.

Further, the SDL material deteriorated in performance over a year. We regularly tested the sample in a 3-mirror cavity to check whether or not the laser was running optimally. Figure 4.27 shows the diminishment of the output power of the SDL taken at different times during the Raman experiment.

SDL emission towards 1180 nm is made possible thanks to higher concentration of indium and strain compensation due to high strain in the quantum wells. While strain compensation layers were included it is possible that this compromised the SDL lifetime, although this remain still unclear.

In the next chapter we address laser emission in the 1.7 μm region using a KGW crystal with a new SDL sample to efficiently generate three cascaded Stokes conversion wavelengths to cover the 1.3-1.7 μm range.

Chapter 5

1.7 μm cascaded third Stokes KGW Raman laser

To date, semiconductor disk lasers (SDLs) emitting directly at eye-safe wavelengths between 1.4 and 1.7 μm are mostly based on quaternary compounds of quantum wells (QWs) [6, 7, 201]. With the exception of dilute nitride InGaAs SDLs, these gain structures are adversely affected by a relatively large amount of defects at the interface and poor thermal conductivity when monolithically grown on the distributed Bragg reflector (DBR) [13]. The wafer fusion process is so far the optimal technique for assembling such mismatching materials and enables SDLs with multi-Watt output and high conversion efficiency [13,33]. This approach requires, however, two separate growth steps (for QWs and DBR) which makes the whole procedure more complicated than the manufacture of a conventional, monolithic SDL. Other functional, though less compact, alternatives can be integrated into SDLs to mitigate this challenge. One of these is to implement intracavity nonlinear crystals for Raman down-conversion of well-established InGaAs-based SDLs, allowing the fundamental to be Stokes-shifted in a cascading process towards longer wavelengths.

Cascaded Raman conversion is a relatively simple process that does not require a sophisticated cavity configuration. Typically, the Raman gain is only weakly wavelength-dependent, therefore, as long as the cavity is equipped with appropriately broadband

coatings, the Raman laser threshold depends on the pump intensity. The first observation of a cascaded Raman laser in a SDL was reported in 2011 by D. Parrotta et al. [35]. They utilised an intracavity KGW crystal to Raman shift by 767 cm^{-1} the 1040-nm fundamental field of the SDL to the 1140 nm region. Incidentally, they detected a second Stokes emission laser line near 1160 nm, because, for this particular crystal orientation, there exists a peak in the Raman gain spectrum at 84 cm^{-1} and the coatings on the optics (i.e. KGW and mirrors) were spectrally broad enough to allow oscillation of a second Raman laser line pumped by the 1140 nm field.

Different Raman materials have been used to access wavelengths longer than 1.4 μm. For instance, in solid-state laser systems, the longest wavelength via a single Stokes conversion was achieved by pumping a diamond with a pulsed 1.34-μm Nd:YAP laser in an external cavity to reach 1.63 μm [202]. Lux et al. generated a second Stokes order at 1.48 μm in an external diamond cavity for single longitudinal mode operation towards potential application in water vapour sensing [153]. Following our report of a 1.4 μm diamond Raman laser presented in the previous chapter (and also published in ref. [90]), it would be possible to use diamond to access the 1.7 μm region via a second Stokes laser. The main challenge we encountered with this material at the time of writing was to find a coatings manufacturer willing to guarantee a broadband AR coating on diamond for intracavity use. Typically, coatings manufacturers can still customize AR coatings for such a broad wavelength range (1-1.7 μm) and low reflection, but the deposition of reliable multilayer dielectric coatings on diamond was limited to reflection above 1%. An efficient intracavity Raman laser requires that the total cavity loss is below a few percent. With R >1% per end facet, the diamond would contribute at least 4% reflection loss plus the absorption loss per round-trip, with which both the SDL and the Raman laser would be unable to reach threshold. Conversely, AR coatings with $R < 0.5\%$ are routinely achieved on KGW for this wavelength range as the surface chemistry favours better adhesion (diamond is more chemically stable). The disadvantage is that KGW has a smaller Raman shift than diamond - the longest is 901 cm^{-1} [203] - and therefore 3 Stokes shifts are required to reach 1.7 μm from a fundamental wavelength of 1180 nm.

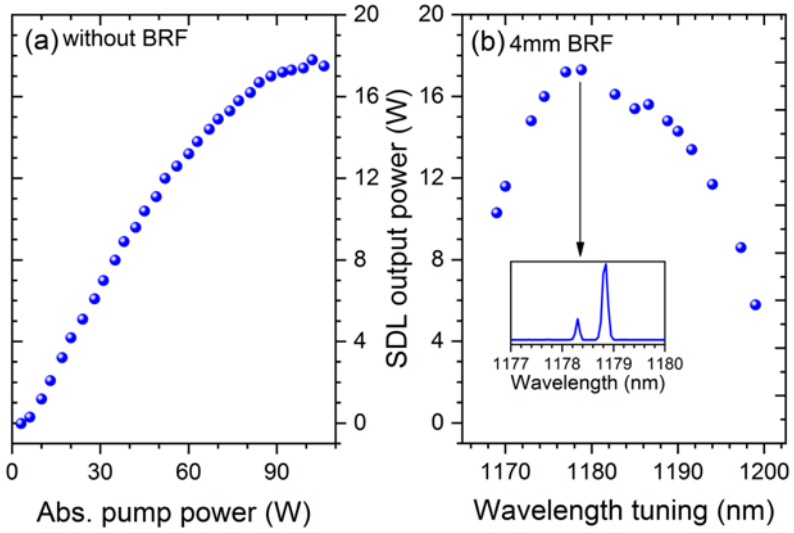

Figure 5.1: (a) Power transfer of the InGaAs SDL structure with 1.6% output coupling. (b) Tuning curve of the SDL at the highest pump power obtained by the rotation of the birefringent filter (BRF) with 1.6% output coupling. Inset: emission spectrum measured at the highest output power.

In this chapter we show, with some results, discussion and analysis, cascaded Stokes shifts in a SDL-pumped KGW Raman laser to reach laser wavelength operation up to 1.7 μm, with simultaneous oscillation of the lower Stokes orders in the 1.3- and 1.5-μm region.

5.1 Characterization of the InGaAs SDL with a plane-parallel heatspreader

For the cascaded Raman laser experiment we utilized an SDL chip from the same wafer as presented in the previous chapter and reported in [14, 193]. The SDL consisted of 10 strain-compensated, equally-spaced 7-nm thick InGaAs quantum wells for tuneable laser emission centred at ∼1180 nm. Unlike the previous sample, where a wedged diamond heatspreader was used, the gain structure was bonded to an uncoated plan-parallel 500-μm thick diamond heatspreader and clamped to the brass mount for water cooling down to 10°C. (In our laboratory, temperatures below this usually result in condensation of water on the mount.) Capillary-bonded onto the intracavity side of

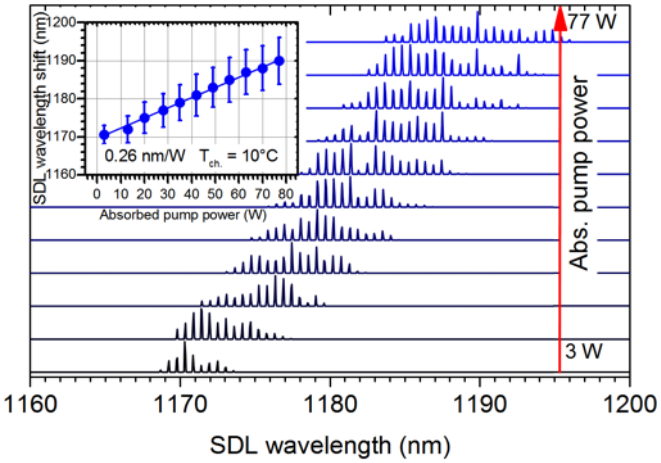

Figure 5.2: The SDL emission spectrum as a function of the pump power from 3 to 77 W of absorbed diode pump power indicated by the vertical red arrow. Inset: SDL wavelength shift versus pump power; the vertical bars indicate the maximum wavelength extension of each spectrum.

the gain structure, the flat parallel diamond surfaces (<0.15 mrad) provide an etalon effect with free spectral range of ∼0.57 nm. By this, plus some additional intracavity filtering as explained later, both the SDL and Raman laser can oscillate with narrow linewidth. Due to the presence of the diamond bonded on the intracavity side, the 80% of the diode pump beam is being absorbed by the SDL gain active structure upon reflection.

We first tested the SDL in a three-mirror cavity, consisting of the DBR as a plane end mirror, a folding highly reflective (HR) mirror (AOI< 5°) with 200 mm radius of curvature and R>99.9% from 1160-1190 nm, and a plane end mirror with 1.6% output coupling (OC). The mirror-mirror distances were chosen to be SDL-HR = 110 mm and HR-OC = 200 mm to provide a 100-μm cavity mode radius on the SDL chip surface and to allow insertion of a birefringent filter mount compatible with the cavity size. We pumped the SDL gain chip with a commercial fibre-coupled diode laser at 808 nm, whose external optics collimated and focused the beam to a spot radius of ∼200 μm on the surface of the sample with an angle of incidence of ∼20°, in the same arrangement as used for the diamond work presented in Chapter 4. A bigger pump spot size would promote high output power at the cost of multi transverse mode operation [71].

The free-running SDL reached threshold at 3 W of absorbed pump power and operated with maximum output power of 17.8 W when the absorbed pump was 102 W and an output coupler of 1.6% transmission was used [Fig. 5.1(a)]. Thermal rollover of the output power was observed above above 102 W of absorbed pump power. "Absorbed pump power" here refers to the net of the input pump power that reaches the gain structure and it was calculated considering the sum of the Fresnel equation at the air-diamond and diamond-semiconductor interfaces at AOI - 20°, calculated to be ∼80%. Note that the total internal loss may affect the rollover point by a few Watts of pump power and therefore during the Raman experiment the rollover pump power may vary. Also, tweaking the distance of the focusing lens could affect the shape and dimension of the pump size as well, to which the SDL is quite sensitive [71].

The tuning curve depicted in Fig. 5.1(b) was carried out at the highest pump power, with 1.6% OC, via the in-plane rotation of an intracavity 4-mm thick birefringent filter. The laser tuned from 1170 to 1200 nm, limited by the free spectral range of the birefringent filter, and operates with maximum power of 17.3 W at around 1179 nm [Fig. 5.1(a)] and 33% slope efficiency [Figure 5.1(b)], hence with a minimal amount of loss when the BRF was inserted. Although the BRF alone enabled narrow emission (<1 nm) the SDL can exhibit a broader spectrum during Raman laser oscillation. This SDL sample still showed very similar performance to that reported in the previous chapter and in [14, 193].

In Fig. 5.2 is reported the wavelength shift of the free-running spectrum with increasing pump power, using an output coupler with 0.8% transmission. While pumping from the threshold to the highest output power, the SDL spectrum exhibited a relative large bandwidth (∼10 nm) where the mean wavelength shifted from 1170 to 1190 nm at a rate of a 0.26 nm/W. The comb-shaped emission spectrum is due to the etalon filter modulation imposed by the flat parallel diamond heat-spreader. The peak-to-peak separation was 0.56 nm, in accordance with the calculated free spectral range at 1180 nm of the 500-μm thick diamond. Although the free spectral range of the diamond limits continuous tuning to a particular wavelength for gas spectroscopy, fine wavelength tuning can be also achieved, for instance, by changing the SDL temperature.

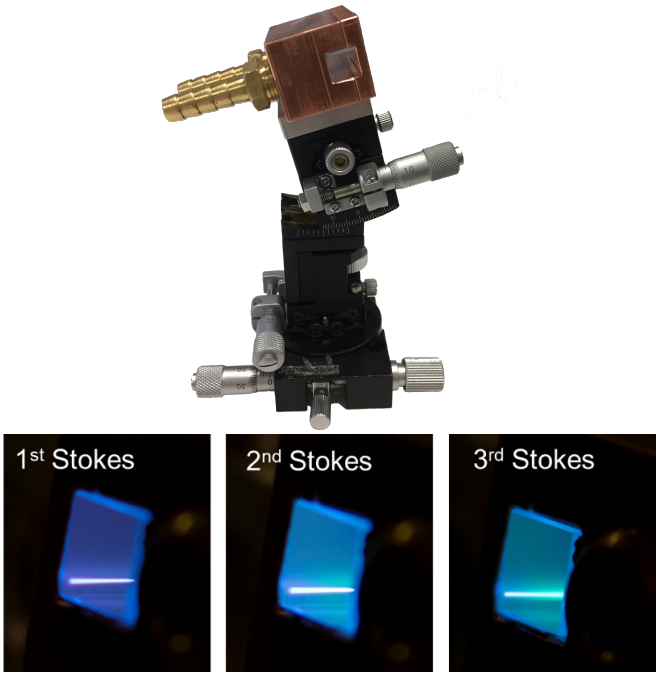

Figure 5.3: (*Top*) Photo of KGW copper mount placed on a translation/rotation stage. (*Bottom*) Visual difference of the KGW crystal photoluminescence during first Stokes and cascaded Raman laser oscillation.

For the analysis of some of the Raman laser results presented in the next sections, we utilised Caird analysis [195] for the SDL in order to track the sample performance over each embodiment of the experiment. During the 1st Stokes experiment we estimated a round-trip loss and internal efficiency of around 1.2% and 50%, respectively; during the cascaded Raman experiment the SDL round-trip loss had increased to $1.5 \pm 0.1\%$, with $34 \pm 3\%$ of internal conversion efficiency.

5.2 KGW for cascaded Raman laser

In this work we utilized a 7x7x30 mm^3 commercial potassium gadolinium tungstate crystal, $KGd(WO_4)_2$ (or KGW), as the Raman gain medium, cut for propagation along the N_p axis and oriented to access the 901 cm^{-1} Raman shift via excitation along the N_m axis, with a corresponding gain coefficient $g_0 = 3$ cm/GW at 1064 nm [204]. Raman gain at longer laser wavelengths can be estimated via $g(\lambda) = g_0 \cdot 1064\ \text{nm}/\lambda$ [144], where

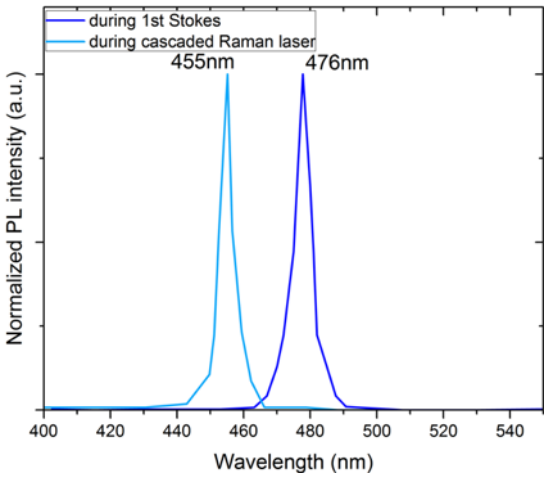

Figure 5.4: Photoluminescence spectra of the KGW in the visible region during 1st Stokes and cascaded Raman laser oscillation (digitized image).

λ is the wavelength of interest. To reduce the intracavity loss, coatings were customized for high transmission at both end faces: R<0.5% from 1160 to 1750 nm (LaserOptik). Like in diamond, to allow heat conduction to the mount, the crystal was wrapped in a 125μm-thick indium foil and clamped into a copper mount.

During the Raman experiment we have observed emission in the blue with some degree of brightness depending on the intensity of the Raman laser, in the presence of SRS. Figure 5.3 shows the photos of the KGW photoluminescence when fluorescence colour slightly changes during first, second, and third Stokes laser oscillation.

This phenomenon can be associated with photo-luminescence induced by up conversion processes quite common in KGW [203, 205, 206]. We collected the photoluminescence during Raman laser oscillation by fibre-coupling the output to an optical spectrum analyser with <1 nm resolution. Figure 5.4 shows two spectra taken when the instrument was collecting the output power transmitted by the output coupler during 1^{st} Stokes and cascaded Raman laser oscillation.

During first Stokes laser oscillation at 1320 nm, the blue luminescence was centred at about 476 nm and it was shifted to 455 nm when the Raman laser reached the threshold at the second Stokes wavelength, 1500 nm, and it remained unchanged after oscillation at the third Stokes wavelength, 1730 nm. The line at about 476 nm (~7 nm FWHM) was first detected in a study of an 808 nm diode-pumped Nd:KGW Raman

laser for Stokes emission at 1180 nm [203], in which the authors attributed the 476 nm emission to the absorption transition between the excited states of Nd ions due to the fundamental photons. This optical property has been investigated in a pure KGW crystal and is also commonly found in YVO_4 crystals [207]. Consequently, the study was extended also to $BaWO_4$ and Nd:$GdVO_4$ [205], where they assigned the origin of the mechanism to Tm^{3+} impurities in vanadate and tungstate systems. Therefore it would be possible that the luminescent line at 455 nm was generated by some up-conversion process between higher energy levels of Tm impurities in KGW during cascaded SRS although it is not clear the mechanism. An investigation of such phenomena is left for a future study. Whatever the nature of this mechanism, this generates cavity loss and thermal loading. In the next paragraph we attempted to measure the optical absorption loss of the KGW at 1180 nm.

5.2.1 KGW absorption at 1180 and 1320 nm

Measurement of the optical absorption coefficient was attempted following the Caird analysis method [195]. The KGW was inserted into a three-mirror cavity of the SDL and the power transfer was measured with a set of output coupler transmissions. Assuming that the internal conversion efficiency (η_{SDL}) of the SDL is an intrinsic property of the gain mirror, the efficiency was first estimated from the Caird analysis without the KGW and then used as an input parameter for the fit with KGW. Figure 5.5 shows both the Caird analysis and the power transfers. The contribution loss of the KGW is therefore the difference between the SDL loss with and without the KGW. This was estimated to be 0.7% per round-trip and counts both the loss due to absorption and reflection loss of the coatings. Separately, the reflection from each crystal surface was measured at a small angle of incidence; this was measured to be 0.015% and 0.022% for a total of 0.074% per round-trip, which is lower than that calculated by the manufacturer. Therefore we surmise that the round-trip loss due to optical absorption is L = (0.6 ± 0.4)% which returns, by $L = 1 - \exp(-2\alpha l)$, an absorption coefficient of $\alpha = (0.001 \pm 0.0008)$ cm^{-1}.

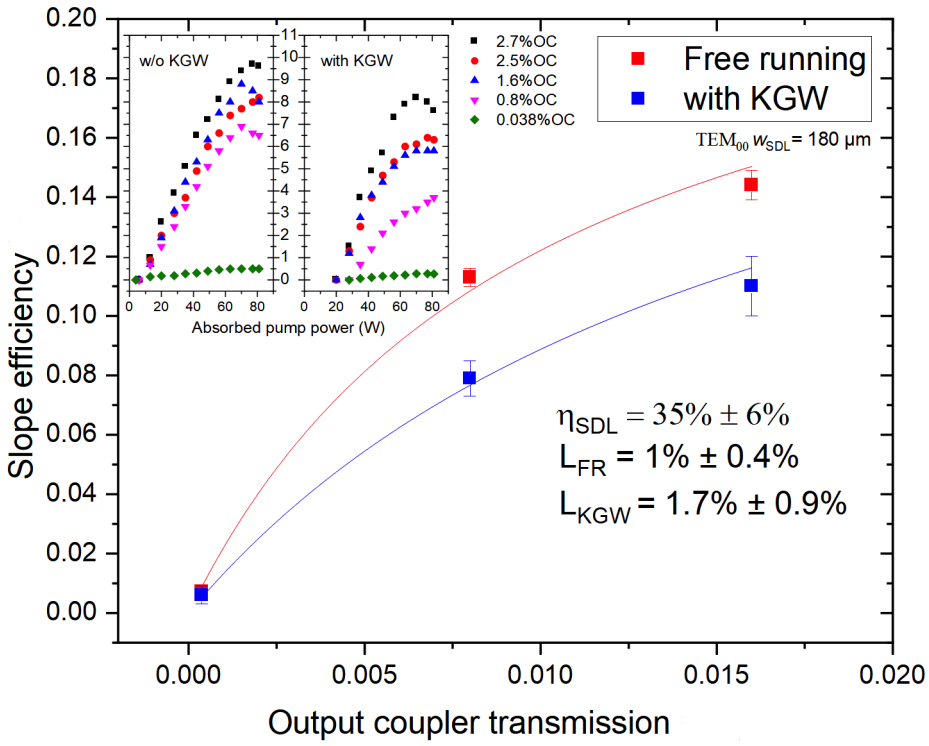

Figure 5.5: Caird analysis of a three-mirror cavity SDL, with and without intracavity KGW, fitted with the curve of Eq. 4.1. *Insets*: output power (W), y axis, versus absorbed pump power with a range of output couplers. The vertical error bars origin from the slope efficiency fit calculation.

5.3 Cascaded Raman laser setup with KGW

The laser cavity design, similar to that used for the diamond Raman laser experiment, is shown in Fig. 5.6. This consisted of a two partially-shared four-mirror cavities designed for laser oscillation at the fundamental at 1.18 μm and the cascaded Raman wavelengths at approximately 1.32, 1.50 and 1.73 μm. The concave mirrors, namely M2, M3 and M4, were coated for high reflectivity for all laser wavelengths (R>99.95%, 1150-1770 nm) and define the fundamental cavity. The mirror distances were chosen to provide a TEM_{00} 140 μm beam radius on the SDL chip and a 41 μm beam focus in the centre of the KGW for a low Raman laser threshold. Such a cavity mode mismatch

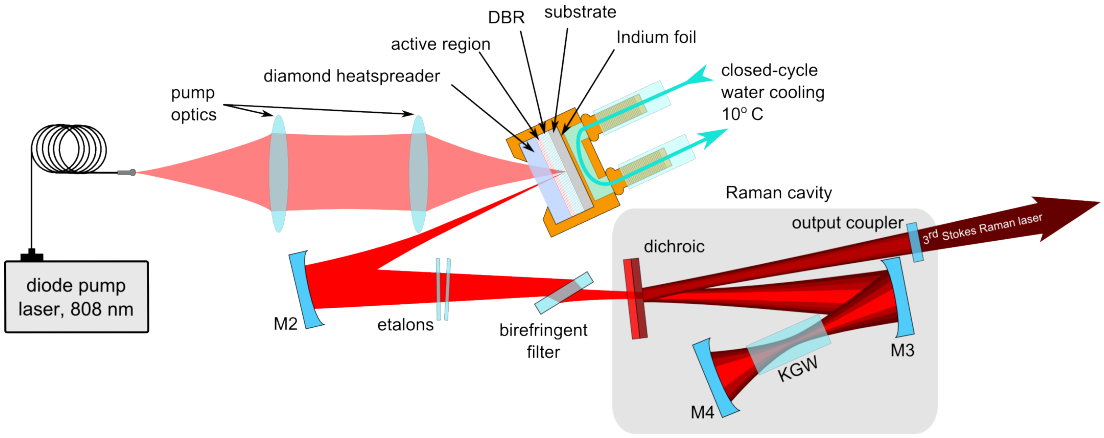

Figure 5.6: Scheme of the SDL-pumped KGW Raman laser. HR: high reflector; OC: output coupler; DBR: distributed Bragg reflector; HS: heatspreader.

at the SDL gain mirror is compensated with operation at higher M2 and higher output power. Intracavity-pumped Raman lasers do not require pumping with a TEM_{00} beam as they can still be optimised for high beam quality and high power owing to beam clean-up effect [148] and high fundamental intracavity power. For a high effective Raman gain, instead, a good overlap in the KGW for the Raman and fundamental beams is recommended [145]. To achieve this, a flat dichroic mirror (DM) was placed in the longest arm (M2-M3) in order to steer, with a small angle (AOI$\sim$2°), the Raman beam to the output coupler (OC). The DM-OC distance can therefore be adjusted to change the beam waist size in the crystal and hence provide mode matching with the fundamental.

Since the dichroic mirror was highly reflective at all Raman wavelengths (R > 99.9%) and highly transmissive at the fundamental (T > 99.9%), the end output coupler could be swapped to switch the Raman laser to the desired Stokes wavelength. A set of output couplers were available: two mirrors with 0.5% and 2.2% OC at 1320 nm for the first Stokes; 1% OC at 1280-1520 nm for the first and second Stokes together; and 1% OC at 1660-1770 nm for the third Stokes with high reflectivity in the 1310-1430 nm range.

A single-plate 4-mm thick birefringent filter (BRF) was placed at Brewsters angle in the longest arm outside the Raman cavity to pin the fundamental field polarization

parallel to the N_m optical axis of the KGW, and enable wavelength tuning of the fundamental and hence the Raman wavelength. The plane-parallel intracavity diamond heatspreader provides some filtering, but the SDL has broad gain, especially in the case of high-power operation, which favours multi longitudinal and transverse mode oscillation. This produces, in the case of a plan-parallel heatspreader, many etalon peaks (see Fig. 5.1) that need to be reduced to a single one if the laser is tailored for a single longitudinal mode or, at least, a narrow linewidth. The large thickness of the BRF itself is sufficient to modulate the spectrum to a single or few etalon peaks when inserted in a three-mirror cavity, but the spectrum enlarges significantly when the laser oscillates within the four-mirror cavity and the Raman crystal is included, and therefore further intracavity filtering is required.

A practical solution is to insert a single Fabry-Perot etalon filter with a spectral range larger than the fundamental spectral width (typically some nm) as we employed for the diamond case presented in the previous Chapter. For example, a single 50-μm thick etalon plate (etalon A in Fig. 5.7) provides a free spectral range of 9.52 nm, which is smaller than the SDL free-running spectrum and hence would provide a single or two etalon peaks. Also, when oscillation with a single etalon peak is obtained, fluctuations due to mechanical instability of the rest of the optics and the etalon itself sometimes caused the laser to oscillate with other diamond etalon peaks. Therefore single peak operation is not guaranteed throughout the entire period of the experiment, typically a few hours or more. Alternatively, inserting two etalons with different thicknesses aids the laser in oscillating stably with a single narrow peak. However, the use of two etalons makes the tuning a more complicated task, since the etalons need to be tilted accordingly. A multi-stage birefringent filter plate would achieve the same effect with a single optic, in which the thinnest plate provides large tuning with a very narrow linewidth defined by the thickest plate. (We attempted to insert a three-stage BRF, having a stack of 1, 3 and 6-mm thick plates, but the geometry of the cavity and size of the multi-stage BRF mount strongly limited the beam to pass through the centre of the aperture in a such way that we chose to continue the experiments with the single BRF along with etalon plates.) All cavity parameters for all wavelengths are summarized in

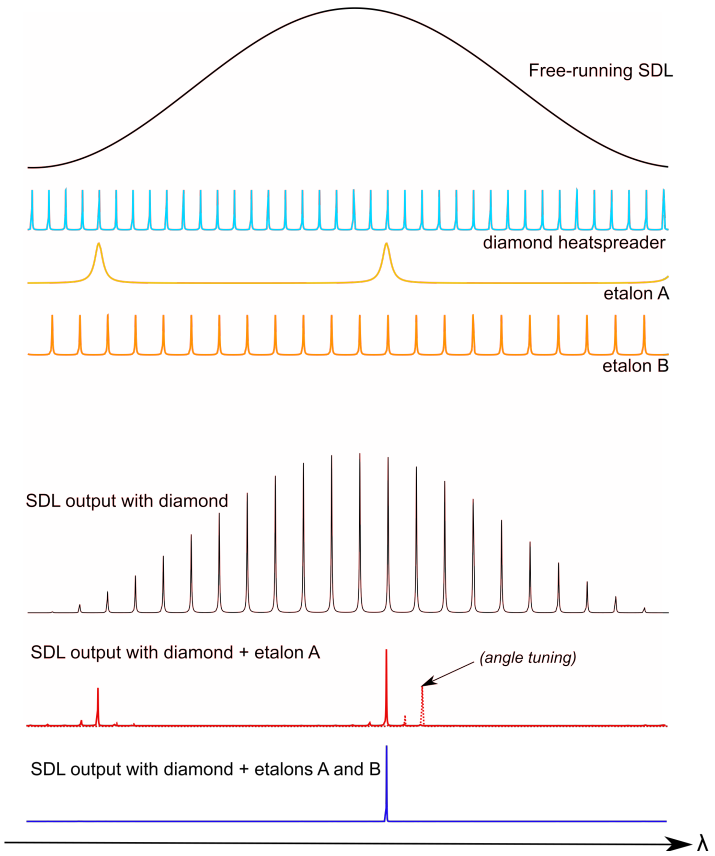

Figure 5.7: Sketch of the single etalon peak selection using two etalon filters. Angle tuning is achieved by slightly tilting the angle of incidence of the etalon.

Table 1.

It should be noted that the cavity modes are quite dependent on the position of the last curved mirror, M4, which was clamped on a translational stage with a range of 5 mm. Figure 4.7 shows the dependency of the cavity mode size with respect to the distance of the M4 mirror from the end of the KGW together with the consequent variation of the fundamental beam propagation inside the KGW. It can be seen that, tweaking the M4-KGW distance by about 1 mm from its initial position (42 mm), the fundamental cavity mode varies from 130 to 150 μm, and it becomes larger 200 μm when M4-KGW = 44 mm. This has to be taken into consideration when thermal effects are considerable during Raman laser oscillation and that the distances need to

Table 5.1: Fundamental and Raman cavity parameters.

Fundamental cavity (1.18 μm)		Raman laser cavity (1.32-1.73 μm)	
Mirror-mirror	Length (mm)	Mirror-mirror	Length (mm)
SDL-M2	110	OC-DM-M3	333
M2-M3	450	M3-KGW	49
M3-KGW	49	KGW-M4	42
KGW-M4	42	-	-
TEM$_{00}$ waist radius	41 μm	-	-
TEM$_{00}$ cavity mode radius	150 μm	-	-

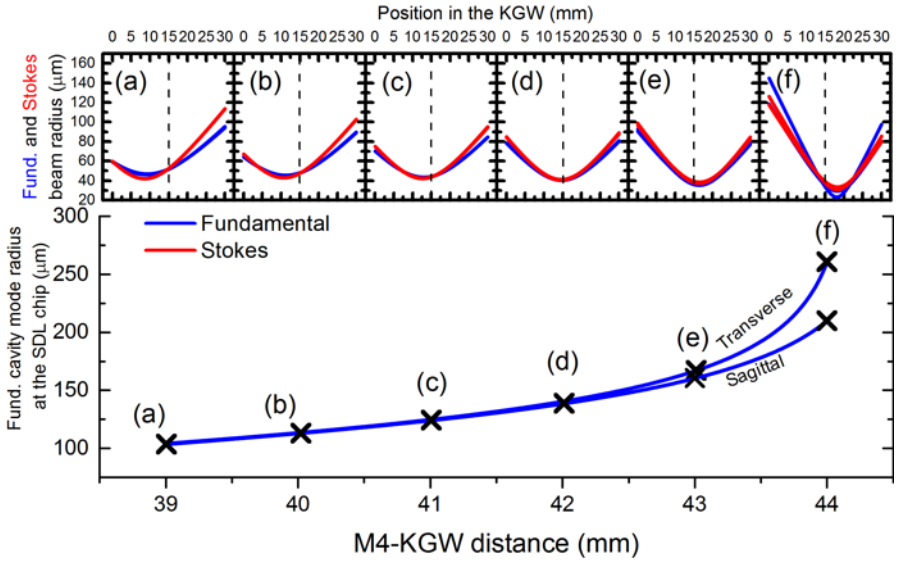

Figure 5.8: Bottom: variation of the fundamental cavity mode radius on the SDL surface. Top: fundamental and Stokes beam propagation inside the KGW at some M4-KGW distances.

be adjusted again if one wants to set the cavity mode back to the cold cavity mode size. This will be discussed further in the next section.

5.4 Raman shift at 200 cm^{-1}

The purpose of this work is to convert the SDL to longer wavelengths exploiting the largest 901 cm^{-1} Raman shift of KGW, which is provided by the vibration of the WO_4 ions tetrahedra [187]. While this is the dominant Stokes shift, it is not the only one to be excited during p[mm]p excitation. In fact, the complex structure of tungstate

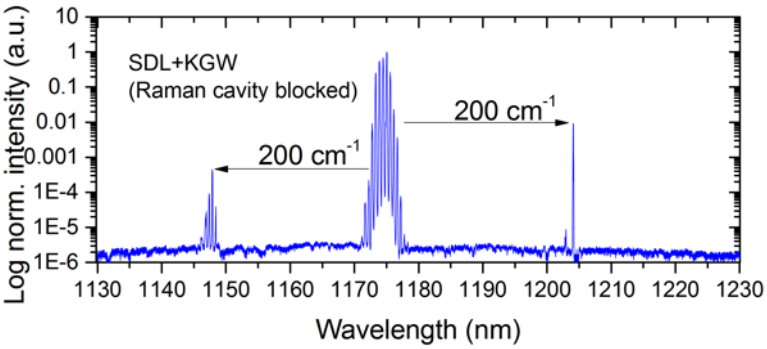

Figure 5.9: Emission spectrum of the SDL with an intracavity KGW crystal.

crystals characterizes KGW with other Raman features below 901 cm^{-1}. To identify any other competing Raman shift accessible within the stopband of the SDL DBR reflectivity, the SDL spectrum was recorded during oscillation in the four-mirror cavity including the KGW within the 1130-1230 nm range. We blocked the Raman cavity to prevent Raman laser oscillation above 1320 nm from any other other kind of cross cascading anti-Stokes shift in the 1180 nm region. Figure 5.9 illustrates the Raman shift of the SDL spectrum recorded at high pump power.

The spectrum is characterized with a high-intensity laser emission at ∼1175 nm, ∼5 nm broad, and two other main peaks at ∼1145 and ∼1205 nm, equally spaced by 200 cm^{-1} with respect to the fundamental peak. It is quite likely that these Stokes and anti-Stokes shifts are in accord with the Gd-O vibration in KGW as investigated in [187] and observed in [188]. Raman laser emission at 1145 and 1205 nm however was not highly repeatable as it was very sensitive to cavity alignment, but it may compete with the higher 901 cm^{-1} Stokes modes during cascaded Raman laser.

5.5 Anti-Stokes laser (1060 nm)

The Raman cavity was first equipped with a broadband HR (R>99.95% 1150-1770 nm) to have quick access to all Raman wavelengths. Figure 5.10 shows the spectrum of the Raman laser at high pump power through the leakage of the HR mirror gathered by a fibre-coupled optical spectrum analyser (OSA).

The fundamental wavelength of the SDL was Stokes-shifted to the longest 1732 nm

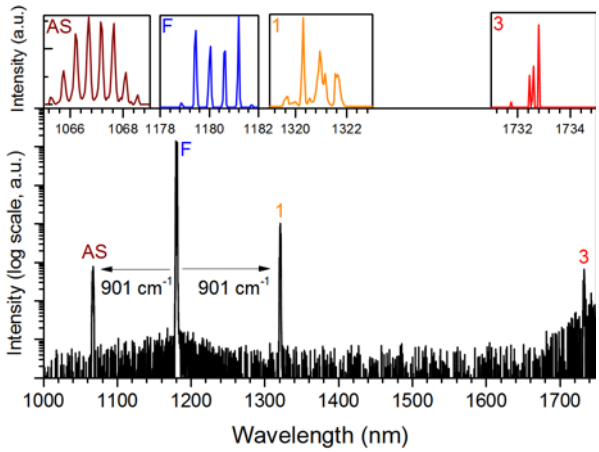

Figure 5.10: Emission spectrum of the SDL-pumped Raman laser for 92 W of absorbed diode pump power. AS, anti-Stokes; F, fundamental; 1 and 3 first and third Stokes laser. Top insets: 0.05 nm resolution; bottom: 0.2 nm resolution.

region and anti-Stokes shifted to around 1067 nm. Incidentally, generation at 1066 nm was made possible by the slight off-axis alignment of the Raman cavity to phase-match the first- to the anti-Stokes photons and the high-intracavity power level of this system. The anti-Stokes laser reached threshold at 28 W of absorbed diode pump power; just a few Watts more beyond the first Stokes threshold. Unfortunately, the actual reflection loss below the fundamental wavelength was unknown and we were not equipped with adequate filters to discriminate the anti-Stokes laser from the others. Also, the limited fine adjustment of the rotational stage of the KGW mount limited direct control of the anti-Stokes and any further optimisation. This also limited to optimize the intensity at the second-Stokes wavelength in the optical spectrum analyzer, as presumed to oscillate at 1500 nm thanks to the presence of the first- and the third-Stokes order.

However, we believe there are other two main factors that impede us from detecting this signal. First, the high-reflectivity of the mirrors at 1500 nm was too high to make the signal detectable; in fact we measured the transmission to be $(4.1 \pm 0.5) \times 10^{-7}$ at 1500 nm and $(9.6 \pm 0.9) \times 10^{-6}$ at 1320 nm. A discrepancy of a factor of $\sim$20 probably made the first-Stokes signal much more evident in the optical spectrum analyzer, and also the collection system was mostly optimized for the anti-Stokes wavelength as the second-Stokes component was generally of lower intensity than the other Stokes orders

as shown later in the next sections. Another possibility to take into account is that, according to the cascaded model of Williams et al. [208], the intracavity field of the second Stokes order is expected to have low intensity compared to the first order to allow first-Stokes oscillation. However, that model accounts for the specific case of extra-cavity setups.

Nevertheless, we report, for the first time to our knowledge, the first observation of a continuous-wave anti-Stokes laser in a SDL.

5.6 SDL-pumped KGW for 1320 nm

5.6.1 Broad emission

The HR was replaced with an output coupler for the first Stokes in the ∼1300-1340 nm range with 2.2% transmission. Figures 5.11 shows the power transfer of the first Stokes. The Raman laser emitted up to 6.1 W at 1320 nm for an absorbed pump power higher than 84 W. The Raman laser threshold was attained when the intracavity power was 300 ± 70 W, above which the output power increased with nearly 8% slope efficiency until 70 W, increasing to 14% from 70 to 80 W, above which the Raman laser remained unchanged. At the same time, the fundamental intracavity power nearly clamped above 70 W of pump power and it rolled over at 100 W. The non-regular slope efficiency can be attributed to the interplay between thermal effects and spectral and spatial mode evolution over the diode pump power.

Figure 5.12 shows typical multi-longitudinal laser mode spectra taken at different diode pump power. It can be seen that both the fundamental and the Stokes-shifted spectrum enlarged from a single narrow etalon peak, near the threshold to about 4-nm wide spectrum at the maximum pump power. The development towards broad emission can be mostly attributed to the low ratio of the cavity mode to pump size and the high-power pump regime of the diode on the SDL and in the KGW, influencing the Raman conversion efficiency. At the same time, the relative Raman gain lineshape of the KGW (see dashed black curve in fig. 4.9) is large enough to encompass nearly all fundamental longitudinal modes and thus maximize the gain.

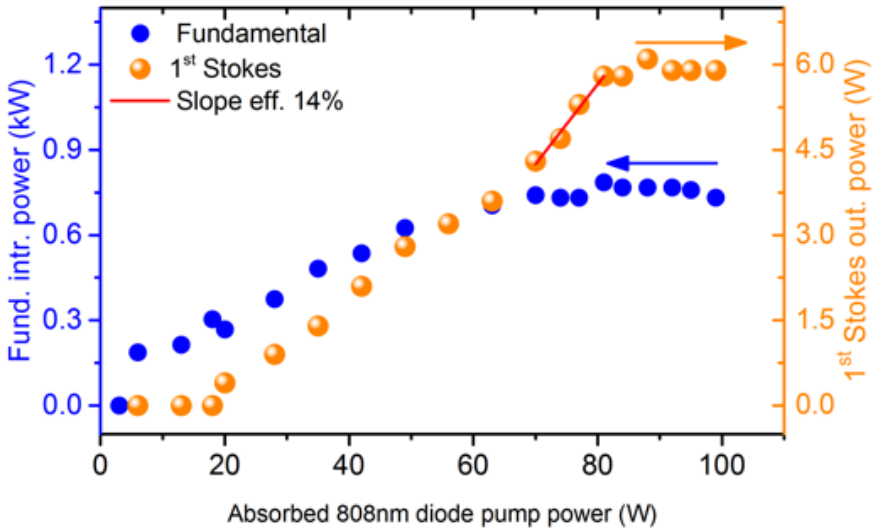

Figure 5.11: Power transfer of the first Stokes Raman laser and the fundamental intracavity power.

The beam quality factors (M^2) of the lasers were measured at 4 W of output power (around 70 W absorbed diode pump power) to enable the measurements in such a way that the passive thermal effects did not cause the laser to fluctuate significantly during the M^2 experiment. First, the fundamental beam propagated with $M^2 = 3 \times 2.5$, (horizontal)×(vertical), when the Raman cavity output coupler was misaligned to impede SRS generation at ∼70 W of absorbed pump power. Once we had aligned the output coupler to allow Raman laser oscillation at 4 W output power, the fundamental M^2 degraded to 5×3. Deterioration of the fundamental was automatically cleaned up by the Raman laser process itself [148], in which the Stokes beam quality was improved to 2.7×1.5.

Unlike the diamond Raman laser case, the phonon dispersion at 901 cm^{-1} is larger, 5.9 cm^{-1} FWHM, and therefore an optimal spectral overlap between the pump spectrum and the Raman gain linewidth can be achieved with no spectral narrowing with etalons as long as the fundamental is narrower than the Raman gain bandwidth [145, 146]. Indeed, the Raman linewidth is larger than the free spectral range of the heatspreader (4 cm^{-1}), as shown earlier in Fig. 5.12, and gives an indication that high efficiency can be managed without spectral narrowing.

In an ideal intracavity Raman laser, the intracavity power is clamped above the

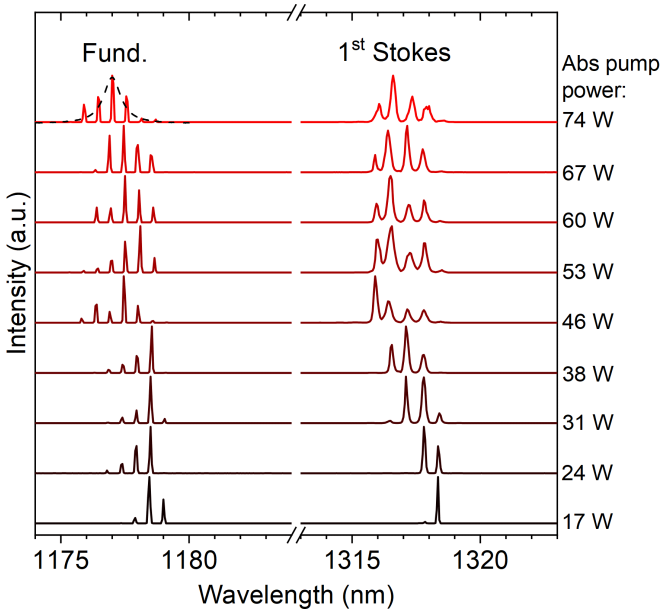

Figure 5.12: Development of the fundamental and first Stokes laser emission spectrum from near the threshold to the maximum diode pump power. The dashed line represents the virtual, Lorentzian-like, KGW Raman gain linewidth at 1180 nm.

Raman laser threshold and the slope efficiency is maximized. In some cases, however, the complex behaviour of the longitudinal and transverse modes impedes the intracavity fundamental energy from being efficiently converted for Raman laser emission, thus leading to an irregular increase of the intracavity power [145]. In the ideal case, the maximum slope efficiency for the SDL case is proportional to the quantum defect (λ_p/λ_1), the internal conversion efficiency within the SDL gain medium (η_{SDL}), and the relative output coupling [89, 145]:

$$\eta_{ideal} = \frac{T_{oc}}{T_{oc} + L_R} \frac{\lambda_p}{\lambda_1} \eta_{SDL} = 16\% \tag{5.1}$$

where $T_{oc} = 2.2\%$ is the output coupling at $\lambda_1 = 1320$ nm, $\lambda_p = 808$ nm is the diode pump and first Stokes wavelength, $\eta_{SDL} = 50\%$ is the SDL internal efficiency, and $L_R = 2.1\%$ is the estimation of the round-trip loss associated with the Raman cavity, which is calculated by the sum of ~0.7% of round-trip absorption loss in the KGW (absorption coefficient 0.001 cm^{-1} at 1180 nm, but it can be smaller at longer wavelengths), 1.2% given by the round-trip reflection loss of the facets coatings (0.3% at 1320 nm), and

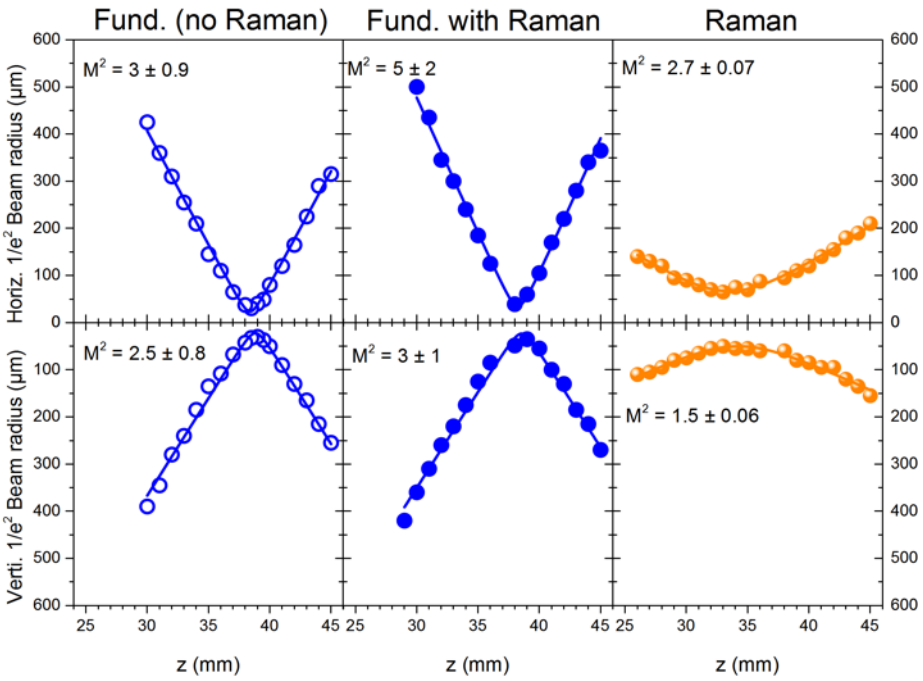

Figure 5.13: Laser beam propagation for a 70 W absorbed pump power (4 W Raman laser output power).

the remaining 0.2% is due to the leakage through the HRs and the dichroic mirror. In the region where the intracavity power was clamped (∼60-100W of pump power), the slope efficiency was 14%, higher than the overall slope efficiency (∼9%) and close to the ideal value estimated by Eq. 5.1.

5.6.2 Thermal lensing considerations

In a region where fundamental power was clamped, the Raman laser output power eventually rolled over at ∼6 W. It is likely that the Raman rollover was caused by thermal lens. Similar behaviour was observed in another analogue KGW Raman laser experiment [188]. In that experiment the first Stokes rollover was avoided by pumping the KGW with an external quasi-CW laser source. It was shown that the Raman laser performance was enhanced with a low duty cycle and brought to its minimum when the duration of each pump pulse was long enough to heat up the crystal and generate thermal lensing.

It has to be noted that unlike most all-solid-state Raman lasers, the intracavity

power does not exert, at least appreciably [7], thermal lensing on the SDL gain medium. Therefore, thermal lensing in the fundamental cavity can be neglected. This implies thermal lensing affects the spatial overlap of the fundamental and the Stokes modes in the Raman crystal. At the same time, since the thermal lens strength diminishes with the pump size, this changes, in turn, the thermal lens focal length itself again. Most accurate measurements of the thermal lens strength require a lateral shearing interferometry technique and it can be used in most lasers [34], including Raman lasers [138]. Here we instead indicatively quantify the strength of the thermal lens assuming that the most dominant contribution is given by the thermal variation of the refractive index due to heat deposited during the SRS process. In this case, the thermal lens strength can be calculated as follows [150]

$$\frac{1}{f(z)} = \frac{dn}{dT}\frac{P_{out}}{k_c A(z)}\left(\frac{\lambda_1}{\lambda_f} - 1\right) \tag{5.2}$$

where λ_f, λ_1 are the fundamental and Stokes wavelengths; $k_c = 3.8$ $\mathrm{Wm^{-1}K^{-1}}$ and $dn/dT = -1.16 \cdot 10^{-5}$ $\mathrm{K^{-1}}$ are the KGW thermal conductivity and the thermo-optic coefficient respectively at 1320 nm [189]; $A(z)$ is the transversal area of the Stokes multi-mode beam propagating along the crystal during multi-mode operation; P_{out} is the time-averaged power at the Stokes wavelength, which can be taken as the Stokes laser output power itself [34]. The negative value of the thermo-optic coefficient makes the lens diverging. Given the relative tight focusing and assuming that SRS is generated throughout the entire length of the crystal, the thermal lens strength is not uniform along the optical axis: stronger in the centre and weaker towards the end facets.

The impact of the thermal lens on the stability of the laser cavity and on the modes overlap is qualitatively delineated by modelling from scratch the round-trip ABCD matrices of the fundamental and Raman cavity with a thermal lens of focal length $f(z)$, implemented throughout the crystal length. It can be calculated that the contribution of the thermal lenses generated along the crystal can be conceived as a single thin lens

of focal length equal to

$$f^{-1}(z) = \frac{1}{l}\int_{-l/2}^{l/2} \frac{dn}{dT}\frac{P_{out}}{k_c A(z)}\left(\frac{\lambda_1}{\lambda_f} - 1\right), \quad \mathrm{m}^{-1} \tag{5.3}$$

and placed at the centre of the crystal. Equation 5.3 is hence plugged into the matrix of a thin lens and the round-trip ABCD matrices were calculated in a Mathcad script. Figure 5.14 shows the output power dependency of the stability range, given by $-1 < (A + D)/2 < 1$, and the focal length of the thermal lens for the tangential and sagittal directions. For this purpose, the virtual output power after the rollover was extrapolated up to the maximum pump power. Given the relation between the thermal lens focal length and output power of Eq. 5.3, the thermal focal length varies as indicated in Fig. 5.14(left). Despite the expectations, the cavity seems not to be significantly affected by the presence of such strong diverging thermal lens, which approaches approximately -15 and -26 mm at 4 W of output power (tangential and sagittal respectively) for laser beam quality factors (M^2) of 2.7×1.5 and 5×3. Here, as indicated in Fig. **??**(right), the stability curves lie well within the stability limits and, assuming same beam qualities over higher power, the cavity remains stable. Besides, according to the simulation, the propagation of the laser beams simulated inside the crystal does not appear to be appreciably distorted (see Fig. 5.15).

Note that we have optimized the cavities at high pump, which is mostly an empirical procedure to compensate thermal effects, while also taking advantage of the intracavity Raman beam clean-up [148], which perhaps contributed to a relatively good beam quality despite high power. In addition, it is important to point out that this model neglected the contribution end-face bulging effects, which possibly compensated the negative lens.

An extensive study of thermal effects in KGW was made by McKay et al. in Ref. [188]. They externally-pumped the crystal with $p[mm]p$ mode excitation with a quasi-CW source, characterising astigmatic expansion of the beam towards higher transversal modes as the average output power increased beyond 3 W, attributing to photo-elastic effects a prevailing contribution over the thermo-optical and end-face

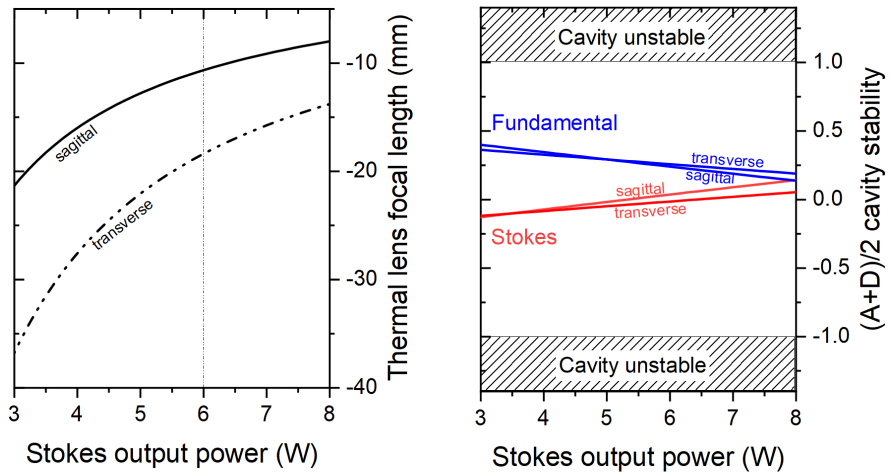

Figure 5.14: (*Left*) Focal length of the thin thermal lens along the transverse and sagittal direction calculated via Eq. 5.3. The vertical dashed line marks the maximum output power of the Raman laser. (*Right*) Stability curves of the fundamental (blue) and the Raman multi-mode laser beam (red).

bulging effects. Compensation for thermal aberration was obtained with a cylindrical lens in the Raman cavity, enabling the achievement of high output power from the Raman laser [154]. In our case, the distortion of the output beam was always avoided and we ensured that the beam was as circular as possible by optimising the cavity.

5.6.3 Tuning

Figure 5.16 shows the wavelength tuning of the fundamental and Raman lasers, with the corresponding emission spectrum at each power, when the birefringent filter and a single etalon were in the fundamental cavity. Narrow laser emission of ∼2 nm was obtained by rotating the birefringent filter and tilting the 50-μm thick etalon filter accordingly until the output power was optimised. With 70 W of diode pump power, both tuning curves showed similar trends in the full tuning range within 20% standard deviation. The fundamental wavelength tuned from 1163 to 1196 nm, limited by the free spectral range of the birefringent filter, with automatic tuning of the Raman laser wavelength between 1300 and 1341 nm. Each fundamental wavelength was automatically Stokes-shifted by (901 ± 2) cm^{-1}, and the highest output power of 4.6 W was achieved when the Raman wavelength was 1316 nm, while pumped by the fundamental field at 1177

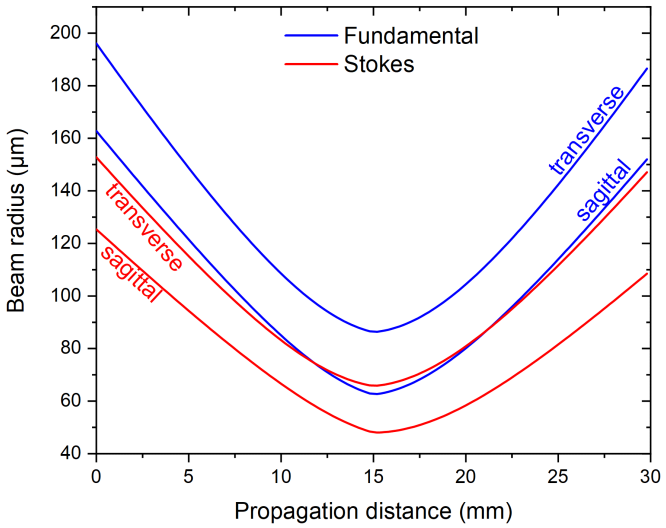

Figure 5.15: Fundamental and cavity multi-mode beam propagation in the crystal during thermal lensing where the Raman laser output power was 4 W.

nm.

Sirbu et al. demonstrated emission in the 1.3 μm spectral region with maximum output power of 7.1 W by diode-pumping an InGaAs-on-InP SDL, whose gain structure was fabricated via wafer-fusion to allow laser emission in this region [13]. Here, we have demonstrated a practical alternative way to access the 1.32 μm window with output power greater than 6 W by taking advantage of the most well-established, monolithic InGaAs-on-GaAs SDL material and an off-the-shelf KGW crystal. In the following Section, we will show that this approach can be easily configured to shift the laser output to the 1.5 μm region via a second Stokes shift in the Raman laser.

5.7 SDL-pumped KGW for 1500 nm

5.7.1 Broad emission

We achieved laser operation at 1.5 μm using the same cavity configuration as shown previously in Fig. 5.6. Most optics manufacturers did not have off-the-shelf mirrors coated for high reflection at 1300 nm and partial reflection at 1500 nm, so we opted for a broadband mirror up to 1500 nm; specifically, 0.67% OC at 1320 nm and 1% OC at the second Stokes wavelength. The 1500 nm laser output power was measured

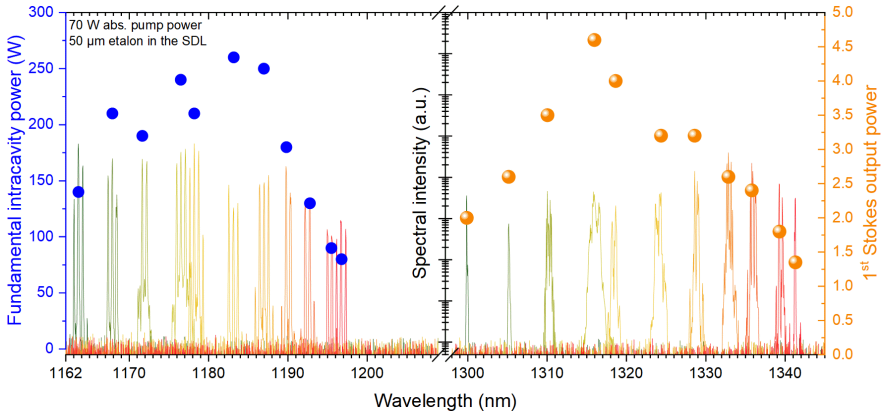

Figure 5.16: Wavelength tuning of the fundamental laser (blue circles) with related tuning of the Raman laser (orange spheres) at 70 W of absorbed diode pump power and corresponding log-scaled output spectra.

using a tuneable interference filter with a cut-off wavelength at 1400 nm for 20deg angle of incidence; while the 1320 nm laser output, collinear with the 1500 nm beam, was reflected out by a mirror, HR at 1320 nm and transparent at 1500nm. A >1250-nm long-pass filter was used to block any remaining power at the fundamental.

In Fig. 5.17 the first and second Stokes output power and the fundamental intracavity power as a function of the pump power are reported for broad emission, depicted at different pump powers in the inset. The Raman laser was optimized for high power extraction at 1.5 μm for 84 W of absorbed pump power. At this pump power, we obtained a maximum power of 1.1 W at 1.5 μm and 0.9 W of output power for the first Stokes field.

Figure 5.17 also shows that, above the first Stokes and second Stokes threshold, reached at 8 and 20 W of absorbed pump power respectively, all Stokes components and the fundamental power increased almost linearly. The fundamental power was clamped above nearly 60 W of pump power, where the first Stokes output power slightly decreased as it was converted to the second Stokes wavelength. With no control of the longitudinal modes, the fundamental and the first Stokes linewidth enlarged to a maximum of ∼5 nm (∼30 cm^{-1}) over the pump power, while the second Stokes reached a maximum of ∼2 nm width at the highest pump power. Customized coatings to enable both HR at the first Stokes wavelength and output coupling at the second

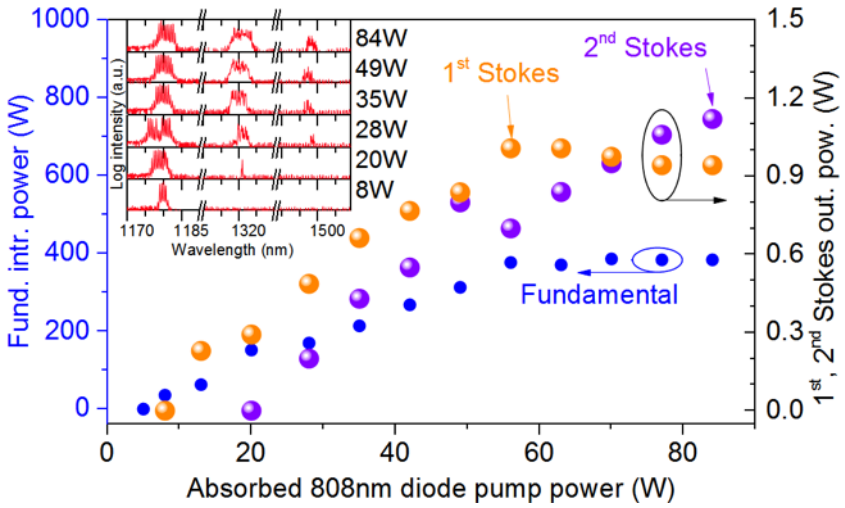

Figure 5.17: Output power of the cascaded Raman laser at the first and second Stokes radiation (orange and purple spheres, respectively), and the dependency of the fundamental intracavity power on the absorbed diode pump power (blue circles). Inset: Fundamental, first- and second-Stokes Raman spectra at different absorbed pump powers.

Stokes wavelength would enable higher output power at 1.5 μm.

5.7.2 Narrow emission and tuning

Figure 5.18 shows high spatial and spectral brightness of all wavelengths, obtained by adding two etalon filters, 50- and 500-μm-thick, in the fundamental cavity. During the single-peak regime (FWHM<50 pm, resolution limited by the spectrometer), the 1.5 μm Raman laser operated with high spatial quality of M^2~1.1 at the maximum output power of 800 mW, during simultaneous oscillation of the first Stokes propagating with M^2~1.2 and ~550 mW output power, and the fundamental with a beam quality factor of ~1.3. The combination of the etalons lowered the diode-to-2^{nd}-Stokes conversion efficiency increasing the fundamental cavity loss, which was partially compensated by a spectrally-narrow oscillation.

Figure 5.19 shows laser tuning via rotation of the intracavity birefringent plate at the highest pump power. As previously done for the first Stokes laser experiment, we maintained multi-peak narrow linewidth of ~1 nm by placing the 50-μm etalon filter inside the fundamental cavity. The fundamental field tuned non-continuously from

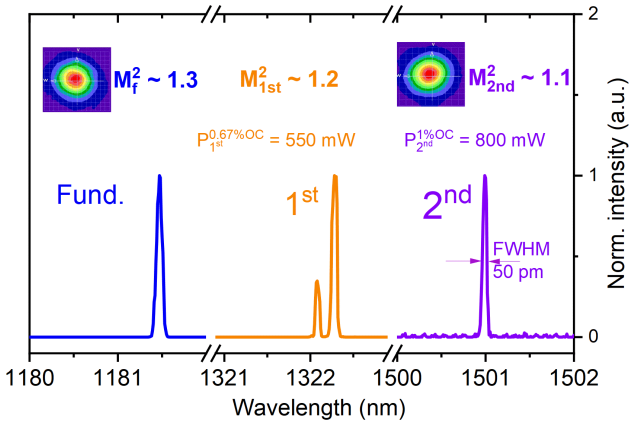

Figure 5.18: Spectrum of the cascaded Raman laser at 84 W of absorbed diode pump power with 500- and 50-μm thick etalon plates placed within the fundamental cavity (the blue, orange and purple lines represent the fundamental, first and second Stokes, respectively). The output power for the first and second Stokes with the relative output coupler transmissivity is reported in the figure. Insets: spatial laser beam profiles acquired at the highest pump power for the fundamental and second Stokes.

1164 to 1194 nm limited by the free spectral range of the BRF, with automatic tuning of the first Stokes (1300-1338 nm) and, in cascade, the second Stokes laser tuned from 1473-1522 nm. Maximum output power of around 1.3 W at the second Stokes field oscillation was attained between 1502 and 1508 nm.

A Raman conversion spectrum at the highest output power is depicted in the inset of Fig. 5.19. It can be seen also that in this tuning experiment the Raman laser presented other parasitic Stokes wavelengths: at 1456 nm, separated by 901 cm^{-1} from 1287 nm, which was in turn a 684 cm^{-1} Stokes-shift of the fundamental. The relatively low symmetry of the crystal structure bestows the KGW with several Raman features. Most likely the 684 cm^{-1} Raman shift can be assigned to an eigenmode of the oxygen-oxygen bridge bond [180, 187, 209]. The broad reflectivity of the mirrors made the cross-cascading Raman process possible, though not always repeatable. An output coupler with coatings customized for high-reflectivity limited to only the first Stokes wavelengths would avoid emission at any other unwanted wavelength and thus would improve the laser efficiency at 1.5 μm.

Compared with the state of art, Sirbu et al. demonstrated maximum output power >4 W emitting at 1480 nm using a wafer-fused AlGaInAs SDL. However, operation at

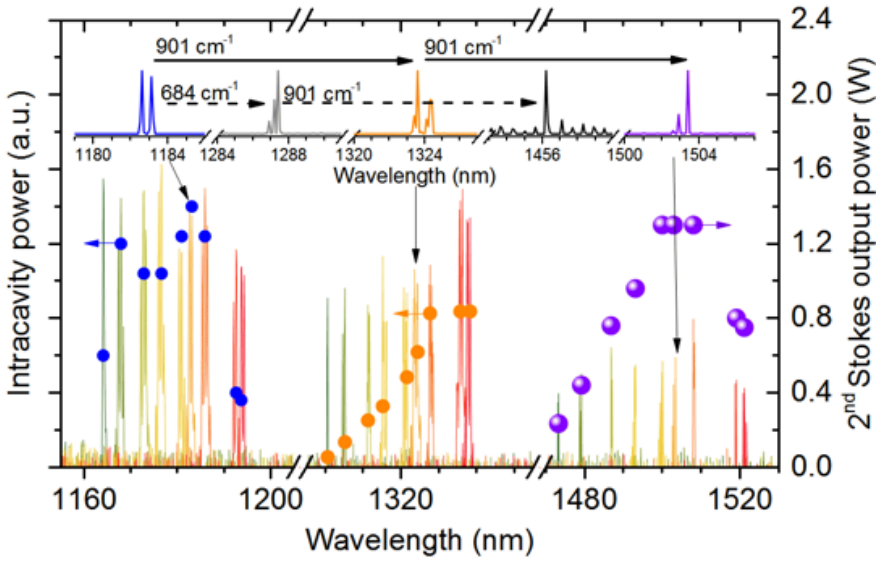

Figure 5.19: Cascaded Raman laser tuning curves with 1% output coupling at 1500 nm for an absorbed pump power of 84 W.

1550 nm required modification of the structure of the wafer-fused gain mirror, allowing maximum output power of 2.8 W [13]. Here we have demonstrated emission in the wavelength gap region of 1470-1520 nm tuning the second Stokes shift radiation of an InGaAs-based SDL-pumped KGW Raman laser.

5.8 Broad Raman laser at 1730 nm

The Raman laser at the third Stokes was achieved using an output coupler tailor-made for the diamond experiment in anticipation of a solution to AR-coat the diamond for 2$^{\text{nd}}$ Stokes up to 1740 nm. Namely, the output coupler was coated to provide $R = 99.95\%$ at 1310-1430 nm and $R = 99 \pm 0.3\%$ at 1660-1770 nm. It turned out that the coating was also suitable for the third Stokes KGW experiment. We measured the transmission to be 1% at 1740 nm, $5.5 \times 10^{-3}\%$ at 1500 nm, and $4.5 \times 10^{-3}\%$ at 1320 nm. Further, given longer wavelengths, the longest arm length of the Raman cavity (OC-DM-M3, see Table 5.1 and Fig. 5.8) was first adjusted to 379 mm in order to overlap the fundamental and the first Stokes beam propagation inside the crystal.

With no intracavity etalon, the laser would leverage the broad Raman gain linewidth

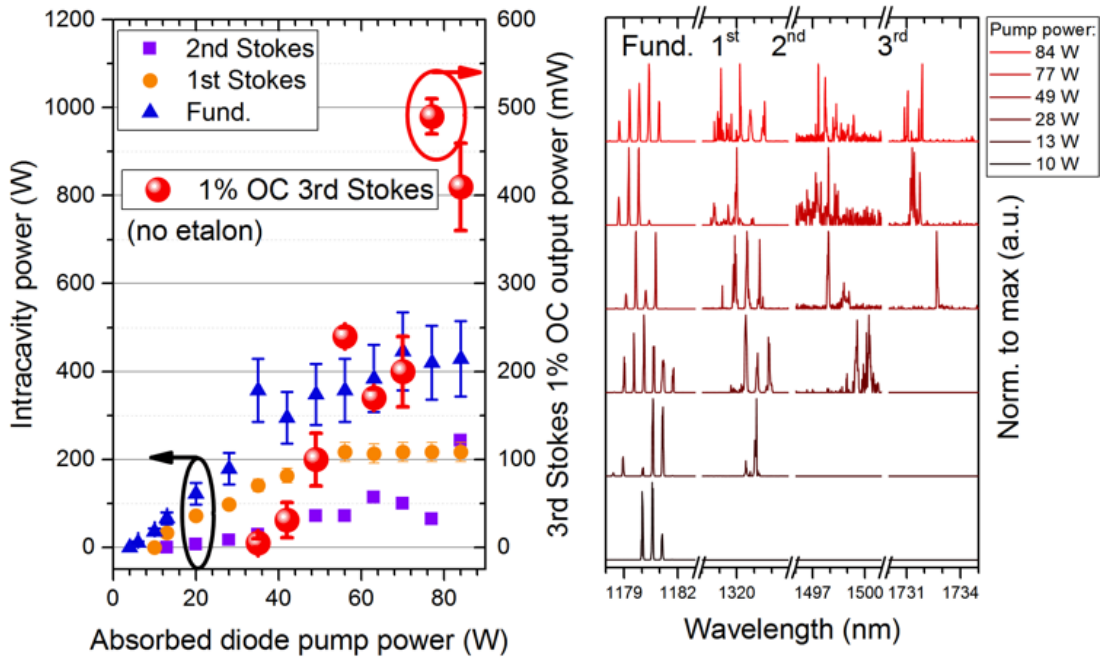

Figure 5.20: (*left*) Power transfer characteristic of the cascaded Raman laser with no etalon and (*right*) the corresponding output spectrum collected at different pump powers.

and hence the output power is expected to function, at least in theory [145], close to its maximum performance. Maximum output power of 0.5 W was reached at 77 W of absorbed pump power, well above the threshold at near 40 W, as shown in Fig. 5.20, left. The thresholds of the fundamental, 1st and 2^{nd} Stokes laser were close to each other (4, 10, 12 W respectively) due to low reflection loss at the corresponding wavelengths. The optical spectrum analyzer, with a limited resolution of 0.05 nm, collected all collinear beams at once with variable efficiency (Fig. 5.20, right).

At high output power, the fundamental emission spectrum width was ∼2 nm. All spectra appeared complex: while the fundamental shape was well defined by a certain number of etalon peaks due to the heatspreader, the Stokes spectra shapes appeared more irregular and noiser. Mutual dependency of the intracavity laser power, thermal aberration and mode radii can exist and can have consequences for the output power. This might have also reflected on the irregularity of the intracavity power. In fact, from the 2nd to the 3rd Stokes threshold, both fundamental and first Stokes increased,

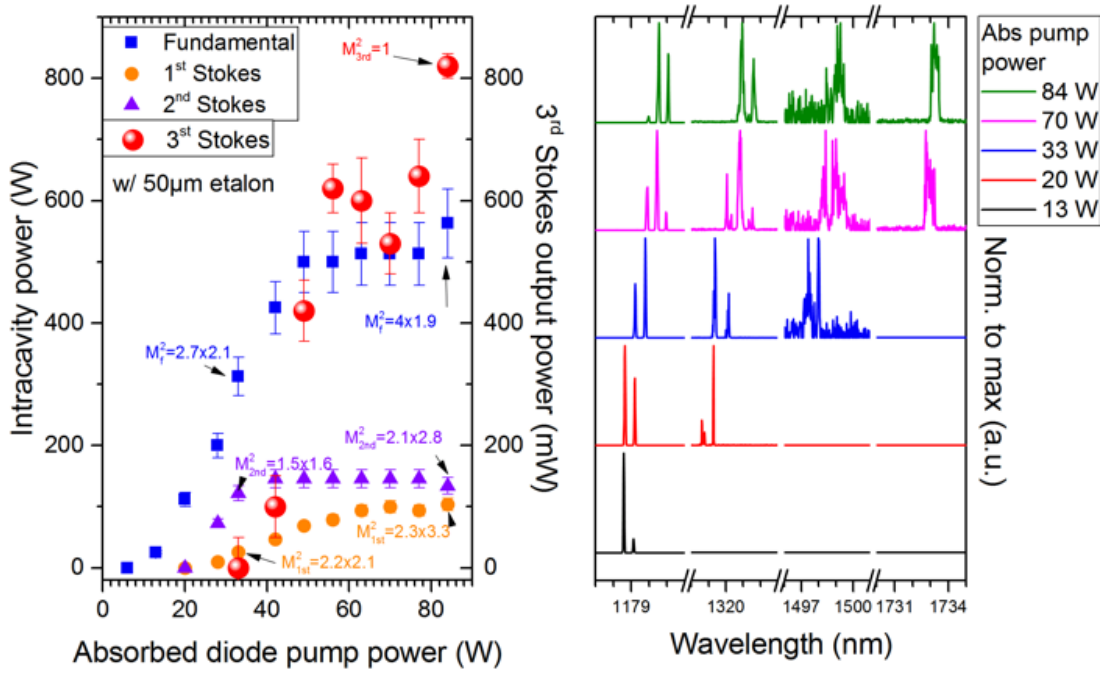

Figure 5.21: (*left*) Power transfer characteristic of the cascaded Raman laser with an intracavity 50-μm etalon and (*right*) the corresponding output spectrum collected at different pump powers.

where the fundamental is expected to be clamped by the 1st Stokes. As well as this complex behaviour, the disparity between the emission linewidth and KGW Raman gain bandwidth (5.4 cm^{-1}) also reduces pump efficiency. Adding etalons in the fundamental cavity is expected to provide optimal spectral overlap and hence better laser performance.

5.9 Spectral control

To reduce the fundamental and thus the Raman laser linewidth, a 50-μm thick etalon was added in the fundamental cavity outside the Raman resonator. Figure 5.21 shows the power transfer and the emission spectra of all cascaded wavelengths. In this configuration we were able to improve the third Stokes output power up to 820 mW. A single etalon peak resulted in a linewidth of 0.4 nm FWHM at 1733 nm.

At the same time, the third Stokes beam quality factor was measured to be close to optimum, which is expected considering that the Raman beam clean-up effect [148]

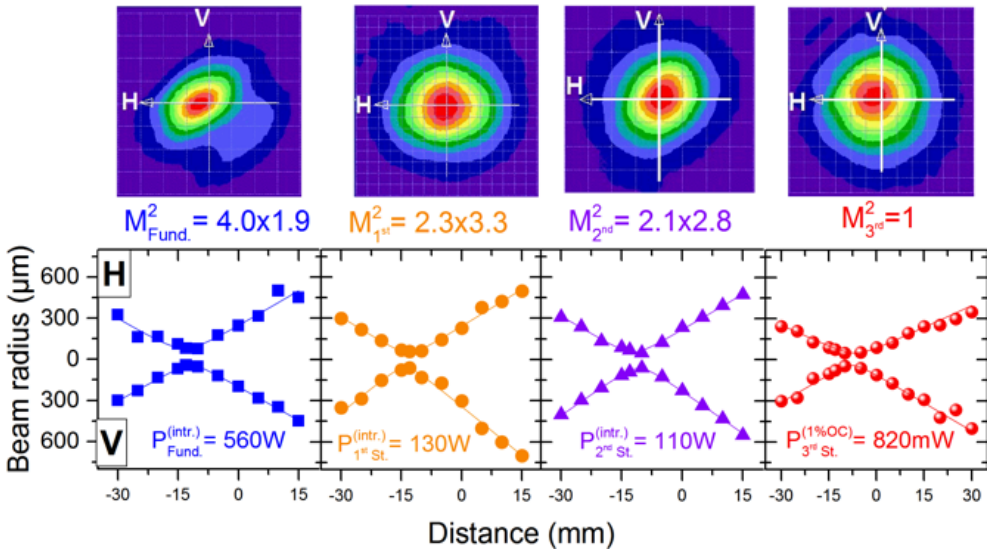

Figure 5.22: Variation of the beam radii for M^2 measurements at 820 mW output power.

relaxes the higher transverse modes of the fundamental towards TEM_{00} at each Raman conversion step. Beam quality measurements are reported in Fig. 4.22. Indeed, beam quality factors of the second, first and fundamental degrade to 2.1×2.8, 2.3×3.3 and 2.7×3.6 respectively. Near the third Stokes threshold, the beam quality improves to 1.5×1.6, 2.2×2.1 and 2.7×2.1 for the second, first and fundamental respectively.

5.9.1 Tuning with 50-μm etalon

Non-continuous tuning of the third Stokes wavelength was performed via rotation of the intracavity BRF and tilting of the 50 μm etalon filter in order to achieve the narrowest linewidth of FWHM ~1 nm. Figure 5.23 shows the tuning curve and the spectra of the cascaded Raman laser collected at maximum pump power.

The third-Stokes laser emitted from 1695.2 to ~1761 nm while tuning the fundamental in the 1163-1193.2 nm range. Simultaneously, the first and the second Stokes fields tuned over 1299.2-1336.8 nm and 1471.4-1519.8 nm, respectively. Third-Stokes laser oscillation with output power of 1.1 W occurred at 1732.2 nm when the fundamental was tuned at 1180.4 nm. Note that the longest two third-Stokes wavelengths, ~1754 and ~1761 nm, were calculated by Raman shifting the longest two second Stokes

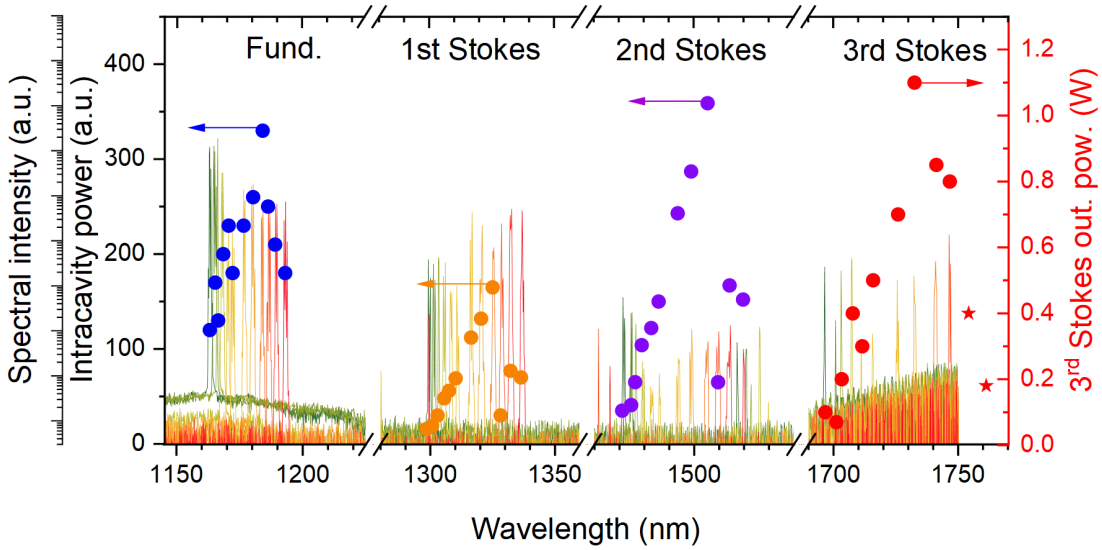

Figure 5.23: Tuning of the fundamental and the cascaded Raman laser for an absorbed diode pump power of 84 W and corresponding log-intensity emission spectra (varying from green to red for increasing fundamental wavelength) measured with 0.2 nm resolution. Normalized linear intensity spectra in the inset. Red stars data: measured power for calculated wavelength shift as signal was out of range of the optical spectrum analyzer.

wavelengths by 901 cm^{-1}, as they were out of range of our spectrometer but measured by the power meter.

5.9.2 Narrow linewidth with 50- and 500-μm etalon

Single-peak narrow emission torwards 0.05 nm FWHM (intrument-limited) was achieved using two etalon filters, 50- and 500-μm-thick, in the fundamental cavity. Also, the DM-M3 distance was lengthened to 379 mm to mode-match the third Stokes cavity mode and thus favour low Raman laser threshold (the first Stokes beam waist radius decreased from 41 to 36 μm). Figures 5.24(a) and 5.24(b) show the power transfer of all laser wavelengths with respect to the absorbed diode pump power and the corresponding evolution of the emission spectrum over the pump power range, taken with a resolution of 0.2 nm from 820-1750 nm. The third Stokes laser reached a maximum of 1.1 ± 0.1 W for an absorbed diode pump power of 84 W, well above the threshold of ~50 W, with a single peak located at 1731 nm. Figure 5.24(b) shows that the fundamental

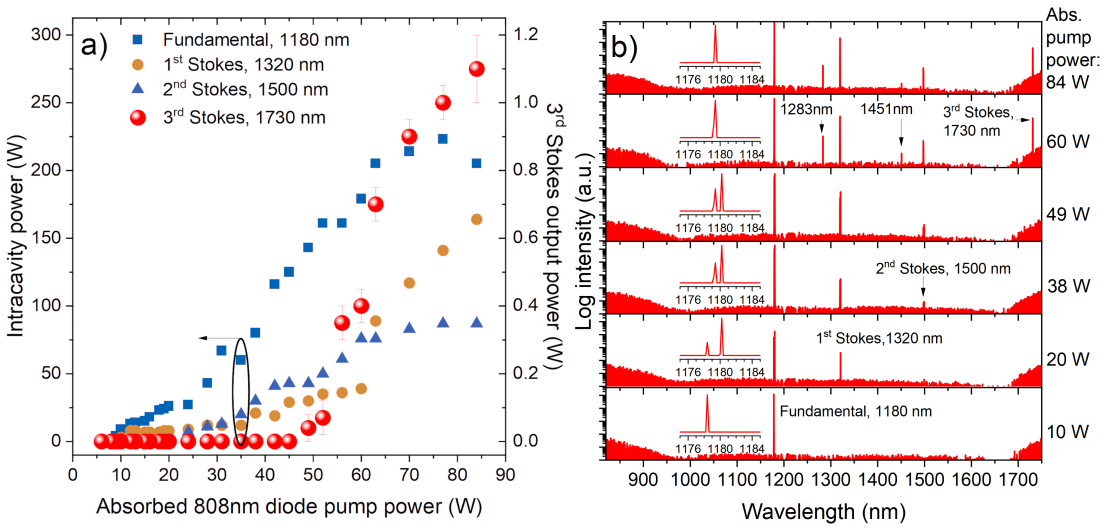

Figure 5.24: (a) Power transfer of the third Stokes Raman laser (red spheres). Intracavity power of the fundamental (blue squares), first Stokes (orange circles), and second Stokes (purple triangles). (b) Evolution of the emission spectrum of the Raman laser taken with 0.2 nm resolution.

was operating with a single peak in the pump power range of 60-84 W, and oscillating with two peaks when the diode pump power was decreased. Most likely, given the high intracavity power, the cavity was particularly susceptible to misalignment induced by thermal distortion in the etalons. Indeed, in an ideal scenario, the fundamental and each Stokes-shifted laser power are clamped to be partially converted for the generation of the next-order Stokes field throughout the pump power range until the fundamental or the Raman laser power thermally rolls off. It emerged, however, that, despite narrow linewidth of a single peak obtained at high power, this ideal trend was not entirely maintained.

There are a few factors, other than spectral broadening, that made the relationship between the fundamental and the Raman laser power quite complex, among which thermal effects in KGW and the emergence of additional Raman features as observed in the second Stokes laser experiment. The former involves the heat deposited in the crystal after the generation of any Stokes-shifted beam, which could be automatically improved by the Raman beam clean-up effect [148]. Indeed, if the heat deposits when the Stokes photons leave the cavity through the output coupler, therefore only third

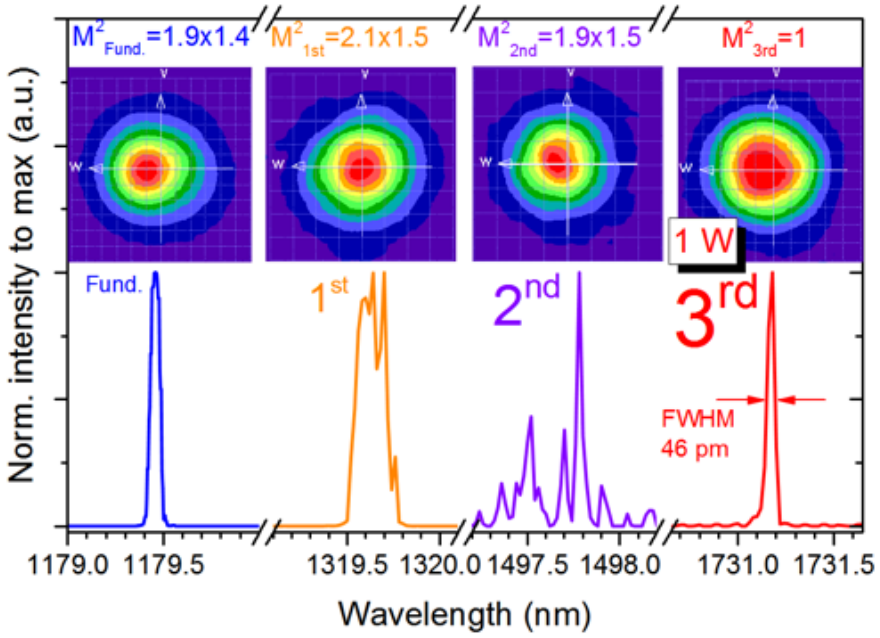

Figure 5.25: Intensity spectrum of the cascaded Raman laser collected by an optical spectrum analyzer with 50 pm resolution while the third Stokes output power was 1 W. Insets: near-field spatial profiles of the output beam section at the fundamental and Raman wavelengths.

Stokes photons thermally-load the crystal and the Raman beam clean-up at each conversion steps would be expected to compensate thermal aberration. The latter was observed more often than in the 1.5 μm Raman laser experiment case. The Raman conversion spectra in Fig. 5.24(b) exhibited, as also demonstrated in the previous experiment, a few minor and competing Raman peaks located at 1283 nm and 1451 nm for an absorbed pump power higher than 60 W. Probably, the third-Stokes output coupler made the conversion to these wavelengths more efficient. An output coupler coating specifically designed for the wavelengths of interest would be a solution that will reduce substantially the generation of undesired wavelengths.

The measurements of the beam quality factors were performed during operation with a single peak with instrument-limited FWHM of 46 pm at 1730 nm and 1 W of output power, all depicted in Fig. 5.25. While diffraction-limited propagation ($M^2 = 1$) of the third Stokes was achieved, the quality factors of fundamental, first and second Stokes-shifted laser were measured to be less than 2.1.

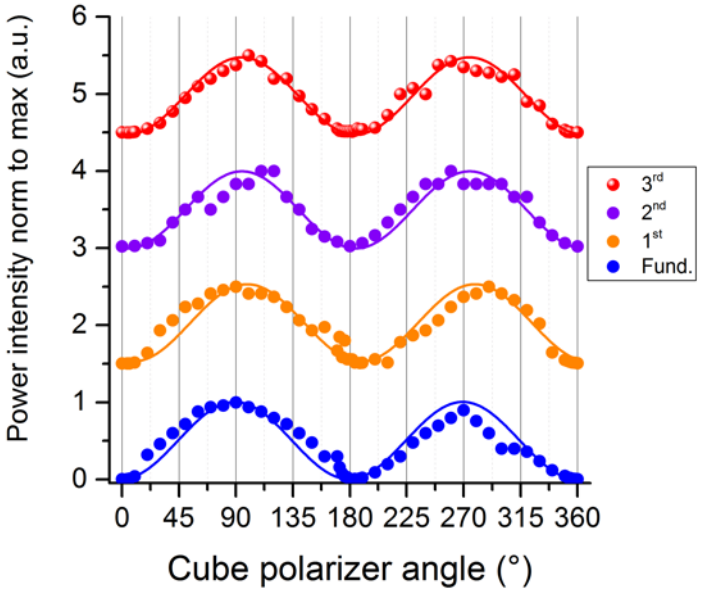

Figure 5.26: Fundamental and Raman laser polarization curves at maximum pump power.

The fundamental beam was actually slightly better than the first Stokes, in contrast to the expected degradation after intracavity Raman conversion. But note that the all beams were acquired starting, in order, from the third Stokes to the fundamental. Therefore it was probable that during acquisition of the fundamental the other Raman beams were worsening and hence we treated this deviation as a minor fluctuation. Regardless, the Raman beam clean-up process [148] has demonstrated to be very advantageous for obtaining a diffraction-limited beam, even when beam quality of the SDL is poor. Indeed, while the SDL was optimised for high intracavity power at the cost of high M^2 to maintain a good overlap with the pump size, the intracavity-pumped Raman laser, and all the more so the cascaded Raman laser, does not require pumping with a single transverse mode, as it can leverage the intracavity Raman beam clean-up effect to partially compensate thermal aberration.

5.10 Polarization

In addition to loss due to spectral broadening and optical absorption, the mutual orientation of all lasers field polarization also impacts the Raman conversion efficiency.

Figure 5.26 shows the transmitted intensity of the laser output power through the rotation of a cube polarizer (calcite).

The birefringent plate placed at Brewsters angle within the fundamental cavity before the Raman cavity input coupler (dichroic mirror) pins the fundamental field polarisation to the horizontal. The variation of the fundamental power hence is the reference of the other curves. As expected in intracavity-pumped setups, the intensities of the Stokes beams seemed to vary in accordance to the fundamental polarization curve, indicating the lasers were co-polarized. Despite some minor fluctuations, we can therefore exclude depolarization loss in KGW in this experiment.

5.11 Conclusion

The topic of this chapter was to access continuous-wave laser emission in the 1.3-1.7 μm spectral region. Via intracavity cascaded Raman shifting in a KGW crystal, we have successfully extended the upper limit of a monolithic InGaAs-based SDL beyond the $\sim$1.18 μm limit of semiconductor QW bandgap engineering. We demonstrated Raman laser maximum output power of 6.1 W with output coupling of 2.2% at the first Stokes wavelength of 1.32 μm and 80 W absorbed diode pump power, with Raman beam quality factor of $M^2 < 3$. The ideal slope efficiency of 16% was nearly reached at high power, suggesting that KGW showed good tolerance of thermal lensing. With the rotation of a 4-mm-thick single-plate birefringent filter set at Brewsters angle in the SDL cavity, we managed to achieve wavelength tuneability between 1300 and 1341 nm with output power higher than 1.5 W as limited by the free spectral range of the birefringent filter. During tuning, a narrow linewidth of $\sim$1 nm FWHM was also achieved with a 50-μm etalon in the fundamental cavity. For a broader tuning, a thinner BRF can be implemented to increase the free spectral range since the SDL can still leverage the plan-parallel heatspreader and insertion of etalon filters in the cavity for a narrow linewidth emission.

Broadband anti-reflection coatings on the KGW and highly-reflective coatings on the cavity mirrors enabled Raman laser oscillation in cascade up to the third Stokes

wavelength. A Raman laser oscillating at the second Stokes wavelength of 1.5 μm was achieved with >1W of maximum output power, concurrent with the collinear first Stokes wavelength with 0.9 W of output power, with a 1% and 0.65% output coupler, respectively. Wavelength tuning of the fundamental was obtained to tune the second Stokes laser from 1473 to 1522 nm.

Finally, we obtained a cascaded Raman laser with 1% output coupling at the third Stokes wavelength to achieve 1.1 W output power at 1732 nm and wide tuneability, from 1.70 to 1.76 μm. The KGW Raman laser owed very high spectral and spatial brightness to the intracavity etalon plates, allowing spatial propagation near TEM_{00} and a frequency spectrum as narrow as 50 pm (FWHM), despite some thermal lensing likely occurring at high Raman power, and other spectral lines emerging at 1254 and 1485 nm (probably due to the different and less efficient 684 cm^{-1} Raman shift). The Raman lasers operating at 1.32 and 1.50 μm are a valid alternative to the more compact and very competitive wafer-fused SDLs counterparts. The laser emitting at 1.7-μm via Raman conversion is an entirely novel wavelength for SDL systems. A continuous-wave Raman laser at 1.7 μm emerges in a very-low absorption window of water and therefore it can be potentially tailored for high-resolution medical imaging or remote gas sensing applications.

Chapter 6

Conclusions

This thesis has presented the development of a high-power cw laser with narrow linewidth and tuneable emission to cover the important wavelength region around the very low water absorption gap at 1.7 μm, which can be of interest for medical imaging and atmospheric sensing. Stimulated Raman scattering (SRS) has been demonstrated to be a practical means to achieve long wavelengths as an alternative to the $\chi^{(2)}$ process employed in optical parametric oscillators (OPOs) as SRS naturally avoids phase-matching requirements. As the field intensity of the pump source is the primary condition that makes possible laser emission at longer wavelength via two or more Stokes shifts, incorporating the Raman resonator within a high-finesse VECSEL made possible, for the first time, a cw output at third Stokes in the 1.7-μm region with a Raman crystal. Also, with this system we have addressed a performance gap in VECSEL spectral coverage. In terms of power, we attained more than 1 W of output power centred at 1.73 μm with emission as narrow as <46 pm as limited by the resolution of our spectrum analyzer, and diffraction-limited beam propagation ($M^2 < 1.01$) thanks to threefold beam quality improvement produced by Raman beam clean-up. Other notable achievements were attained at shorter wavelengths, located around 1.5 μm, another important water spectral window of slightly lower transmission; and 1.32 μm Raman laser output with more than 6 W and good beam quality despite the presence of thermal lensing. As much as VECSELs are now well-known for providing direct emission throughout much of the visible red to the mid-infrared region, 1.3, 1.4, 1.5 and 1.7 μm wavelengths

are nevertheless still challenging to achieve, requiring complex fabrication including wafer fusion from different substrates. Here we have thus demonstrated a platform laser technology that provides Watt-level performance in the near-infrared region using commercially available components, namely InGaAs-based VECSEL gain structures for direct emission from 0.92-1.20 μm and a tungstate-based material (KGW) for cascaded Raman conversion to extend this up to 1.7 μm, including up to 65 nm tuning. Emission centred at 1.4 μm was also achieved implementing instead a CVD diamond. This was initially intended to reach the 1.7 μm target with only two Stokes conversion steps, but it remains difficult to AR-coat diamond for such a broad range of wavelengths.

As discussed in Chapter 1, the wavelength flexibility of such VECSELs extends the operation from the visible to the mid-infrared region via engineering of the III-V semiconductor quantum well. This is possible through the monolithical growth of such layers over high-quality broadband DBRs. When these materials do not lend themselves to direct emission at long wavelength, the complexity of monolithical fabrication motivates the search for alternatives: wafer fusion and frequency-conversion. Whereas wafer-fused VECSELs have demonstrated laser emission with tens of Watt of output power in the near-infrared, their efficiency drops quite quickly at longer wavelengths. On the other hand, Raman frequency conversion of VECSELs has been used as a method to push the boundaries further; here we have taken the most mature VECSEL gain structure material InGaAs/GaAs and demonstrated 1.3-1.7 μm laser operation. As seen in Chapter 2, the simplicity of implementing a crystalline Raman-active material in a VECSEL cavity for low-threshold multi-wavelength Stokes conversion is limited more by the quality of the HR/AR coating layers of the intracavity optics, rather than by some complications that may arise around the nature of the Raman material itself (i.e. thermal effects, birefringence loss, crystal length design, and availability of samples). Being a phase-matchless process, in addition, intracavity Raman conversion leads to improvements of the output beam quality, offering more flexibility in cavity design against thermal aberration, to which most Raman materials are prone. The Raman gain spectrum is too narrow for direct broad tuning, but the VECSEL intracavity pump geometry directly transfers the broad gain bandwidth of the fundamental

automatically to the Raman laser. In these experiments wavelength tuneability was achieved by rotation of an intracavity birefringent filter in the VECSEL cavity.

6.1 Long-wavelength emission

In the first experiment reported in Chapter 3, an ultra-pure diamond was AR-coated for Raman laser emission in the eye-safe region. InGaAs-based SDLs are limited up to ∼1.2 μm, and we successfully elongated the emission wavelength to the 1.4 μm region, made possible by intracavity Raman conversion of a 1.18 μm SDL. Spectral filtering of the fundamental with etalons was essential to reach the best performance: 2.3W of maximum output power with narrow linewidth (0.1 nm FWHM). The difficulty of achieving continuous wavelength tuning from 1373 to 1415 nm suggested the detrimental presence of water vapour, as many of the absorption lines fall within this tuning range. Enclosing the laser in a dry air cavity will likely reduce the absorption and thus improve the performance. When compared to alternative SDL technology, the same region can be covered by direct emission of a wafer-fused SDL with greater efficiency. Here, we demonstrated a relatively simple way to achieve same target wavelength with a Raman-converted monolithical SDL gain chip. In principle, high efficiency may therefore be attainable using a commercial 1-μm-emitting SDL. At 1-μm pump, in fact, the diamond provides higher gain (∼17 cm/ GW) and a high-efficiency laser at ∼1.4 μm might be also achieved via cascaded Stokes conversion. Future work can be aimed at further improvements of broadband multi-layer coatings on diamond, in terms of low reflection loss (R<0.5%) and robustness. The work described in Chapter 3 was presented at Europhoton 2016 [210], and ultimately published in Optics Express [90].

In the work presented in Chapter 4, the wavelength coverage was further extended to the 1.73 μm region for the first time, via cascaded Raman conversion of the same SDL gain structure. At the time of the experiment, broadband coatings on diamond, suitable for intracavity use (1.1-1.7 μm with R<0.5% per pass), were not yet developed. Here, a commercial KGW crystal was used, thanks to the availability of high-performance AR broadband coatings on such material. In contrast to diamond, KGW

has a shorter Raman shift (901 cm^{-1} compared with 1332 cm^{-1} for diamond). Via first and second Stokes shifts, a valid alternative to wafer-fused SDLs at 1.32 and 1.50 μm was demonstrated: 6 W of maximum output power with output coupling at 1.32 μm; and output power in excess of 1 W for simultaneous output coupling at 1.32 and 1.5 μm. In addition, SDL oscillation at 1.73 μm was achieved for the first time via output coupling at the third Stokes wavelength. The third Stokes laser oscillated with narrow linewidth (<0.05 nm FWHM; instrument limited) and near diffraction limited beam quality ($M^2 \sim 1$). Whereas spectral narrowing of the fundamental did not significantly improve the performance of the first and second Stokes lasers, likely due to thermal lens fluctuations and the interplay between competing modes at both wavelengths, 1.1 W of maximum output power was achieved at 1.732-μm during tuning from 1.70 to 1.76 μm with 1% output coupling. Perhaps higher performance might be reached with higher output coupling, which was not available at the time with our resonator mirrors. Other than the Stokes shift, incidentally an anti-Stokes laser at 1.06 μm was also observed during optimisation of the 1.32-μm laser. The four-wave mixing process of the anti-Stokes laser requires manual phase matching, which is attainable by placing the crystal slightly off-axis, and is thus more complicated to optimize with the available optics and observe a reasonable output power. Nevertheless we also demonstrated for the first time that a cw anti-Stokes laser is feasible in an SDL. This work was presented at CLEO 2017 [92] and published in Optica [102].

6.2 Diamond and KGW comparison

In this project we used two materials, a synthetic diamond and a KGW crystal for wavelength conversion of the 1.18 μm InGaAs SDL material up to the eye-safe region. Table 6.1 compares the performances of the KGW and diamond Raman laser systems achieved in this work.

Diamond, and more recently CVD diamond, has been receiving significant attention in the last decade for advanced laser technology, firstly (and more widely) for thermal management [211], and now as a gain material [212] mainly thanks to its robustness,

its unmatched thermal conductivity (2000 $Wm^{-1}K^{-1}$) [137], and its large Stokes shift (1332 cm^{-1}), enabling laser operation within its large wavelength transparency range. In our experiment a synthetic diamond was exploited to address the difficult SDL wavelength region around 1.4 μm, which is also of particular interest for water vapour detection [153] due to strong absorption in this spectral region. Originally intended to be used to reach an output at 1.7 μm via cascaded Raman conversion, diamond proved to be particularly challenging when it concerned broadband coatings with our requirements (i.e. R<0.5%, 1.1-1.8μm). Indeed, most established coating companies that we approached, including Layertek, Eksma Optics and LaserOptik, were not able to guarantee, at the time of the experiment, robust coatings on diamond substrates with those characteristics. Improvements in this regard have been attained only very recently, and now companies have greater experience of ion beam sputtering on diamond substrates instead of the commonly used electron beam evaporation technique [1]. Nevertheless, broadband coatings limited to covering the fundamental to first Stokes range (1.1-1.4 μm) was sufficient for developing an alternative solution to wafer-fused VECSEL technology as well as opening a potential application for water vapour sensing. The bulk structure of the diamond is simple, enabling a single, three-fold degenerate strong phonon mode oscillation at 1332 cm^{-1}, which provides high-intensity Raman gain with a very narrow bandwidth. We attained Raman laser conversion centred at 1.4 μm and a maximum of 2.3 W output power, but the performance largely varied across the sample, most likely caused by the uncontrolled formation of impurities during the growth process, and the limited size of the surface, 2×2 mm^2, prevented us from pumping across a broader area.

KGW, on the other hand, has a low degree of symmetry, yielding a more complex Raman spectrum, resulting in a few, less intense Raman features well below the most intense 901 cm^{-1} shift, which could hinder the maximum efficiency of the laser. Further, the up-conversion-induced blue photoluminescence due to crystal impurities is also counted as loss, which was measured to be at most 0.6% per round-trip, thus being a non negligible source of loss, as it is same order of magnitude as the output coupling

[1] LaserOptik, private communication

Table 6.1: KGW and diamond Raman laser perforamance. [1]Not achieved; [2]resolution-limited.

	Stokes order	**Diamond**	**KGW**
Wavelength (nm)	1st	1400	1320
	2nd	1740(1)	1500
	3rd	-	1730
Tuning range (nm)	1st	1372-1416	1300-1342
	2nd	n/a	1470-1520
	3rd	-	1696-1761
Max. output power	1st	2.3 W	6.1 W
	2nd	n/a	1.1 W
	3rd	-	1.1 W
Linewidth (FWHM, nm)	1st	0.1 (2)	0.05 (2)
	2nd	n/a	0.05 (2)
	3rd	-	0.05 (2)
Max. diode-to-Stokes efficiency	1st	3.4%	7.3%
	2nd	n/a	1.3%
	3rd	-	1.3%
Polarization rotation	1st	24°	0°
	2nd	n/a	0°
	3rd	-	0°

transmission. Nevertheless, with this material we attained 6 W of output power at the first Stokes wavelength and effective fundamental to first Stokes efficiency of 36% (calculated with respect to the maximum available VECSEL output power, 16 W, at the same diode pump power), which compares favourably to the prior work of a 1.14 μm Raman laser reported by Savitski et al. [170], where a KGW crystal of the same length was intracavity-pumped by a Nd:YLF laser, enabling first Stokes laser output of 6.1 W with 33% effective efficiency. When compared to the diamond, however, the Raman laser at 1.4 μm was less efficient, 15% against a maximum of 28% as recorded in previous reports [89, 155, 213]. The cause of such discrepancy could be attributed most probably to the strong water vapour absorption occurring at 1.4 μm although the coating deterioration may have incurred as well. When diamond efficiency is compared to KGW performance, the limited gain bandwidth in diamond (1.5 cm^{-1} [214]) necessitated filtering of the fundamental via intracavity etalons, whereas the KGW gain is relatively broad (5.4 cm^{-1} [179]) and thus spectral narrowing returned a minor

enhancement of the output. In terms of birefringence loss, we found rotation of the Stokes field polarization in diamond, indicating the presence of residual birefringence caused by dislocation-induced stress incurred during the CVD growth process. This was not observed in KGW, where all Stokes field orders were polarized parallel to each other. Thermal lensing is another obstacle for most low thermal conductivity materials and was not negligible in the KGW when reaching 6-W output, though Raman beam clean-up compensated, and the cascaded clean-up effect up to the third Stokes improved the beam quality to TEM_{00}.

In conclusion, KGW has been demonstrated to be a valid competitor for diamond in achieving multi-Watts output power and greater versatility for multi-wavelength operation in cw SDLs.

6.3 Potential impact and future work

Tuneable lasers operating in the eye-safe region are being employed via different techniques, primarily via parametric processes in $\chi^{(2)}$-type crystals known as optical parametric oscillators (OPOs). The parametric process in $\chi^{(2)}$ materials bestows high temporal and wavelength versatility on OPOs enabling very wide coverage in the infrared in both pulsed and cw operation. This exceptional wavelength flexibility makes OPOs suitable for spectroscopy, gas sensing, frequency metrology, and comb generation. Comparing with these systems, Raman lasers are easy to build owing to less stringent material requirements: the phase-matchless characteristic of the $\chi^{(3)}$type crystal they are based on do not require active intervention for tuning as long as the pump source is tuneable. Also, similarly to OPOs, the gain-storage-free nature of Raman lasers potentially allows very low noise, narrow single-frequency Raman emission if the crystal is coupled to a low-noise, high-finesse fundamental cavity. In this regard, a very recent demonstration reports the first cw single-frequency intracavity Raman laser reaching around 30 MHz linewidth with a use of an etalon filter in the fundamental cavity [215]. Our tuneable 1.7 μm intracavity cascaded Raman laser can be hence potentially optimized for tunable single-frequency operation and ultimately developed for remote

sensing applications. As described in Chapter 1, a 1.7 μm laser is well-suited for in vivo investigations of biological tissues thanks to the low water absorption window. The reduced scattering coefficient in water at long wavelengths increases the signal penetration depth in organic tissues. Current coherence tomography technology operates in the 0.8-1.3 μm with micrometre-resolution using supercontinuum light sources. Indeed, recent demonstrations of deep-penetrating imaging at the 1.5-1.7 μm wavelength region [39] might encourage the development of such technology by taking full advantage of VECSELs.

As far as it concerns single-molecule detection, a range of remote gas sensing applications require tuneable, single-frequency light sources. As shown in Chapters 3 and 4, the insertion of etalons and birefringent elements in the VECSEL cavity promote a tuneable, narrow-linewidth laser beam. Future work can be focused on the realization of frequency-stabilized SDL-pumped Raman lasers: locking the laser to an external stable frequency reference (e.g. a high finesse Fabry-Perot interferometer), the fundamental wavelength can be stabilized to support single-frequency operation at the Raman wavelength as well. The design of a narrow-linewidth and broad tuning laser can be simplified with a multi-stage birefringent filter (Lyot filter) in the fundamental cavity coupled to a very compact Raman resonator to both ensure stability and wide longitudinal mode spacing. Tuning this laser has therefore the benefit to probing across the gas at various absorption lines and identifying the molecular species.

6.4 Summary

In summary, we have demonstrated intracavity Raman conversion for multi-Watt continuous wave output power in the 1.3-1.7 μm wavelength region, achieved through the use of an InGaAs-based SDL and two crystalline Raman materials: synthetic diamond for single Stokes conversion to the 1.4 μm region, and potassium gadolinium tungstate for Raman conversion up to third Stokes wavelength: 1.3, 1.5 and 1.7 μm. The emission of >1 W output power in the 1.7 μm water transmission window also represents the first cw third-Stokes laser in a crystalline medium and addresses the SDL emission

spectral gap between GaAs- and GaSb-based gain structures. With low absorption and scattering coefficients in water at these wavelengths, the development of such SDLs towards single-frequency operation could be engineered for single-molecule spectroscopy and medical imaging applications.

Bibliography

[1] A. Einstein, "Zur Quantentheorie der Strahlung," *Phys. Z.*, vol. 18, pp. 121–128, 1917.

[2] T. H. Maiman, "Optical and Microwave-Optical Experiments in Ruby," *Physical Review Letters*, vol. 4, pp. 564–566, 1960.

[3] A. F. Fercher, W. Drexler, C. K. Hitzenberger, and T. Lasser, "Optical coherence tomography - principles and applications," *Reports on Progress in Physics*, vol. 66, pp. 239–303, 2003.

[4] M. Kuznetsov, F. Hakimi, R. Sprague, and A. Mooradian, "High-power (>0.5W CW) diode-pumped vertical-external-cavity surface-emitting semiconductor lasers with circular TEM_{00} beams," *IEEE Photonics Technology Letters*, vol. 9, pp. 1063–1065, 1997.

[5] M. Kuznetsov, F. Hakimi, R. Sprague, and A. Mooradian, "Design and characteristics of high-power (>0.5-W CW) diode-pumped vertical-external-cavity surface-emitting semiconductor lasers with circular TEM_{00} beams," *IEEE Journal of Selected Topics in Quantum Electronics*, vol. 5, pp. 561–573, 1999.

[6] S. Calvez, J. E. Hastie, M. Guina, O. G. Okhotnikov, and M. D. Dawson, "Semiconductor disk lasers for the generation of visible and ultraviolet radiation," *Laser and Photonics Reviews*, vol. 3, pp. 407–434, 2009.

[7] M. Guina, A. Rantamäki, and A. Härkönen, "Optically pumped VECSELs: review of technology and progress," *Journal of Physics D: Applied Physics*, vol. 50, p. 383001, 2017.

[8] Coherent, "Advances in Laser Diode and OPSL Technologies Render Ion and Metal Vapor Lasers Obsolete, `https://cohrcdn.azureedge.net/assets/pdf/Advances-in-Laser-Diode-and-OPSL-Technologies.pdf`," 2018.

[9] A. R. Albrecht, T. J. Rotter, C. P. Hains, A. Stintz, G. Xin, T.-L. Wang, Y. Kaneda, J. V. Moloney, K. J. Malloy, and G. Balakrishnan, "High-power 1.25 μm InAs QD VECSEL based on resonant periodic gain structure," in *Vertical External Cavity Surface Emitting Lasers (VECSELs)* (U. Keller, ed.), vol. 7919, pp. 30 – 35, International Society for Optics and Photonics, SPIE, 2011.

[10] J.-M. Hopkins, S. A. Smith, C. W. Jeon, H. D. Sun, D. Burns, S. Calvez, M. D. Dawson, T. Jouthi, and M. Pessa, "0.6-W CW GaInNAs vertical external-cavity surface emitting laser operating at 1.32 μm," *Electronics Letters*, vol. 40, 2004.

[11] V.-M. Korpijärvi, T. Leinonen, J. Puustinen, A. Härkönen, and M. D. Guina, "11 W single gain-chip dilute nitride disk laser emitting around 1180 nm.," *Optics express*, vol. 18, pp. 25633–41, 2010.

[12] A. Karim, S. Bjorlin, J. Piprek, and J. Bowers, "Long-wavelength vertical-cavity lasers and amplifiers," *IEEE Journal of Selected Topics in Quantum Electronics*, vol. 6, pp. 1244–1253, 2000.

[13] A. Sirbu, N. Volet, A. Mereuta, J. Lyytikäinen, J. Rautiainen, O. Okhotnikov, J. Walczak, M. Wasiak, T. Czyszanowski, A. Caliman, Q. Zhu, V. Iakovlev, and E. Kapon, "Wafer-Fused Optically Pumped VECSELs Emitting in the 1310-nm and 1550-nm Wavebands," *Advances in Optical Technologies*, vol. 2011, pp. 1–8, 2011.

[14] S. Ranta, M. Tavast, T. Leinonen, N. Van Lieu, G. Fetzer, and M. Guina, "1180 nm VECSEL with output power beyond 20 W," *Electronics Letters*, vol. 49, pp. 59–60, 2013.

[15] R. N. Hall, G. E. Fenner, J. D. Kingsley, T. J. Soltys, and R. O. Carlson, "Coherent Light Emission From GaAs Junctions," *Physical Review Letters*, vol. 9, pp. 366–368, 1962.

[16] F. Koyama, S. Kinoshita, and K. Iga, "Room temperature continuous wave lasing characteristics of a GaAs vertical cavity surfaceemitting laser," *Applied Physics Letters*, vol. 55, pp. 221–222, 1989.

[17] F. Peters, M. Peters, D. Young, J. Scott, B. Thibeault, S. Corzine, and L. Coldren, "High-power vertical-cavity surface-emitting lasers," *Electronics Letters*, vol. 29, p. 200, 1993.

[18] R. Diehl, *High Power Diode Lasers*. Springer, 2000.

[19] R. Boyd, *Nonlinear Optics*. Academic Press, 2008.

[20] O. G. Okhotnikov, *Semiconductor Disk Lasers (VECSELs)*. Woodhead Publishing Limited, 2010.

[21] J. Hastie, S. Calvez, and M. Dawson, *Semiconductor disk lasers (VECSELs)*. Woodhead Publishing Limited, 2013.

[22] A. Giesen, H. Hügel, A. Voss, K. Wittig, U. Brauch, and H. Opower, "Scalable concept for diode-pumped high-power solid-state lasers," *Applied Physics B*, vol. 58, pp. 365–372, 1994.

[23] A. Giesen and J. Speiser, "Fifteen Years of Work on Thin-Disk Lasers: Results and Scaling Laws," *IEEE Journal of Selected Topics in Quantum Electronics*, vol. 13, pp. 598–609, 2007.

[24] A. Mooradian, "High brightness cavity-controlled surface emitting GaInAs lasers operating at 980 nm," in *OFC 2001. Optical Fiber Communication Conference and Exhibit. Technical Digest Postconference Edition (IEEE Cat. 01CH37171)*, vol. 4, pp. PD17–P1–3, Opt. Soc. America, 2001.

[25] J. L. A. Chilla, S. D. Butterworth, A. Zeitschel, J. P. Charles, A. L. Caprara, M. K. Reed, and L. Spinelli, "High-power optically pumped semiconductor lasers," in *Solid State Lasers XIII: Technology and Devices* (R. Scheps and H. J. Hoffman, eds.), vol. 5332, pp. 143 – 150, International Society for Optics and Photonics, SPIE, 2004.

[26] B. Rudin, A. Rutz, M. Hoffmann, D. J. H. C. Maas, A.-R. Bellancourt, E. Gini, T. Südmeyer, and U. Keller, "Highly efficient optically pumped vertical-emitting semiconductor laser with more than 20 W average output power in a fundamental transverse mode," *Optics Letters*, vol. 33, p. 2719, 2008.

[27] B. Heinen, T.-L. Wang, M. Sparenberg, A. Weber, B. Kunert, J. Hader, S. Koch, J. Moloney, M. Koch, and W. Stolz, "106 W continuous-wave output power from vertical-external-cavity surface-emitting laser," *Electronics Letters*, vol. 48, p. 516, 2012.

[28] Coherent, "Optically pumped semiconductor lasers superior reliability & performance," 2018.

[29] A. Albrecht, T. Rotter, C. Hains, A. Stintz, J. Moloney, K. Malloy, and G. Balakrishnan, "Multi-watt 1.25 μm quantum dot VECSEL," *Electronics Letters*, vol. 46, p. 856, 2010.

[30] D. I. Babić, J. J. Dudley, K. Streubel, R. P. Mirin, N. M. Margalit, J. E. Bowers, and E. E. Hu, "Transverse-mode & polarization characteristics of double-fused 1.52 μm vertical-cavity lasers," *III-Vs Review*, vol. 9, pp. 36–40, 1996.

[31] N. Margalit, J. Piprek, S. Zhang, D. Babic, K. Streubel, R. Mirin, J. Wesselmann, and J. Bowers, "64°C continuous-wave operation of 1.5-μm vertical-cavity laser," *IEEE Journal of Selected Topics in Quantum Electronics*, vol. 3, pp. 359–365, 1997.

[32] J. Rautiainen, J. Lyytikäinen, A. Sirbu, A. Mereuta, A. Caliman, E. Kapon, and O. G. Okhotnikov, "2.6 W optically-pumped semiconductor disk laser operating at 1.57-μm using wafer fusion," *Optics Express*, vol. 16, p. 21881, 2008.

[33] A. Sirbu, A. Rantamaki, E. J. Saarinen, V. Iakovlev, A. Mereuta, J. Lyytikainen, A. Caliman, N. Volet, O. G. Okhotnikov, and E. Kapon, "High performance wafer-fused semiconductor disk lasers emitting in the 1300 nm waveband," *Optics Express*, vol. 22, pp. 29398–29403, 2014.

[34] H. Pask, "The design and operation of solid-state Raman lasers," *Progress in Quantum Electronics*, vol. 27, pp. 3–56, 2003.

[35] D. C. Parrotta, W. Lubeigt, A. J. Kemp, D. Burns, M. D. Dawson, and J. E. Hastie, "Continuous-wave Raman laser pumped within a semiconductor disk laser cavity," *Optics Letters*, vol. 36, p. 1083, 2011.

[36] A. J. Lee, D. J. Spence, J. a. Piper, and H. M. Pask, "A wavelength-versatile, continuous-wave, self-Raman solid-state laser operating in the visible," *Optics express*, vol. 18, pp. 20013–20018, 2010.

[37] R. J. Williams, D. J. Spence, O. Lux, and R. P. Mildren, "High-power continuous-wave Raman frequency conversion from 1.06 μm to 1.49 μm in diamond," *Optics Express*, vol. 25, p. 749, 2017.

[38] Innoptics, "VECSEL, `http://innoptics.com/en/vecsel-16`," 2018.

[39] H. Kawagoe, M. Yamanaka, S. Makita, Y. Yasuno, and N. Nishizawa, "Full-range ultrahigh-resolution spectral-domain optical coherence tomography in 1.7 μm wavelength region for deep-penetration and high-resolution imaging of turbid tissues," *Applied Physics Express*, vol. 9, p. 127002, 2016.

[40] A. C. Tropper and S. Hoogland, "Extended cavity surface-emitting semiconductor lasers," *Progress in Quantum Electronics*, vol. 30, pp. 1–43, 2006.

[41] S. W. Corzine, R. S. Geels, J. W. Scott, R. . Yan, and L. A. Coldren, "Design of fabry-perot surface-emitting lasers with a periodic gain structure," *IEEE Journal of Quantum Electronics*, vol. 25, pp. 1513–1524, 1989.

[42] M. Y. A. Raja, S. R. J. Brueck, M. Osinski, C. F. Schaus, J. G. McInerney, T. M. Brennan, and B. E. Hammons, "Resonant periodic gain surface-emitting

semiconductor lasers," *IEEE Journal of Quantum Electronics*, vol. 25, pp. 1500–1512, 1989.

[43] A. Garnache, A. A. Kachanov, F. Stoeckel, and R. Houdré, "Diode-pumped broadband vertical-external-cavity surface-emitting semiconductor laser applied to high-sensitivity intracavity absorption spectroscopy," *Journal of the Optical Society of America B*, vol. 17, p. 1589, 2000.

[44] S.-S. Beyertt, M. Zorn, T. Kubler, H. Wenzel, M. Weyers, A. Giesen, G. Trankle, and U. Brauch, "Optical in-well pumping of a semiconductor disk laser with high optical efficiency," *IEEE Journal of Quantum Electronics*, vol. 41, pp. 1439–1449, 2005.

[45] Y. Varshni, "Temperature dependence of the energy gap in semiconductors," *Physica*, vol. 34, pp. 149–154, 1967.

[46] M. Rahim, F. Felder, M. Fill, and H. Zogg, "Optically pumped 5 μm IV-VI VECSEL with Al-heat spreader," *Optics Letters*, vol. 33, p. 3010, 2008.

[47] M. Rahim, A. Khiar, F. Felder, M. Fill, and H. Zogg, "4.5 μm wavelength vertical external cavity surface emitting laser operating above room temperature," *Applied Physics Letters*, vol. 94, p. 201112, 2009.

[48] M. Rahim, A. Khiar, F. Felder, M. Fill, H. Zogg, and M. W. Sigrist, "5-μm vertical external-cavity surface-emitting laser (VECSEL) for spectroscopic applications," *Applied Physics B*, vol. 100, pp. 261–264, 2010.

[49] T. D. Germann, A. Strittmatter, U. W. Pohl, D. Bimberg, J. Rautiainen, M. Guina, and O. G. Okhotnikov, "Quantum-dot semiconductor disk lasers," *Journal of Crystal Growth*, vol. 310, pp. 5182–5186, 2008.

[50] A. E. Willner, R. L. Byer, C. J. Chang-Hasnain, S. R. Forrest, H. Kressel, H. Kogelnik, G. J. Tearney, C. H. Townes, and M. N. Zervas, "Optics and Photonics: Key Enabling Technologies," *Proceedings of the IEEE*, vol. 100, pp. 1604–1643, 2012.

[51] J. Matthews and A. Blakeslee, "Defects in epitaxial multilayers," *Journal of Crystal Growth*, vol. 32, pp. 265–273, 1976.

[52] R. People and J. C. Bean, "Calculation of critical layer thickness versus lattice mismatch for Ge_xSi_{1x}/Si strainedlayer heterostructures," *Applied Physics Letters*, vol. 47, pp. 322–324, 1985.

[53] E. Yablonovitch and E. Kane, "Reduction of lasing threshold current density by the lowering of valence band effective mass," *Journal of Lightwave Technology*, vol. 4, pp. 504–506, 1986.

[54] A. R. Adams, "Strained-Layer Quantum-Well Lasers," *IEEE Journal of Selected Topics in Quantum Electronics*, vol. 17, pp. 1364–1373, 2011.

[55] J. H. Davies, *The Physics of Low-Dimensional Semiconductors.* Cambridge: Cambridge University Press, 1997.

[56] N. J. Ekins-Daukes, K. Kawaguchi, and J. Zhang, "Strain-Balanced Criteria for Multiple Quantum Well Structures and Its Signature in X-ray Rocking Curves ," *Crystal Growth & Design*, vol. 2, pp. 287–292, 2002.

[57] D. Babic and S. Corzine, "Analytic expressions for the reflection delay, penetration depth, and absorptance of quarter-wave dielectric mirrors," *IEEE Journal of Quantum Electronics*, vol. 28, pp. 514–524, 1992.

[58] A. J. Kemp, J.-M. Hopkins, A. J. Maclean, N. Schulz, M. Rattunde, J. Wagner, and D. Burns, "Thermal Management in 2.3-μm Semiconductor Disk Lasers: A Finite Element Analysis," *IEEE Journal of Quantum Electronics*, vol. 44, pp. 125–135, 2008.

[59] P. Holl, M. Rattunde, S. Adler, S. Kaspar, W. Bronner, A. Bachle, R. Aidam, and J. Wagner, "Recent Advances in Power Scaling of GaSb-Based Semiconductor Disk Lasers," *IEEE Journal of Selected Topics in Quantum Electronics*, vol. 21, pp. 324–335, 2015.

[60] M. Devautour, A. Michon, G. Beaudoin, I. Sagnes, L. Cerutti, and A. Garnache, "Thermal Management for High-Power Single-Frequency Tunable Diode-Pumped VECSEL Emitting in the Near- and Mid-IR," *IEEE Journal of Selected Topics in Quantum Electronics*, vol. 19, pp. 1701108–1701108, 2013.

[61] Z. Yang, A. R. Albrecht, J. G. Cederberg, and M. Sheik-Bahae, "80 nm tunable DBR-free semiconductor disk laser," *Applied Physics Letters*, vol. 109, p. 022101, 2016.

[62] M. A. Schmidt, "Wafer-to-wafer bonding for microstructure formation," *Proceedings of the IEEE*, vol. 86, pp. 1575–1585, 1998.

[63] U. Gosele, Y. Bluhm, G. Kastner, P. Kopperschmidt, G. Krauter, R. Scholz, A. Schumacher, S. Senz, Q.-Y. Tong, L.-J. Huang, Y.-L. Chao, and T. H. Lee, "Fundamental issues in wafer bonding," *Journal of Vacuum Science & Technology A: Vacuum, Surfaces, and Films*, vol. 17, p. 1145, 1999.

[64] A. Plößl and G. Kräuter, "Wafer direct bonding: Tailoring adhesion between brittle materials," *Materials Science and Engineering R: Reports*, vol. 25, pp. 1–88, 1999.

[65] E. Higurashi and T. Suga, "Review of Low-Temperature Bonding Technologies and Their Application in Optoelectronic Devices," *Electronics and Communications in Japan*, vol. 99, pp. 159–165, 2016.

[66] T. Leinonen, V. Iakovlev, A. Sirbu, E. Kapon, and M. Guina, "33 W continuous output power semiconductor disk laser emitting at 1275 nm," *Optics Express*, vol. 25, p. 7008, 2017.

[67] J. Lyytikäinen, J. Rautiainen, L. Toikkanen, A. Sirbu, A. Mereuta, A. Caliman, E. Kapon, and O. G. Okhotnikov, "1.3-μm optically-pumped semiconductor disk laser by wafer fusion," *Optics Express*, vol. 17, p. 9047, 2009.

[68] A. Rantamäki, J. Rautiainen, J. Lyytikäinen, A. Sirbu, A. Mereuta, E. Kapon, and O. G. Okhotnikov, "1 W at 785 nm from a frequency-doubled wafer-fused semiconductor disk laser," *Optics Express*, vol. 20, p. 9046, 2012.

[69] A. Kemp, G. Valentine, J.-M. Hopkins, J. Hastie, S. Smith, S. Calvez, M. Dawson, and D. Burns, "Thermal management in vertical-external-cavity surface-emitting lasers: finite-element analysis of a heatspreader approach," *IEEE Journal of Quantum Electronics*, vol. 41, pp. 148–155, 2005.

[70] J. M. Hopkins, S. Calvez, A. J. Kemp, J. E. Hastie, S. A. Smith, A. J. Maclean, D. Burns, and M. D. Dawson, "High-power vertical external-cavity surface-emitting lasers," *Physica Status Solidi C*, vol. 3, pp. 380–385, 2006.

[71] A. J. Maclean, R. B. Birch, P. W. Roth, A. J. Kemp, and D. Burns, "Limits on efficiency and power scaling in semiconductor disk lasers with diamond heat-spreaders," *Journal of the Optical Society of America B*, vol. 26, p. 2228, 2009.

[72] W. J. Alford, T. D. Raymond, and A. A. Allerman, "High power and good beam quality at 980 nm from a vertical external-cavity surface-emitting laser," *Journal of the Optical Society of America B*, vol. 19, p. 663, 2002.

[73] J. Hastie, J.-M. Hopkins, S. Calvez, Chan Wook Jeon, D. Burns, R. Abram, E. Riis, A. Ferguson, and M. Dawson, "0.5-W single transverse-mode operation of an 850-nm diode-pumped surface-emitting semiconductor laser," *IEEE Photonics Technology Letters*, vol. 15, pp. 894–896, 2003.

[74] Z. L. Liau, "Semiconductor wafer bonding via liquid capillarity," *Applied Physics Letters*, vol. 77, pp. 651–653, 2000.

[75] N. Schulz, J. M. Hopkins, M. Rattunde, D. Burns, and J. Wagner, "High-brightness long-wavelength semiconductor disk lasers," *Laser and Photonics Reviews*, vol. 2, pp. 160–181, 2008.

[76] S.-H. Park and H. Jeon, "Microchip-Type InGaN Vertical External-Cavity Surface-Emitting Laser," *Optical Review*, vol. 13, pp. 20–23, 2006.

[77] A. Ishida, Y. Sugiyama, Y. Isaji, K. Kodama, Y. Takano, H. Sakata, M. Rahim, A. Khiar, M. Fill, F. Felder, and H. Zogg, "2 W high efficiency PbS mid-infrared surface emitting laser," *Applied Physics Letters*, vol. 99, 2011.

[78] M. Rahim, A. Khiar, F. Felder, M. Fill, D. Chappuis, and H. Zogg, "Above Room Temperature Lead Salt VECSELs," *Physics Procedia*, vol. 3, pp. 1145–1148, 2010.

[79] D. C. Parrotta, A. J. Kemp, M. D. Dawson, and J. E. Hastie, "Tuneable continuous-wave diamond Raman laser," *Optics Letters*, vol. 19, p. 24165, 2011.

[80] S.-S. Beyertt, U. Brauch, F. Demaria, N. Dhidah, A. Giesen, T. Kubler, S. Lorch, F. Rinaldi, and P. Unger, "Efficient GalliumArsenide Disk Laser," *IEEE Journal of Quantum Electronics*, vol. 43, pp. 869–875, 2007.

[81] W. J. Alford, G. J. Fetzer, R. J. Epstein, Sandalphon, N. Van Lieu, S. Ranta, M. Tavast, T. Leinonen, and M. Guina, "Optically Pumped Semiconductor Lasers for Precision Spectroscopic Applications," *IEEE Journal of Quantum Electronics*, vol. 49, pp. 719–727, 2013.

[82] E. Kantola, T. Leinonen, J.-P. Penttinen, V.-M. Korpijärvi, and M. Guina, "615 nm GaInNAs VECSEL with output power above 10 W," *Optics Express*, vol. 23, p. 20280, 2015.

[83] L. Fan, C. Hessenius, M. Fallahi, J. Hader, H. Li, J. V. Moloney, W. Stolz, S. W. Koch, J. T. Murray, and R. Bedford, "Highly strained InGaAsGaAs multiwatt vertical-external-cavity surface-emitting laser emitting around 1170 nm," *Applied Physics Letters*, vol. 91, pp. 2005–2008, 2007.

[84] J. Konttinen, A. Härkönen, P. Tuomisto, M. Guina, J. Rautiainen, M. Pessa, and O. Okhotnikov, "High-power (>1 W) dilute nitride semiconductor disk laser emitting at 1240 nm," *New Journal of Physics*, vol. 9, pp. 140–140, 2007.

[85] M. Guina, V.-M. Korpijärvi, J. Rautiainen, P. Tuomisto, J. Puustinen, A. Härkönen, and O. Okhotnikov, "3.5 W GaInNAs disk laser operating at 1220

nm," in *Semiconductor Lasers and Laser Dynamics III* (K. P. Panajotov, M. Sciamanna, A. A. Valle, and R. Michalzik, eds.), vol. 6997, pp. 176 – 183, International Society for Optics and Photonics, SPIE, 2008.

[86] V. M. Korpijarvi, E. L. Kantola, T. Leinonen, R. Isoaho, and M. Guina, "Monolithic GaInNAsSb/GaAs VECSEL Operating at 1550 nm," *IEEE Journal on Selected Topics in Quantum Electronics*, vol. 21, 2015.

[87] S. Keller, A. Sirbu, V. Iakovlev, A. Caliman, A. Mereuta, and E. Kapon, "8.5 W VECSEL output at 1270 nm with conversion efficiency of 59 %," *Optics Express*, vol. 23, p. 17437, 2015.

[88] A. Rantamäki, J. Rautiainen, A. Sirbu, A. Mereuta, E. Kapon, and O. G. Okhotnikov, "1.56 μm 1 watt single frequency semiconductor disk laser," *Optics Express*, vol. 21, p. 2355, 2013.

[89] D. C. Parrotta, A. J. Kemp, M. D. Dawson, and J. E. Hastie, "Multiwatt, Continuous-Wave, Tunable Diamond Raman Laser With Intracavity Frequency-Doubling to the Visible Region," *IEEE Journal of Selected Topics in Quantum Electronics*, vol. 19, pp. 1400108–1400108, 2013.

[90] R. Casula, J.-P. Penttinen, A. J. Kemp, M. Guina, and J. E. Hastie, "1.4 μm continuous-wave diamond Raman laser," *Optics Express*, vol. 25, p. 31377, 2017.

[91] D. C. Parrotta, R. Casula, J.-p. Penttinen, T. Leinonen, A. J. Kemp, M. Guina, and J. E. Hastie, "InGaAs-QW VECSEL emitting >1.300-nm via intracavity Raman conversion," in *SPIE LASE* (K. G. Wilcox, ed.), p. 97340O, 2016.

[92] R. Casula, J.-P. Penttinen, M. Guina, A. J. Kemp, and J. E. Hastie, "Continuous-wave, cascaded Raman laser at 1.3, 1.5, and 1.7 μm," in *2017 Conference on Lasers and Electro-Optics Europe & European Quantum Electronics Conference (CLEO/Europe-EQEC)*, pp. 1–1, IEEE, 2017.

[93] P. Targowski and M. Iwanicka, "Optical Coherence Tomography: its role in the non-invasive structural examination and conservation of cultural heritage objectsa review," *Applied Physics A*, vol. 106, pp. 265–277, 2012.

[94] H. Kawagoe, S. Ishida, M. Aramaki, Y. Sakakibara, E. Omoda, H. Kataura, and N. Nishizawa, "Development of a high power supercontinuum source in the 1.7 μm wavelength region for highly penetrative ultrahigh-resolution optical coherence tomography," *Biomedical Optics Express*, vol. 5, p. 932, 2014.

[95] I. Gordon, L. Rothman, C. Hill, R. Kochanov, Y. Tan, P. Bernath, M. Birk, V. Boudon, A. Campargue, K. Chance, B. Drouin, J.-M. Flaud, R. Gamache, J. Hodges, D. Jacquemart, V. Perevalov, A. Perrin, K. Shine, M.-A. Smith, J. Tennyson, G. Toon, H. Tran, V. Tyuterev, A. Barbe, A. Császár, V. Devi, T. Furtenbacher, J. Harrison, J.-M. Hartmann, A. Jolly, T. Johnson, T. Karman, I. Kleiner, A. Kyuberis, J. Loos, O. Lyulin, S. Massie, S. Mikhailenko, N. Moazzen-Ahmadi, H. Müller, O. Naumenko, A. Nikitin, O. Polyansky, M. Rey, M. Rotger, S. Sharpe, K. Sung, E. Starikova, S. Tashkun, J. V. Auwera, G. Wagner, J. Wilzewski, P. Wcisło, S. Yu, and E. Zak, "The HITRAN2016 molecular spectroscopic database," *Journal of Quantitative Spectroscopy and Radiative Transfer*, 2017.

[96] P. J. Schlosser, J. E. Hastie, S. Calvez, A. B. Krysa, and M. D. Dawson, "InP/AlGaInP quantum dot semiconductor disk lasers for CW TEM_{00} emission at 716 - 755 nm.," *Optics express*, vol. 17, pp. 21782–7, 2009.

[97] E. J. Saarinen, J. Lyytikäinen, S. Ranta, A. Rantamäki, A. Sirbu, V. Iakovlev, E. Kapon, and O. G. Okhotnikov, "750 nm 15 W frequency-doubled semiconductor disk laser with a 44 nm tuning range," *Optics Letters*, vol. 40, p. 4380, 2015.

[98] J. Chilla, Q.-Z. Shu, H. Zhou, E. Weiss, M. Reed, and L. Spinelli, "Recent advances in optically pumped semiconductor lasers," in *Proceedings of SPIE* (H. J. Hoffman, R. K. Shori, and N. Hodgson, eds.), p. 645109, 2007.

[99] J. D. Berger, D. W. Anthon, A. Caprara, J. L. Chilla, S. V. Govorkov, A. Y. Lepert, W. Mefferd, Q.-Z. Shu, and L. Spinelli, "20 Watt CW TEM00 intracavity doubled optically pumped semiconductor laser at 532 nm," in *Vertical External Cavity Surface Emitting Lasers (VECSELs) II* (A. C. Tropper, ed.), vol. 8242, pp. 36 – 42, International Society for Optics and Photonics, SPIE, 2012.

[100] S. Hackett, A. R. Albrecht, Z. Yang, J. G. Cederberg, M. Sheik-Bahae, J. T. McGraw, R. L. Johnson, and J. W. Richey, "Development of vertical external cavity surface emitting lasers (VECSELs) for use as monochromatic and polychromatic sodium guidestars," in *Adaptive Optics Systems V* (E. Marchetti, L. M. Close, and J.-P. Vran, eds.), vol. 9909, pp. 1691 – 1697, International Society for Optics and Photonics, SPIE, 2016.

[101] C. Möller, C. Fuchs, C. Berger, A. Ruiz Perez, M. Koch, J. Hader, J. V. Moloney, S. W. Koch, and W. Stolz, "Type-II vertical-external-cavity surface-emitting laser with Watt level output powers at 1.2 μm," *Applied Physics Letters*, vol. 108, 2016.

[102] R. Casula, J.-P. Penttinen, M. Guina, A. J. Kemp, and J. E. Hastie, "Cascaded crystalline Raman lasers for extended wavelength coverage: continuous-wave, third-Stokes operation," *Optica*, vol. 5, p. 1406, 2018.

[103] J. Lyytikainen, J. Rautiainen, A. Sirbu, V. Iakovlev, A. Laakso, S. Ranta, M. Tavast, E. Kapon, and O. G. Okhotnikov, "High-Power 1.48-μm Wafer-Fused Optically Pumped Semiconductor Disk Laser," *IEEE Photonics Technology Letters*, vol. 23, pp. 917–919, 2011.

[104] Asclepion, "QuadroStarPRO, `https://www.asclepion.com/wp-content/uploads/2018/03/Brochure_QuadroStarPRO_2018-01_EN.pdf`," 2018.

[105] B. W. Tilma, Y. Jiao, J. Kotani, B. Smalbrugge, H. P. M. M. Ambrosius, and E. A. J. M. Bente, "Integrated tunable quantum-dot laser for optical coherence tomography in the 1.7 μm wavelength region," *IEEE Journal of Quantum Electronics*, vol. 48, pp. 1–133, 2011.

[106] G. Giudice, S. Guy, S. Crigler, L. Zenteno, and B. Hallock, "Effect of pump laser noise on an erbium-doped fiber-amplified signal," *IEEE Photonics Technology Letters*, vol. 14, pp. 1403–1405, 2002.

[107] L. Fan, M. Fallahi, J. Hader, A. R. Zakharian, M. Kolesik, J. V. Moloney, T. Qiu, A. Schülzgen, N. Peyghambarian, W. Stolz, S. W. Koch, and J. T. Murray, "Over 3 W high-efficiency vertical-external-cavity surface-emitting lasers and application as efficient fiber laser pump sources," *Applied Physics Letters*, vol. 86, pp. 1–3, 2005.

[108] B. D. Zelickson, S. L. Kilmer, E. Bernstein, V. A. Chotzen, J. Dock, D. Mehregan, and C. Coles, "Pulsed dye laser therapy for sun damaged skin," *Lasers in Surgery and Medicine*, vol. 25, pp. 229–236, 1999.

[109] M. Triki, P. Cermak, D. Romanini, L. Cerutti, and A. Garnache, "Extended Continuous Tuning of A Single-frequency Diode-pumped Vertical-external-cavity Surface-emitting Laser At 2.3 μm," *IEEE Photonics Technology Letters*, vol. 20, pp. 1947–1949, 2008.

[110] A. Ouvrard, L. Cerutti, and A. Garnache, "Broad continuous tunable range with single frequency Sb-based external-cavity VCSEL emitting in MIR," *Electronics Letters*, vol. 45, p. 629, 2009.

[111] T. Gherman, D. Romanini, I. Sagnes, A. Garnache, and Z. Zhang, "Cavity-enhanced absorption spectroscopy with a mode-locked diode-pumped vertical external-cavity surface-emitting laser," *Chemical Physics Letters*, vol. 390, pp. 290–295, 2004.

[112] T. Gherman, S. Kassi, A. Campargue, and D. Romanini, "Overtone spectroscopy in the blue region by cavity-enhanced absorption spectroscopy with a mode-locked femtosecond laser: application to acetylene," *Chemical Physics Letters*, vol. 383, pp. 353–358, 2004.

[113] A. Garnache, A. Ouvrard, and D. Romanini, "Single-Frequency operation of External-Cavity VCSELs: Non-linear multimode temporal dynamics and quantum limit.," *Optics Express*, vol. 15, p. 9403, 2007.

[114] R. Aviles-Espinosa, G. Filippidis, C. Hamilton, G. Malcolm, K. J. Weingarten, T. Südmeyer, Y. Barbarin, U. Keller, S. I. Santos, D. Artigas, and P. Loza-Alvarez, "Compact ultrafast semiconductor disk laser: targeting GFP based nonlinear applications in living organisms," *Biomedical Optics Express*, vol. 2, p. 739, 2011.

[115] S. C. Burd, D. T. C. Allcock, T. Leinonen, J. P. Penttinen, D. H. Slichter, R. Srinivas, A. C. Wilson, R. Jördens, M. Guina, D. Leibfried, and D. J. Wineland, "VECSEL systems for the generation and manipulation of trapped magnesium ions," *Optica*, vol. 3, p. 1294, 2016.

[116] D. Pabœuf and J. E. Hastie, "Tunable narrow linewidth AlGaInP semiconductor disk laser for Sr atom cooling applications," *Applied Optics*, vol. 55, p. 4980, 2016.

[117] J. A. Parrish, "New Concepts in Therapeutic Photomedicine; Photochemistry, Optical Targeting and the Therapeutic Window," *Journal of Investigative Dermatology*, vol. 77, pp. 45–50, 1981.

[118] S. R. Chinn, E. A. Swanson, and J. G. Fujimoto, "Optical coherence tomography using a frequency-tunable optical source," *Optics Letters*, vol. 22, p. 340, 1997.

[119] D. P. Popescu, L.-P. Choo-Smith, C. Flueraru, Y. Mao, S. Chang, J. Disano, S. Sherif, and M. G. Sowa, "Optical coherence tomography: fundamental principles, instrumental designs and biomedical applications," *Biophysical Reviews*, vol. 3, pp. 155–169, 2011.

[120] M. Wojtkowski, "High-speed optical coherence tomography: basics and applications," *Applied Optics*, vol. 49, p. D30, 2010.

[121] T. Klein, W. Wieser, C. M. Eigenwillig, B. R. Biedermann, and R. Huber, "Megahertz OCT for ultrawide-field retinal imaging with a 1050nm Fourier domain mode-locked laser," *Optics Express*, vol. 19, p. 3044, 2011.

[122] S. Ishida and N. Nishizawa, "Quantitative comparison of contrast and imaging depth of ultrahigh-resolution optical coherence tomography images in 800-1700 nm wavelength region," *Biomedical Optics Express*, vol. 3, p. 282, 2012.

[123] L. Shi, L. A. Sordillo, A. Rodríguez-Contreras, and R. Alfano, "Transmission in near-infrared optical windows for deep brain imaging," *Journal of Biophotonics*, vol. 9, pp. 38–43, 2016.

[124] C. V. Raman and K. S. Krishnan, "A New Type of Secondary Radiation," *Nature*, vol. 121, pp. 501–502, 1928.

[125] G. Landsberg and L. Mandelstam, "Eine neue Erscheinung bei der Lichtzerstreuung in Krystallen," *Die Naturwissenschaften*, vol. 16, pp. 557–558, 1928.

[126] G. Eckhardt, R. W. Hellwarth, F. J. McClung, S. E. Schwarz, D. Weiner, and E. J. Woodbury, "Stimulated Raman Scattering From Organic Liquids," *Physical Review Letters*, vol. 9, pp. 455–457, 1962.

[127] E. J. Woodbury and W. K. Ng, "Ruby Laser Operation in the Near IR," *Proceedings of the IRE*, vol. 50, pp. 2365–2383, 1962.

[128] G. Eckhardt, D. P. Bortfeld, and M. Geller, "Stimulated emission of Stokes and anti-Stokes Raman lines from diamond, calcite, and α-sulfur single crystals," *Applied Physics Letters*, vol. 3, pp. 137–138, 1963.

[129] R. W. Minck, R. W. Terhune, and W. G. Rado, "Laser-stimulated Raman effect and resonant four-photon interactions in gases H_2, D_2, and CH_4," *Applied Physics Letters*, vol. 3, pp. 181–184, 1963.

[130] J. Stone, "cw Raman fiber amplifier," *Applied Physics Letters*, vol. 26, pp. 163–165, 1975.

[131] N. Boetti, D. Pugliese, E. Ceci-Ginistrelli, J. Lousteau, D. Janner, and D. Milanese, "Highly Doped Phosphate Glass Fibers for Compact Lasers and Amplifiers: A Review," *Applied Sciences*, vol. 7, p. 1295, 2017.

[132] A. S. Grabtchikov, V. a. Lisinetskii, V. a. Orlovich, M. Schmitt, R. Maksimenka, and W. Kiefer, "Multimode pumped continuous-wave solid-state Raman laser," *Optics Letters*, vol. 29, p. 2524, 2004.

[133] A. A. Demidovich, A. Grabtchikov, V. A. Lisinetskii, V. N. Burakevich, V. A. Orlovich, and W. Kiefer, "Continuous-wave Raman generation in a diode-pumped Nd^{3+}:$KGd(WO_4)_2$ laser.," *Optics letters*, vol. 30, pp. 1701–3, 2005.

[134] H. M. Pask, "Continuous-wave, all-solid-state, intracavity Raman laser," *Optics Letters*, vol. 30, p. 2454, 2005.

[135] A. J. Lee, J. Lin, and H. M. Pask, "Near-infrared and orange red emission from a continuous-wave , second-Stokes self-Raman Nd:$GdVO_4$ laser," *Optics Letters*, vol. 35, pp. 3000–3002, 2010.

[136] A. M. Zaitsev, *Optical properties of diamond: a data handbook*. Springer, 2001.

[137] R. P. Mildren, "Intrinsic Optical Properties of Diamond," *Optical Engineering of Diamond*, pp. 2–3, 2013.

[138] G. M. Bonner, H. M. Pask, A. J. Lee, A. J. Kemp, J. Wang, H. Zhang, and T. Omatsu, "Measurement of thermal lensing in a CW $BaWO_4$ intracavity Raman laser," *Optics Express*, vol. 20, p. 9810, 2012.

[139] A. Caprara, "Aberration insensitive resonators for OPS lasers," in *Proceedings of SPIE*, p. 719314, 2009.

[140] A. Chernikov, J. Herrmann, M. Scheller, M. Koch, B. Kunert, W. Stolz, S. Chatterjee, S. W. Koch, T. L. Wang, Y. Kaneda, J. M. Yarborough, J. Hader, and J. V. Moloney, "Influence of the spatial pump distribution on the performance of high power vertical-external-cavity surface-emitting lasers," *Applied Physics Letters*, vol. 97, p. 191110, 2010.

[141] W. Demtröder, *Laser Spectroscopy*. Berlin, Heidelberg: Springer Berlin Heidelberg, 2008.

[142] W. K. Bischel and M. J. Dyer, "Wavelength dependence of the absolute Raman gain coefficient for the Q(1) transition in H_2," *Journal of the Optical Society of America B*, vol. 3, p. 677, 1986.

[143] V. G. Savitski, S. Reilly, and A. J. Kemp, "Steady-State Raman Gain in Diamond as a Function of Pump Wavelength," *IEEE Journal of Quantum Electronics*, vol. 49, pp. 218–223, 2013.

[144] A. Penzkofer, A. Laubereau, and W. Kaiser, "High intensity Raman interactions," *Progress in Quantum Electronics*, vol. 6, pp. 55–140, 1979.

[145] D. J. Spence, "Spatial and Spectral Effects in Continuous-Wave Intracavity Raman Lasers," *IEEE Journal of Selected Topics in Quantum Electronics*, vol. 21, pp. 134–141, 2015.

[146] D. J. Spence, "Spectral effects of stimulated Raman scattering in crystals," *Progress in Quantum Electronics*, vol. 51, pp. 1–45, 2017.

[147] J. Eggleston and R. Byer, "Steady-state stimulated Raman scattering by a multimode laser," *IEEE Journal of Quantum Electronics*, vol. 16, pp. 850–853, 1980.

[148] J. T. Murray, W. L. Austin, and R. C. Powell, "Intracavity Raman conversion and Raman beam cleanup," *Optical Materials*, vol. 11, pp. 353–371, 1999.

[149] J. T. Murray, R. C. Powell, and N. Peyghambarian, "Properties of stimulated Raman scattering in crystals," *Journal of Luminescence*, vol. 66-67, pp. 89–93, 1995.

[150] H. Pask and J. Piper, "Raman lasers," in *Handbook of Solid-State Lasers*, ch. 17, pp. 493–524, Elsevier, 2013.

[151] R. P. Mildren, H. Ogilvy, and J. a. Piper, "Solid-state Raman laser generating discretely tunable ultraviolet between 266 and 320 nm," *Optics Letters*, vol. 32, p. 814, 2007.

[152] O. Kitzler, A. McKay, D. J. Spence, and R. P. Mildren, "Modelling and optimization of continuous-wave external cavity Raman lasers," *Optics Express*, vol. 23, pp. 8590–8602, 2015.

[153] O. Lux, S. Sarang, R. J. Williams, A. McKay, and R. P. Mildren, "Single longitudinal mode diamond Raman laser in the eye-safe spectral region for water vapor detection," *Optics Express*, vol. 24, pp. 876–881, 2016.

[154] A. McKay, O. Kitzler, and R. P. Mildren, "Thermal lens evolution and compensation in a high power KGW Raman laser," *Optics Express*, vol. 22, p. 6707, 2014.

[155] V. G. Savitski, J. E. Hastie, M. D. Dawson, D. Burns, and A. J. Kemp, "Multiwatt continuous-wave diamond raman laser at 1217 nm," in *CLEO/Europe and EQEC 2011 Conference Digest*, p. PDA_2, Optical Society of America, 2011.

[156] D. J. Spence, P. Dekker, and H. M. Pask, "Modeling of Continuous Wave Intracavity Raman Lasers," *IEEE Journal of Selected Topics in Quantum Electronics*, vol. 13, pp. 756–763, 2007.

[157] P. A. Apanasevich, A. A. Kananovich, and G. I. Timofeeva, "Power and lasing threshold for longitudinally pumped lasers with intracavity Raman self-conversion," *Journal of Applied Spectroscopy*, vol. 77, pp. 223–231, 2010.

[158] S. R. J. Brueck and H. Kildal, "Efficient Raman Frequency Conversion in Liquid Nitrogen," 1982.

[159] R. H. Stolen, E. P. Ippen, and A. R. Tynes, "Raman Oscillation in Glass Optical Waveguide," *Applied Physics Letters*, vol. 20, pp. 62–64, 1972.

[160] E. O. Ammann and C. D. Decker, "0.9-W Raman oscillator," *Journal of Applied Physics*, vol. 48, pp. 1973–1975, 1977.

[161] I. Friel, "Optical Quality Diamond Grown by Chemical Vapor Deposition," in *Optical Engineering of Diamond*, pp. 35–69, Weinheim, Germany: Wiley-VCH Verlag GmbH & Co. KGaA, 2013.

[162] H. Jasbeer, R. J. Williams, O. Kitzler, A. McKay, S. Sarang, J. Lin, and R. P. Mildren, "Birefringence and piezo-Raman analysis of single crystal CVD diamond and effects on Raman laser performance," *Journal of the Optical Society of America B*, vol. 33, pp. 56–64, 2016.

[163] R. Robertson, J. J. Fox, and A. E. Martin, "Two Types of Diamond," *Philosophical Transactions of the Royal Society A: Mathematical, Physical and Engineering Sciences*, vol. 232, pp. 463–535, 1934.

[164] R. S. Balmer, J. R. Brandon, S. L. Clewes, H. K. Dhillon, J. M. Dodson, I. Friel, P. N. Inglis, T. D. Madgwick, M. L. Markham, T. P. Mollart, N. Perkins, G. A. Scarsbrook, D. J. Twitchen, A. J. Whitehead, J. J. Wilman, and S. M. Woollard, "Chemical vapour deposition synthetic diamond: materials, technology and applications," *Journal of Physics: Condensed Matter*, vol. 21, p. 364221, 2009.

[165] A. R. Lang, "Causes of Birefringence in Diamond," *Nature*, vol. 213, pp. 248–251, 1967.

[166] F. P. Bundy, H. T. Hall, H. M. Strong, and R. H. Wentorf, "Man-Made Diamonds," *Nature*, vol. 176, pp. 51–55, 1955.

[167] F. P. Bundy, "Direct Conversion of Graphite to Diamond in Static Pressure Apparatus," *The Journal of Chemical Physics*, vol. 38, pp. 631–643, 1963.

[168] I. Friel, S. L. Geoghegan, D. J. Twitchen, and G. A. Scarsbrook, "Development of high quality single crystal diamond for novel laser applications," in *Optics and Photonics for Counterterrorism and Crime Fighting VI and Optical Materials in Defence Systems Technology VII* (C. Lewis, D. Burgess, R. Zamboni, F. Kajzar, and E. M. Heckman, eds.), vol. 7838, pp. 340 – 347, International Society for Optics and Photonics, SPIE, 2010.

[169] R. Loudon, "The Raman effect in crystals," *Advances in Physics*, vol. 13, pp. 423–482, 1964.

[170] V. G. Savitski, I. Friel, J. E. Hastie, M. D. Dawson, D. Burns, and A. J. Kemp, "Characterization of single-crystal synthetic diamond for multi-watt continuous-wave Raman lasers," *IEEE Journal of Quantum Electronics*, vol. 48, pp. 328–337, 2012.

[171] A. A. Kaminskii, V. G. Ralchenko, and V. I. Konov, "Observation of stimulated raman scattering in CVD-diamond," *Journal of Experimental and Theoretical Physics Letters*, vol. 80, pp. 267–270, 2004.

[172] R. P. Mildren, D. W. Coutts, and D. J. Spence, "All-solid-state parametric Raman anti-Stokes laser at 508 nm," *Optics Express*, vol. 17, pp. 810–818, 2009.

[173] A. Sabella, J. a. Piper, and R. P. Mildren, "1240 nm diamond Raman laser operating near the quantum limit," *Optics Letters*, vol. 35, pp. 3874–3876, 2010.

[174] J.-P. M. Feve, K. E. Shortoff, M. J. Bohn, and J. K. Brasseur, "High average power diamond Raman laser," *Optics Express*, vol. 19, pp. 913–922, 2011.

[175] A. J. Kemp, P. Millar, W. Lubeigt, J. E. Hastie, M. D. Dawson, and D. Burns, "Diamond in Solid-State Disk Lasers: Thermal Management and CW Raman Generation," in *Advanced Solid-State Photonics*, p. WE7, OSA, 2009.

[176] O. Kitzler, A. McKay, and R. P. Mildren, "Continuous-wave wavelength conversion for high-power applications using an external cavity diamond Raman laser," *Optics Letters*, vol. 37, p. 2790, 2012.

[177] O. Lux, S. Sarang, O. Kitzler, D. J. Spence, and R. P. Mildren, "Intrinsically stable high-power single longitudinal mode laser using spatial hole burning free gain," *Optica*, vol. 3, p. 876, 2016.

[178] H. Jasbeer, R. J. Williams, O. Kitzler, A. McKay, and R. P. Mildren, "Wavelength diversification of high-power external cavity diamond Raman lasers using intracavity harmonic generation," *Optics Express*, vol. 26, p. 1930, 2018.

[179] I. V. Mochalov, "Laser and nonlinear properties of the potassium gadolinium tungstate laser crystal $KGd(WO_4)_2$:Nd^{3+}-(KGW:Nd)," *Optical Engineering*, vol. 36, p. 1660, 1997.

[180] D. Kasprowicz, T. Runka, A. Majchrowski, E. Michalski, and M. Drozdowski, "Vibrational properties of Nd^{3+}, Eu^{3+}, Er^{3+} and Ho^{3+} doped $KGd(WO_4)_2$ single crystals studied by Raman scattering method," *Physics Procedia*, vol. 2, pp. 539–550, 2009.

[181] A. A. Kaminskii, K.-i. Ueda, H. E. Eichler, J. Findeisen, S. N. Bagayev, F. A. Kuznetsov, A. A. Pavlyuk, G. Boulon, and F. Bourgeois, "Monoclinic Tungstates $KDy(WO_4)_2$ and $KLu(WO_4)_2$ - New $\chi(3)$-Active Crystals for Laser Raman Shifters," *Japanese Journal of Applied Physics*, vol. 37, pp. L923–L926, 1998.

[182] L. Macalik, J. Hanuza, and A. Kaminskii, "Polarized Raman spectra of the oriented $NaY(WO_4)_2$ and $KY(WO_4)_2$ single crystals," *Journal of Molecular Structure*, vol. 555, pp. 289–297, 2000.

[183] S. Kaczmarek, L. Macalik, H. Fuks, G. Leniec, T. Skibiński, and J. Hanuza, "EPR and optical properties of $KYb(WO_4)_2$ and $KTb_{0.2}Yb_{0.8}(WO_4)_2$ single crystals," *Open Physics*, vol. 10, pp. 492–499, 2012.

[184] T. Graf and E. J. Balmer, "Lasing properties of diode-laser-pumped Nd:KGW," *Optical Engineering*, vol. 34, p. 2349, 1995.

[185] K. Andryunas, Y. Vishchakas, V. Kabelka, I. V. Mochalov, A. A. Pavlyuk, G. T. Petrovskii, and V. Syrus, "Stimulated-Raman self-conversion of Nd^{3+} laser light in double tungstenate crystals," *JETP Letters*, vol. 42, pp. 410–412, 1985.

[186] P. Dekker, H. M. Pask, and J. a. Piper, "All-solid-state 704 mW continuous-wave yellow source based on an intracavity, frequency-doubled crystalline Raman laser.," *Optics Letters*, vol. 32, pp. 1114–1116, 2007.

[187] L. Macalik, J. Hanuza, and A. A. Kaminskii, "Polarized infrared and Raman spectra of $KGd(WO_4)_2$ and their interpretation based on normal coordinate analysis," *Journal of Raman Spectroscopy*, vol. 33, pp. 92–103, 2002.

[188] A. McKay, O. Kitzler, and R. P. Mildren, "Simultaneous brightness enhancement and wavelength conversion to the eye-safe region in a high-power diamond Raman laser," *Laser & Photonics Reviews*, vol. 8, pp. L37–L41, 2014.

[189] P. Loiko, K. Yumashev, N. Kuleshov, G. Rachkovskaya, and A. Pavlyuk, "Thermo-optic dispersion formulas for monoclinic double tungstates $KRe(WO_4)_2$ where Re=Gd, Y, Lu, Yb," *Optical Materials*, vol. 33, pp. 1688–1694, 2011.

[190] F. Cerdeira, C. J. Buchenauer, F. H. Pollak, and M. Cardona, "Stress-Induced Shifts of First-Order Raman Frequencies of Diamond- and Zinc-Blende-Type Semiconductors," *Physical Review B*, vol. 5, pp. 580–593, 1972.

[191] M. E. Innocenzi, H. T. Yura, C. L. Fincher, and R. A. Fields, "Thermal modeling of continuouswave endpumped solidstate lasers," *Applied Physics Letters*, vol. 56, pp. 1831–1833, 1990.

[192] J. Blows, T. Omatsu, J. Dawes, H. Pask, and M. Tateda, "Heat generation in Nd:YVO_4 with and without laser action," *IEEE Photonics Technology Letters*, vol. 10, pp. 1727–1729, 1998.

[193] E. Kantola, T. Leinonen, S. Ranta, M. Tavast, and M. Guina, "High-efficiency 20 W yellow VECSEL.," *Optics express*, vol. 22, pp. 6372–80, 2014.

[194] A. J. MacLean, *Power scaling and wavelength control of semiconductor disk lasers*. PhD thesis, University of Strathclyde, 2008.

[195] J. A. Caird, S. A. Payne, P. R. Staver, A. J. Ramponi, L. L. Chase, and W. F. Krupke, "Quantum Electronic Properties of the of the $Na_3Ga_2Li_3FI_2$: Cr^{3+} Laser," *IEEE Journal of Quantum Electronics*, vol. 24, pp. 1077–1099, 1988.

[196] W. W. Rigrod, "Gain Saturation and Output Power of Optical Masers," *Journal of Applied Physics*, vol. 34, pp. 2602–2609, 1963.

[197] D. Welford and M. A. Jaspan, "Single-frequency operation of a Cr:YAG laser from 1332 to 1554 nm," *Journal of the Optical Society of America B*, vol. 21, p. 2137, 2004.

[198] G. M. Bonner, J. Lin, A. J. Kemp, J. Wang, H. Zhang, D. J. Spence, and H. M. Pask, "Spectral broadening in continuous-wave intracavity Raman lasers," *Optics Express*, vol. 22, p. 7492, 2014.

[199] O. Svelto, *Principles of Lasers*. Boston, MA: Springer US, 5th ed., 2010.

[200] A. E. Siegman, "How to (maybe) measure laser beam quality," in *DPSS (Diode Pumped Solid State) Lasers: Applications and Issues*, p. MQ1, Optical Society of America, 1998.

[201] A. Rahimi-Iman, "Recent advances in VECSELs," *Journal of Optics*, vol. 18, p. 093003, 2016.

[202] M. Jelínek, O. Kitzler, H. Jelínková, J. Šulc, and M. Němec, "CVD-diamond external cavity nanosecond Raman laser operating at 1.63 μm pumped by 1.34 μm Nd:YAP laser," *Laser Physics Letters*, vol. 9, pp. 35–38, 2012.

[203] A. Grabtchikov, A. Kuzmin, V. Lisinetskii, G. Ryabtsev, V. Orlovich, and A. Demidovich, "Stimulated Raman scattering in Nd:KGW laser with diode pumping," *Journal of Alloys and Compounds*, vol. 300-301, pp. 300–302, 2000.

[204] Cerny and P, "Solid state lasers with Raman frequency conversion," *Progress in Quantum Electronics*, vol. 28, pp. 113–143, 2004.

[205] J. J. Neto, C. Artlett, A. Lee, J. Lin, D. Spence, J. Piper, N. U. Wetter, and H. Pask, "Investigation of blue emission from Raman-active crystals: Its origin and impact on laser performance," *Optical Materials Express*, vol. 4, p. 889, 2014.

[206] P. Jiang, X. Ding, B. Li, J. Liu, X. Yu, G. Zhang, B. Sun, C. Zhao, L. Wu, and J. Yao, "980-W and 054-mJ actively Q-switched Nd:YAG/Nd:YVO_4 hybrid gain intracavity Raman laser at 1176 nm," *Optics Express*, vol. 25, p. 3387, 2017.

[207] I. A. Khodasevich, A. A. Kornienko, E. B. Dunina, and A. S. Grabtchikov, "Transformation of optical properties of crystal media (KGW, YVO_4) exposed to quasi-continuous laser radiation in the range of the transmission band of the medium," *Optics and Spectroscopy*, vol. 115, pp. 325–334, 2013.

[208] R. J. Williams, O. Kitzler, Z. Bai, S. Sarang, H. Jasbeer, A. McKay, S. Antipov, A. Sabella, O. Lux, D. J. Spence, and R. P. Mildren, "High Power Diamond Raman Lasers," *IEEE Journal of Selected Topics in Quantum Electronics*, vol. 24, pp. 1–14, 2018.

[209] A. Senthil Kumaran, S. Moorthy Babu, S. Ganesamoorthy, I. Bhaumik, and A. K. Karnal, "Crystal growth and characterization of $KY(WO_4)_2$ and $KGd(WO_4)_2$ for laser applications," *Journal of Crystal Growth*, vol. 292, pp. 368–372, 2006.

[210] R. Casula, J.-P. Penttinen, M. Guina, A. J. Kemp, and J. E. Hastie, "∼1400-nm continuous-wave diamond Raman laser intracavity-pumped by an InGaAs semiconductor disk laser," in *7th EPS-QEOD Europhoton Conference: Solid State, Fibre, and Waveguide Coherent Light Sources - Vienna, Austria*, pp. 1–1, Europhoton, 2016.

[211] A. J. Kemp, J.-M. Hopkins, J. E. Hastie, S. Calvez, Y. Zhang, E. Gu, M. D. Dawson, and D. Burns, "Thermal Management of Lasers and LEDs Using Diamond," in *Optical Engineering of Diamond*, ch. Thermal Ma, pp. 353–384, Wiley-VCH Verlag GmbH & Co. KGaA, 2013.

[212] R. P. Mildren and J. R. Rabeau, *Optical Engineering of Diamond*. Wiley-VCH Verlag GmbH & Co. KGaA, 2013.

[213] D. C. Parrotta, *Raman lasers intracavity-pumped by semiconductor disk lasers by Daniele Carmine Parrotta*. PhD thesis, University of Strathclyde, 2012.

[214] K. Lee, B. J. Sussman, J. Nunn, V. Lorenz, K. Reim, D. Jaksch, I. Walmsley, P. Spizzirri, and S. Prawer, "Comparing phonon dephasing lifetimes in diamond using Transient Coherent Ultrafast Phonon Spectroscopy," *Diamond and Related Materials*, vol. 19, pp. 1289–1295, 2010.

[215] Q. Sheng, R. Li, A. J. Lee, D. J. Spence, and H. M. Pask, "A single-frequency intracavity Raman laser," *Optics Express*, vol. 27, p. 8540, 2019.

List of Publications

Riccardo Casula, Jussi-Pekka Penttinen, Mircea Guina, Alan J. Kemp, and Jennifer E. Hastie, Cascaded crystalline Raman lasers for extended wavelength coverage: continuous-wave, third-Stokes operation, Optica, vol. 5, no. 11, p. 1406, (2018).
DOI: 10.1364/OPTICA.5.001406

Riccardo Casula, Jussi-Pekka Penttinen, Alan J. Kemp, Mircea Guina, and Jennifer E. Hastie, 1.4 μm continuous-wave diamond Raman laser, Opt. Express, vol. 25, no. 25, p. 31377, Dec. (2017).
DOI: 10.1364/OE.25.031377

Riccardo Casula, Jussi-Pekka Penttinen, Mircea Guina, Alan J. Kemp, and Jennifer E. Hastie, Continuous-wave, cascaded Raman laser at 1.3, 1.5, and 1.7 μm, in 2017 Conference on Lasers and Electro-Optics Europe & European Quantum Electronics Conference (CLEO/Europe-EQEC), (2017).
DOI: 10.1109/CLEOE-EQEC.2017.8086251
Oral contribution

Riccardo Casula, Daniele C. Parrotta, Alan J. Kemp, Jussi-Pekka Penttinen, Tomi Leinonen, Mircea Guina, Jennifer Hastie, ∼1400-nm continuous-wave diamond Raman laser intracavity-pumped by an InGaAs semiconductor disk laser presented at 7th EPS-QEOD Europhoton Conference, Vienna (2016).

Oral contribution

Daniele C. Parrotta, Riccardo Casula, Jussi-Pekka Penttinen, Tomi Leinonen, Alan J. Kemp, Mircea Guina, Jennifer Hastie, InGaAs-QW VECSEL emitting >1300 nm via intracavity Raman conversion, Proceedings of SPIE, Vol 9734, (2016).
DOI: 10.1117/12.2217593